Squeezing-enhanced feedback cooling of a microresonator

Kerdoncuff, Hugo

Publication date:
2015

Document Version
Publisher's PDF, also known as Version of record

Technical University of Denmark

Doctoral Thesis

Squeezing-enhanced feedback cooling of a microresonator

Author:
Hugo Kerdoncuff

Supervisor:
Professor Ulrik L. Andersen

A thesis submitted in partial fulfillment of the requirements for the degree of Doctor of Philosophy

in the

Quantum Physics and Information Technology group
Department of Physics

October 2015

Squeezing-enhanced feedback cooling of a microresonator

Abstract Since its inception, quantum mechanics have not ceased to fascinate the scientific world, and especially the fundamental question about the famous Schrödinger's cat being alive or dead, or both, is still far from being answered. Although superposition states have been achieved with small particles, such as photons or atoms, they have not yet been observed on large and massive objects consisting of billions of atoms. With the advance of cavity optomechanics, the quantum behavior of massive mechanical oscillators is becoming accessible and a major key requirement in this direction is the ability to cool such oscillators into their quantum ground state. In the present work we investigate a cold damping scheme relying on the ultra-sensitive measurement of mechanical displacements, provided by a cavity-enhanced optomechanical interaction with quadrature squeezed states of light, to control strong dielectric gradient forces actuating the motion of a toroidal microresonator within a feedback loop. We first determine theoretically the conditions and limits to squeezing-enhanced measurement sensitivity of mechanical motion in a cavity optomechanical system, and perform experimentally a proof-of-principle on our microtoroids. Secondly we model the dielectric gradient force actuation scheme and investigate its capabilities in controlling the vibrations of a microtoroid acoustic mode.

Squeezing-forstærket feedback køling a fen mikroresonator

Dansk resumé Kvantemekanikken har siden sit indtog konstant fascineret den videnskabelige verden, og nogle af de mest grundlæggende aspekter af teorien, relateret til Schrödingers famøse kat, der er død og levende på samme tid, er endnu uafklarede. Sådanne superpositionstilstande er blevet realiseret for små partikler, såsom fotoner og atomer, men de er endnu ikke observeret for store og massive objekter indeholdende milliarder af atomer. Takket være den hastige udvikling af det optomekaniske forskningsfelt, er studier af makroskopiske mekaniske oscillatorers kvantemekaniske egenskaber imidlertid ved at være inden for rækkevidde. En central betingelse for dette er dog, at oscillatorerne kan køles til deres kvantemekaniske grundtilstand. I denne afhandling studeres en metode til køling via mekanisk dæmpning, hvor optiske målinger af den mekaniske oscillators udsving udnyttes til at dæmpe disse gennem et feedbackkredsløb. Konkret betragtes en mikrotoroidal oscillator, hvor ultra-følsomme målinger af de mekaniske svingninger realiseres ved at kombinere kvantestøjsreduceret – squeezed – laserlys med en kavitetsforstærket optomekanisk vekselvirkning. Betinget heraf, påvirkes og dæmpes oscillatorens dynamik ved at påtrykke en kraftig dielektrisk gradientkraft. Vi behandler indledningsvist de teoretiske betingelser og begrænsninger for sensitiviteten af squeezing-forstærkede målinger af mikromekaniske svingninger i kavitetsbaserede optomekaniske systemer. Teknikken demonstreres dernæst gennem et proof-of-principle eksperiment med mikrotoroidale oscillatorer. Endelig opstiller vi en model for køling via mekanisk dæmping baseret på dielektriske gradientkræfter, og metodens potentiale og begræsninger med henblik på manipulation af akustiske egensvingninger i mikrotoroidale oscillatorer undersøges i detaljer.

Acknowledgements

I would like to take this opportunity to acknowledge all the people who have contributed in some way to this thesis. First and foremost I would like to thank my supervisor, Professor Ulrik L. Andersen for his constant support and the confidence he has shown in my work, which has inevitably boosted my motivation. I have deeply appreciated the sociable working environment he has built up and maintained in the QPIT group. I am grateful to Ulrich B. Hoff who introduced me to the field of optomechanics and who contributed greatly to my understanding of the theoretical and experimental work I carried out during my thesis. I would also like to thank Hao Fu who accompanied and helped me for some time on my PhD project.

There are a lot of people among the QPIT group that remained to be acknowledged for their contribution to my professional development, but also to my personal fulfillment. I greatly enjoyed the friendly atmosphere of the QPIT group, playing board games, sharing drinks, and meeting for the almost-weekly homemade cakes. In particular I would like to thank Adriano Berni, Amine Lagahout and Clemens Schäfermeier for regularly sharing with me the most appreciated lunch breaks at the cafeteria.

Besides my coworkers I am grateful to my awesome flatmates, Diego Gardini and Davide Deiana, with who I have shared most of my time away from the office, when I was not traveling to enjoy the company of Sarah El-Achachi to whom I am grateful to have supported my absence during the completion of my thesis. Finally I would like to thank my parents for their constant support during my studies event though they kept me far away from them.

Contents

List of Figures

Abbreviations

AM	**A**mplitude **M**odulation
ENA	**E**lectrical **N**etwork **A**nalyzer
EOM	**E**lectro-**O**ptic **M**odulator
ESA	**E**lectronic **S**pectrum **A**nalyzer
FEM	**F**inite **E**lement **M**ethod
FFM	**F**undamental **F**lexural **M**ode
FFOC	**F**used **F**iber **O**ptic **C**oupler
FLC	**F**iber-**L**oop **C**avity
FSR	**F**ree **S**pectral **R**ange
FWHM	**F**ull **W**idth at **H**alf-**M**aximum
HWP	**H**alf-**W**ave **P**late
LO	**L**ocal **O**scillator
OPO	**O**ptical **P**arametric **O**scillator
PBS	**P**olarizing **B**eam **S**plitter
PDH	**P**ound-**D**rever-**H**all
PM	**P**hase **M**odulation
PSD	**P**ower **S**pectral **D**ensity
QBA	**Q**uantum **B**ack**A**ction
QLE	**Q**uantum **L**angevin **E**quations
QWP	**Q**uarter-**W**ave **P**late
RBM	**R**adial **B**reathing **M**ode
SEM	**S**canning **E**lectron **M**icroscope
SQL	**S**tandard **Q**uantum **L**imit
TE	**T**ransverse **E**lectric
TM	**T**ransverse **M**agnetic
TEM	**T**ransverse **E**lectro**M**agnetic
WGM	**W**hispering-**G**allery **M**ode

Introduction

Overview

The field of cavity optomechanics involves the study of physical systems that combine the properties of mechanical and optical resonators. This kind of hybrid systems have drawn the attention of the scientific communities due to their potential and actual use to solve a wide range of scientific and technological issues, from investigations into the fundamental laws of nature as the test bench of coherence collapse models [1, 2] and quantum gravity models [3], to applications in future technologies such as quantum computers and quantum communication networks [4].

Mechanical oscillators such as a simple mass-on-a-string pendulum are long- and well-known physical systems that have been studied and used extensively across the human history. In the first century, Chinese scientists used pendulums to sens acoustic vibrations from earthquakes, which was an early implementation of a force sensing scheme employing a mechanical oscillator. Many centuries later, famous experiments involved massive mechanical oscillators for sensing applications, among which is the experiment of Foucault for sensing the rotation of the Earth via the oscillations of a mass-on-a-string pendulum, or the experiment of Cavendish for measuring the gravitational constant from the oscillations of a torsional pendulum. A more day-to-day utilization of mechanical oscillators is in keeping pace of time. The harmonic properties of mechanical oscillators were recognized in the first half of the seventeenth century by Galileo who designed the first known pendulum clock, and were a few decades later harvested by Huygens who built the first pendulum clock. Nowadays most of our clock systems are still based on the periodic oscillations of mechanical resonators, although no longer in the form of pendulums but as the harmonic vibrations of piezoelectric crystals, such as quartz crystal resonators.

An optical cavity is a key component within the field of optics, and especially quantum optics, as it is essential for the production of coherent laser beams. More generally it is of particular interest for enhancing optical fields and consequently increase the interaction of light with other physical systems, such as small particles, nonlinear media, or, in the case of optomechanical systems, mechanical oscillators. The interaction

of light with massive objects was initially noticed by Kepler in the early seventeenth century, who observed that the tails of comets were deviated away from the sun. The radiation pressure force exerted by the light was later described by Maxwell in its theory of electromagnetic radiation, but it was not experimentally demonstrated before the beginning of the twentieth century.

The field of cavity optomechanics grew in the second half of the twentieth century when scientists started looking for the gravitational waves predicted by Einstein's theory of general relativity, by using large-scale interferometers [5]. Optical interferometric measurements enable the detection of small variations of the position of a massive object but it was soon recognized that the radiation pressure force exerted by the light affects the measurement [6, 7]. The need to understand and control the effects of radiation pressure on massive bodies lead to the development of a general theory of quantum measurements which set the basis of the field of optomechanics [8].

Whereas the radiation pressure force was first thought of as a nuisance for the optical interferometric measurement of the position of a massive body, scientists later realized that they could use it to control the motion of small objects, and they succeeded in trapping and manipulating nanometer-size particles such as atoms and ions. Trapped particles could subsequently be cooled to their ground state of motion where they revealed a purely quantum behavior [9]. From there the question remained as to weather more massive objects constituted of a large amount of atoms could be cooled to their ground state of motion and display a non classical behavior.

The quest for cooling a mechanical oscillator into its quantum ground state faces a number of challenges. The inherent weakness of radiation pressure forces is compensated by the use of an optical cavity to enhance the interaction of the light with the mechanical oscillator, but the high optical power circulating in a cavity generates thermal and nonlinear effects [10–13] that are detrimental to the stability of the optomechanical system, and renders difficult the control over the oscillator motion. As a consequence, alternative methods of actuating a mechanical oscillator have been investigated, and notably the use of dielectric gradient forces [14] which provide a strong influence over the oscillator dynamics.

Thesis structure

In this thesis we investigate the use of dielectric gradient forces within a cold damping scheme to cool the motion of a micromechanical resonator. Our approach combines squeezing-enhanced optomechanical transduction [15, 16], and strong dielectric gradient force actuation [17, 18] within a cavity optomechanical system.

In the first chapter we introduce the reader to relevant concepts within the field of classical and quantum optics. We review a classical representation of light from Maxwell's theory of electromagnetic radiation, and introduce the notions of carrier fields and sidebands which are particularly important in the context of optical communication and optical measurements. We follow with a quantum representation of light in close analogy to its classical counterpart. We explain the origin of quantum noise and provide a representation of light in a semi-classical picture where the optical field can be separated into a classical part and quantum fluctuations. We expand the notion of sidebands by considering the field operators in the Fourier space. The spectral description of field fluctuations is given by the power spectral density which is the frequency-dependent autocorrelation function. We end our introduction to the quantum representation of light by listing the most common quantum states of light. The end of the first chapter is dedicated to the theoretical description of the detection of light within a quantum optics framework, and introduces a major measurement tool, the balanced homodyne detector.

The first two sections of the second chapter treat separately of the two main components of an optomechanical system, namely the optical cavity and the mechanical oscillator. We develop each section with theoretical models illustrated by experimental results. We start with a general description of the properties of optical and mechanical resonators before focusing on the particularities of the microtoroid resonator. We also present a part of our experimental setup that is employed for the characterization of the whispering gallery modes of our microtoroid resonators. In the third section we combine the properties of optical and mechanical resonators within a general theory of optomechanical interactions. We explain the nature of the optomechanical coupling between an optical cavity mode and a mechanical oscillator, and describes the reciprocal action of each system on the other. We finally introduce the quantum Langevin equations that describe the evolution of the cavity optomechanical system.

In the third chapter we develop the theory of continuous displacement sensing by transforming and solving the quantum Langevin equations in the Fourier domain. We investigate the limits of mechanical displacement measurements with coherent and bright quadrature squeezed optical probe fields. The notions of imprecision noise and backaction noise are introduced which lead to the definition of the standard quantum limit in a cavity optomechanical system.

In the fourth and last chapter of this thesis we present the electrical feedback cooling scheme that we employed to damp the motion of a microtoroid resonator. We explain the origin of the dielectric gradient forces and their ability to actuate the motion of a mechanical resonator. We introduce our dielectric gradient force actuation setup and characterize it by analyzing experimental results. In a second part of the chapter we

present the theory of cold damping, and analyze our electrical feedback cooling scheme within this framework. We compare theoretically the in-loop and out-of-loop operation of a feedback actuation scheme. Finally we present experimental results showing the control of a mechanical mode of our microtoroid resonator.

Chapter 1

Basic concepts

The theory and experiments presented in this thesis are based on the principles of quantum optics. The aim of this chapter is to introduce the basic concepts of quantum optics along with the theoretical framework and notations necessary for a good understanding of the content of this thesis. Curious readers may find a more detailed description of the concepts introduced in this chapter, from a broad range of textbooks, e.g. [19–22].

1.1 Classical representation of light

Light is the first and foremost element of optics, and a prominent and omnipresent tool for the experimental work presented in this thesis. We start here by reviewing the classical properties of light that are relevant to this thesis.

1.1.1 Maxwell's and constitutive equations

In the classical picture developed in the nineteenth century, light is represented by the electromagnetic field, solution of Maxwell's equations [23]. In the context of this thesis we are only concerned with the propagation of light in vacuum or dielectric media which we assume non-magnetic and containing no free electric charges nor free currents. Under these conditions, Maxwell's equations read,

$$\vec{\nabla} \cdot \vec{D} = 0 \ , \qquad \vec{\nabla} \cdot \vec{B} = 0 \ , \tag{1.1}$$

$$\vec{\nabla} \times \vec{E} = -\frac{\partial \vec{B}}{\partial t} \ , \qquad \vec{\nabla} \times \vec{H} = \frac{\partial \vec{D}}{\partial t} \ , \tag{1.2}$$

where $\vec{E}$ and $\vec{H}$ denote the *electric and magnetic fields*, and $\vec{D}$ and $\vec{B}$ represent the *electric and magnetic field densities*. The constitutive equations relating the electric

and magnetic fields to their respective field densities read,

$$\vec{D} = \varepsilon_0 \vec{E} + \vec{P} \ , \qquad \vec{B} = \mu_0 \vec{H} \ , \tag{1.3}$$

where the constants ε_0 and μ_0 are the vacuum permittivity and vacuum permeability. The vector field $\vec{P}$ represents the density of electric dipole moments induced by the presence of an electric field in a dielectric material, and is referred to as the *induced electric polarization*. The electric polarization captures both the linear and nonlinear response of a medium to an applied electric field, and constitutes the starting point of most textbooks treatment of nonlinear optics[24]. For a linear, isotropic and lossless medium, the polarization can be written

$$\vec{P} = \varepsilon_0 \chi^{(1)}(t) * \vec{E}(t) \ , \tag{1.4}$$

where the scalar quantity $\chi^{(1)}(t)$ is the *linear electric susceptibility* of the medium, and the convolution accounts for the non-instantaneous response of the medium to the electric field, i.e. the dispersion of the medium. In the following we will omit dispersion for simplicity of notations in the time domain, and come back to it in the Fourier domain where the convolution transforms into a multiplication operation. Finally we can write the electric flux density, $\vec{D} = \varepsilon_0 \varepsilon_r \vec{E}$, with the *relative permittivity* of the medium, $\varepsilon_r = 1 + \chi^{(1)}$.

1.1.2 The wave equation

In classical electrodynamics, it is customary to express the electric and magnetic fields in terms of a *vector potential* $\vec{A}(\vec{r}, t)$,

$$\vec{E} = -\frac{\partial \vec{A}}{\partial t} \ , \qquad \vec{B} = \vec{\nabla} \times \vec{A} \ , \tag{1.5}$$

satisfying the *Coulomb gauge*, $\vec{\nabla} \cdot \varepsilon_r \vec{A} = 0$. From Maxwell's equations (1.1) and (1.2) and the constitutive relations (1.3) , we derive the wave equation satisfied by the vector potential

$$\nabla^2 \vec{A} - \frac{n^2}{c^2} \frac{\partial^2 \vec{A}}{\partial t^2} = 0 \ , \tag{1.6}$$

where we have defined the *speed of light in vacuum* $c = 1/\sqrt{\varepsilon_0 \mu_0}$, and the *refractive index* of the medium $n = \sqrt{\varepsilon_r}$. In the above we further assumed that the medium is homogeneous, i.e. $\vec{\nabla} \varepsilon_r = \vec{0}$, what is reasonable when considering the propagation of light in a bulk uniform material. Precautions must however be taken when considering the electromagnetic field at the boundary between two materials. Maxwell's equations provide two simple boundary conditions for the electric and magnetic fields on each side

of a surface with no charge nor current, delimiting two homogeneous media. Equation (1.1) implies the continuity of the component of the electric and magnetic field densities normal to the surface, while Equation (1.2) implies the continuity of the component of the electric and magnetic fields tangent to the surface.

A general solution of the wave equation in an infinite homogeneous medium is obtained by Fourier decomposition of the vector potential with respect to its space variables [19]. We consider the discrete three-dimensional Fourier decomposition in a large cube of volume V, which we write in terms of plane waves in the form

$$\vec{A}(\vec{r},t) = \sum_{\vec{k}} \mathcal{A}_k \vec{\alpha}_{\vec{k}}(t) e^{i\vec{k}.\vec{r}} \ , \tag{1.7}$$

where the factors $\mathcal{A}_k = (2\omega_k \varepsilon_0 \varepsilon_r(\omega_k) V/\hbar)^{-1/2}$ are normalization constants which makes the field amplitude vectors $\vec{\alpha}_{\vec{k}}(t)$ dimensionless. We have introduced the *wavevector* $\vec{k}$ whose magnitude, also known as the *wavenumber*, obeys the dispersion relation $|\vec{k}| = 2\pi/\lambda = n(\omega_k)\omega_k/c$, with λ the wavelength of the plane wave in the medium, and ω_k its angular frequency. We have reintroduced here the dispersion of the medium in the frequency dependence of the relative permittivity.

Inserting the Fourier decomposition of the vector potential (1.7) into the wave equation (1.6) yields the harmonic oscillator equation for the plane wave amplitude vectors,

$$\left(\frac{\partial^2}{\partial t^2} + \omega_k\right) \vec{\alpha}_{\vec{k}}(t) = \vec{0} \ , \tag{1.8}$$

whose general solutions are given by

$$\vec{\alpha}_{\vec{k}}(t) = \sum_{s=1,2} \left(\vec{\varpi}_{\vec{k},s} \alpha_{\vec{k},s} e^{-i\omega_k t} + \vec{\varpi}_{-\vec{k},s} \alpha^*_{-\vec{k},s} e^{i\omega_k t} \right) . \tag{1.9}$$

The vector form of the plane wave amplitude is resolved into a pair of two orthonormal polarization vectors, $\vec{\varpi}_{\vec{k},s}$ ($s = 1, 2$), satisfying, $\vec{\varpi}_{\vec{k},s} \cdot \vec{\varpi}_{\vec{k},s'} = \delta_{s,s'}$. Maxwell's equations impose two additional conditions, transversality with the wavevector $\vec{k} \cdot \vec{\varpi}_{\vec{k},s} = 0$, and right-handedness $\vec{\varpi}_{\vec{k},1} \times \vec{\varpi}_{\vec{k},2} = \vec{k}/|\vec{k}|$.

Finally, the general decomposition of the vector potential into plane waves reads

$$\vec{A}(\vec{r},t) = \sum_{\vec{k}} \sum_{s} \mathcal{A}_k \vec{\varpi}_{\vec{k},s} \left(\alpha_{\vec{k},s} e^{i(\vec{k}.\vec{r} - \omega_k t)} + \alpha^*_{\vec{k},s} e^{-i(\vec{k}.\vec{r} - \omega_k t)} \right) \ , \tag{1.10}$$

which leads to the decomposition of the electric field into plane waves via Equation (1.5),

$$\vec{E}(\vec{r},t) = i \sum_{\vec{k}} \sum_{s} \mathcal{E}_k \vec{\varpi}_{\vec{k},s} \left(\alpha_{\vec{k},s} e^{i(\vec{k}.\vec{r} - \omega_k t)} - \alpha^*_{\vec{k},s} e^{-i(\vec{k}.\vec{r} - \omega_k t)} \right) \ , \tag{1.11}$$

with the normalization factor $\mathcal{E}_k = (2\varepsilon_0\varepsilon_r V/\hbar\omega_k)^{-1/2}$. It is also straightforward to derive a similar expression for the magnetic field. However the present thesis deals with light-matter interactions involving the electric field essentially, so we will omit the magnetic field in the representation of light fields for the rest of this thesis.

1.1.3 Spatial modes

In the decomposition of the electric field (1.11), the plane waves are identified by a wavevector $\vec{k}$ and a polarization index s, and correspond to distinct *spatial modes* of the electric field referred to as transverse electromagnetic (TEM) plane waves. In general, spatial modes are shaped according to inhomogeneities and anisotropies of the medium, which are represented by the relative permittivity $\varepsilon_r(\vec{r})$. A spatial mode is described by a complex mode function

$$\vec{u}_{\vec{k},s}(\vec{r}) = \mathcal{E}_k(\vec{r})\vec{\varpi}_{\vec{k},s}(\vec{r})e^{i(\vec{k}.\vec{r})} \ . \tag{1.12}$$

Inserting the electric field (1.11) into the wave equation (1.6) reveals that the mode function obeys the Helmholtz equation,

$$(\nabla^2 + k^2)\vec{u}_{\vec{k},s} = \vec{0} \ . \tag{1.13}$$

Common examples of spatial modes obtained by solving the Helmholtz equation are the Laguerre-Gaussian modes and the Hermite-Gaussian modes [23]. The Laguerre-Gaussian modes provide a convenient description of TEM modes propagating in a medium with a radial symmetry, such as an optical fiber. On the other hand, the Hermite-Gaussian modes are better suited to represent TEM modes in a medium with no radial symmetry, but rather a distinction between its horizontal and vertical axis, such as in a rectangular waveguide.

From an experimental point of view, it is of prime importance to identify and control the spatial modes because the spreading of electromagnetic energy into high-order modes is often associated with loss. For the experiments conducted during this thesis we prepared and maintained the optical beams in their fundamental spatial modes, namely the Gaussian TEM_{00} mode in free-space and in optical fibers.

1.1.4 Modulation and sidebands

The starting point of every optics experiment conducted during this thesis, is a continuous electromagnetic wave produced by a laser. It is ideally represented by a monochromatic single mode with wavevector $\vec{k}_{cw}$ and frequency ω_{cw}. Mathematically the spectral envelope of a purely monochromatic wave is related to a Dirac delta function, i.e.

$\alpha_{\vec{k},s} \propto \delta(\omega_{cw} - \omega_k)$, what corresponds to a wave with infinite duration. This is obviously unphysical but provides a good approximation that simplifies the representation of optical laser beams.

In itself a classical monochromatic optical beam does not carry any information as it is simply a sinusoidal signal with a constant amplitude and a cyclic phase. However by interacting with its environment a monochromatic optical beam may experience a modification of its amplitude or phase, thereby acquiring information about its environment.This is the basic principle behind continuous variable optical communication where information is deliberately encoded onto an optical beam by modulating its amplitude or phase. Similarly optical measurements rely on the extraction of information from an optical beam after interaction with the system under measurement.

In general terms the modulation of a sinusoidal signal consists of a particular time dependence $m(t)$ imposed on its amplitude or phase. The modulation is generally much slower than the period of the sinusoidal signal, which is called the *carrier signal*. For simplicity we may consider a sinusoidal modulation with amplitude M and frequency Ω_{mod}, i.e. $m(t) = M\sin(\Omega_{mod}t)$. Starting with a monochromatic optical beam represented by a complex field amplitude $Ee^{-i\omega_{cw}t}$, where ω_{cw} is the carrier frequency and E the amplitude, the result of amplitude modulation (AM) is given by

$$\begin{aligned} E_{AM}(t) &= \left[E + M\sin(\Omega_{mod}t)\right] e^{-i\omega_{cw}t} \\ &= E\left[e^{-i\omega_{cw}t} - \frac{\xi}{2i}e^{-i(\omega_{cw}+\Omega_{mod})t} + \frac{\xi}{2i}e^{-i(\omega_{cw}-\Omega_{mod})t}\right] , \end{aligned} \tag{1.14}$$

where we define the modulation depth ξ as the ratio of the modulation amplitude to the carrier amplitude, i.e. $\xi = M/E$. The modulation results in the generation of two new monochromatic waves oscillating at symmetric frequencies $\omega_{cw} \pm \Omega_{mod}$ around the carrier frequency. They are referred to as the *upper and lower sidebands* of the carrier signal.

In a similar fashion, phase modulation (PM) results in a time dependence of the carrier phase which can be expressed as

$$\begin{aligned} E_{PM}(t) &= Ee^{-i(\omega_{cw}t + \xi\sin(\Omega_{mod}t))} \\ &= E\sum_{n=-\infty}^{+\infty} \mathrm{J}_n(\xi)e^{-i(\omega_{cw}+n\Omega_{mod})t} \qquad (1.15) \\ &\approx E\left[e^{-i\omega_{cw}t} + \frac{\xi}{2}e^{-i(\omega_{cw}+\Omega_{mod})t} - \frac{\xi}{2}e^{-i(\omega_{cw}-\Omega_{mod})t}\right] . \qquad (1.16) \end{aligned}$$

We have expanded the complex modulated field into Bessel functions of the first kind, J_n ($n \in \mathbb{Z}$), by using the identity $\exp(-i\xi\sin(\Omega_m t)) = \sum_{n=-\infty}^{+\infty} \mathrm{J}_n(\xi)\exp(-in\Omega_{mod}t)$

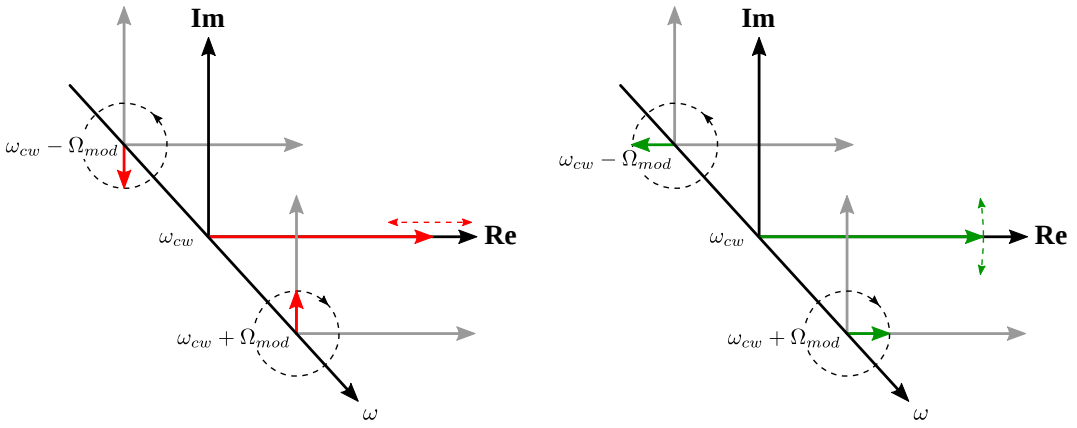

FIGURE 1.1: Spectrally resolved phase space representation of classical field amplitudes in a frame rotating at the carrier frequency ω_{cw}. The field amplitudes are represented by vectors in a complex plane, and their temporal evolution is depicted by dashed lines. The lower sideband at $\omega_{cw} - \Omega_{mod}$ is cycling at a lower frequency than the carrier wave, thus appears rotating in an anticlockwise direction, whereas the upper sidebands at $\omega_{cw} + \Omega_{mod}$ is cycling at a higher frequencies, and is shown rotating in a clockwise direction. The vector sum of the lower and upper sideband complex field amplitudes is equivalent to a harmonically oscillating carrier amplitude in case of AM (left), or carrier phase in case of PM (right).

[25], then assumed the modulation depth to be small, $\xi \ll 1$, to derive a simpler approximation of the phase modulated field in (1.16). PM, like AM, creates upper and lower sidebands equally separated from the carrier frequency by an integer number of the modulation frequency. The small-modulation approximation in (1.16) yields an expression for the modulated field amplitude very much alike AM, but with the notable difference that the upper and lower sidebands are respectively advanced and delayed by a quarter of the modulation period.

It is convenient to visualize the evolution of carrier and sidebands in a spectrally resolved phase space rotating at the carrier frequency, where each frequency component is represented by its complex field amplitude. In this representation shown in Fig. 1.1, the real and imaginary parts of the complex field amplitude are coined the *amplitude quadrature* and the *phase quadrature* of the field.

1.2 Quantum representation of light

The necessity for the development of a quantum model of the electromagnetic field beyond the classical frame of Maxwell's equations arose from the unsatisfactory explanation of physical phenomena such as blackbody radiation and the photo-electric effect. Light presents a dual wave-particle behavior that cannot be explained within the framework of classical physics, but is deeply embedded into the foundation of quantum mechanics.

1.2.1 Quantization of the electromagnetic field

The transition from a classical to a quantum description of a physical system is performed via Dirac's canonical quantization procedure [26], where the set of canonical conjugate variables, $\{q_i, p_j\} = \delta_{ij}$, representing the observable quantities of the system, are replaced by Hermitian Hilbert space operators obeying the canonical commutation relation $[\hat{q}_i, \hat{p}_j] = i\hbar\delta_{ij}$. In Equation (1.11), the field amplitudes $\alpha_{\vec{k},s}$ are complex quantities that do not represent physical observables of the system, therefore they cannot be directly associated with Hilbert space operators. A formal implementation of the canonical quantization procedure starts with the derivation of the classical energy of the electromagnetic field,

$$H = \frac{1}{2}\int \left(\vec{E}\cdot\vec{D} + \vec{B}\cdot\vec{H}\right) dV \tag{1.17}$$

$$= \frac{1}{2}\sum_{\vec{k}}\sum_{s} \hbar\omega_k \left|\alpha_{\vec{k},s}\right|^2 \tag{1.18}$$

$$= \frac{1}{2}\sum_{\vec{k}}\sum_{s} \left[p^2_{\vec{k},s} + \omega_k^2 q^2_{\vec{k},s}\right] \ , \tag{1.19}$$

where we obtained Equation (1.18) by injecting Equations (1.5) and (1.10) into (1.17). Equation (1.19) gives the energy of a system of independent harmonic oscillators, each described by a pair of real canonical variables,

$$q_{\vec{k},s}(t) = \sqrt{\frac{\hbar}{2\omega_k}}\left(\alpha_{\vec{k},s}e^{-i\omega_k t} + \alpha^*_{\vec{k},s}e^{i\omega_k t}\right) \ , \tag{1.20}$$

$$p_{\vec{k},s}(t) = -i\sqrt{\frac{\hbar\omega_k}{2}}\left(\alpha_{\vec{k},s}e^{-i\omega_k t} - \alpha^*_{\vec{k},s}e^{i\omega_k t}\right) \ . \tag{1.21}$$

We may now follow the canonical quantization procedure [19, 21] and transform the real canonical variables of the system into Hilbert space operators, $\hat{q}_{\vec{k},s}(t)$ and $\hat{p}_{\vec{k},s}(t)$ satisfying the commutation relations

$$\left[\hat{q}_{\vec{k},s}(t), \hat{p}_{\vec{k}',s'}(t)\right] = i\hbar\delta^3_{\vec{k}\vec{k}'}\delta_{ss'} \ , \quad \left[\hat{q}_{\vec{k},s}(t), \hat{q}_{\vec{k}',s'}(t)\right] = 0 \ , \quad \left[\hat{p}_{\vec{k},s}(t), \hat{p}_{\vec{k}',s'}(t)\right] = 0 \ . \tag{1.22}$$

From there the electric field may finally be expressed as a Hermitian Hilbert space operator

$$\hat{\vec{E}}(\vec{r},t) = i\sum_{\vec{k}}\sum_{s}\sqrt{\frac{\hbar\omega_k}{2\varepsilon_0\varepsilon_r(\vec{r})V}}\vec{\varpi}_{\vec{k},s}(\vec{r})\left(\hat{a}_{\vec{k},s}e^{i\vec{k}.\vec{r}} - \hat{a}^\dagger_{\vec{k},s}e^{-i\vec{k}.\vec{r}}\right) \ , \tag{1.23}$$

where we have defined the non-Hermitian *creation and annihilation operators*,

$$\hat{a}_{\vec{k},s}(t) = \frac{1}{\sqrt{2\hbar\omega_k}} \left(\omega_k \hat{q}_{\vec{k},s}(t) + i\hat{p}_{\vec{k},s}(t) \right) , \tag{1.24}$$

$$\hat{a}^\dagger_{\vec{k},s}(t) = \frac{1}{\sqrt{2\hbar\omega_k}} \left(\omega_k \hat{q}_{\vec{k},s}(t) - i\hat{p}_{\vec{k},s}(t) \right) , \tag{1.25}$$

obeying the bosonic commutation relations

$$\left[\hat{a}_{\vec{k},s}(t), \hat{a}^\dagger_{\vec{k}',s'}(t) \right] = \delta^3_{\vec{k}\vec{k}'} \delta_{ss'} , \quad \left[\hat{a}_{\vec{k},s}(t), \hat{a}_{\vec{k}',s'}(t) \right] = 0 , \quad \left[\hat{a}^\dagger_{\vec{k},s}(t), \hat{a}^\dagger_{\vec{k}',s'}(t) \right] = 0 . \tag{1.26}$$

In the rest of this thesis we will most often consider a single optical field with an unambiguously determined spatial mode, and will therefore drop the indexing to the wavevector $\vec{k}$ and the polarization index s for simplicity of notations. The field energy of a single continuous wave at frequency ω is given by Equation (1.19) using the Hilbert space operators instead of the classical observables, and can be written in terms of the creation and annihilation operators as the Hamiltonian,

$$\hat{H} = \hbar\omega \left(\hat{a}^\dagger \hat{a} + \frac{1}{2} \right) \tag{1.27}$$

where the contribution $\hbar\omega/2$ is the *zero-point energy* and reflects the fact that a quantum field always carries fluctuations, even when its mean amplitude is null. The Hermitian product of annihilation and creation operators, $\hat{n} = \hat{a}^\dagger \hat{a}$, is the number operator, counting the number of quanta of energy, the so-called *photon*, in the optical mode.

1.2.2 Field quadrature operators

The creation and annihilation operators do not represent real observables and are therefore not measurable. It is then customary to describe the optical field observables in terms of the dimensionless conjugate Hermitian operators,

$$\hat{X} = \sqrt{\frac{\omega}{\hbar}} \hat{q} = \frac{1}{\sqrt{2}} \left(\hat{a} + \hat{a}^\dagger \right) , \tag{1.28}$$

$$\hat{P} = \frac{1}{\sqrt{\hbar\omega}} \hat{p} = -\frac{i}{\sqrt{2}} \left(\hat{a} - \hat{a}^\dagger \right) , \tag{1.29}$$

referred to as the *amplitude and phase quadrature operators*. In a more general way, we introduce a pair of rotated quadrature operators,

$$\begin{pmatrix} \hat{X}^\theta \\ \hat{P}^\theta \end{pmatrix} = \frac{1}{\sqrt{2}} \begin{pmatrix} \hat{a} e^{-i\theta} + \hat{a}^\dagger e^{i\theta} \\ -i\hat{a} e^{-i\theta} + i\hat{a}^\dagger e^{i\theta} \end{pmatrix} = \mathbf{R}(-\theta) \begin{pmatrix} \hat{X} \\ \hat{P} \end{pmatrix} , \tag{1.30}$$

where we have introduced the rotation matrix

$$\mathbf{R}(\theta) = \begin{pmatrix} \cos(\theta) & -\sin(\theta) \\ \sin(\theta) & \cos(\theta) \end{pmatrix} . \tag{1.31}$$

From Equation (1.22), it is straightforward to show that the field quadrature operators satisfy the following commutation relation,

$$\left[\hat{X}^{\theta}, \hat{P}^{\theta}\right] = i . \tag{1.32}$$

1.2.3 Quantum statistics

We have seen that real system observables correspond to Hilbert space operators in quantum mechanics. This representation is better understood in the light of how measurements of the system observables are performed and what information they provide about the physical system [27].

Within the framework of quantum mechanics, system states are described by vectors in a Hilbert space $|\psi\rangle$, called *ket*, which are quantum states of maximal knowledge. According to the spectral theorem, the Hermitian Hilbert space operator $\hat{X}$ associated with a physical quantity X, can be decomposed into a sum

$$\hat{X} = \sum_j x_j \hat{\Pi}_j , \tag{1.33}$$

where $\{x_j\}$ is the set of real eigenvalues of the observable $\hat{X}$ which correspond to the possible outcome of a measurement of the physical quantity X. The operator $\hat{\Pi}_j = |\psi_j\rangle\langle\psi_j|$ is the projection operator (or projector) onto the subspace of eigenstates $|\psi_j\rangle$ of $\hat{X}$ with eigenvalue x_j. The set of projectors form an orthonormal basis of the observable's Hilbert space.

When measuring the physical quantity X for an arbitrary *a priori* state $|\Psi\rangle$, the probability that the result would be the eigenvalue x_j is given by

$$\Pr(X = x_j) = \frac{\langle\Psi|\hat{\Pi}_j|\Psi\rangle}{\langle\Psi|\Psi\rangle} . \tag{1.34}$$

This probability does not depend on the normalization of the state vector, thus we may consider only normalized states, i.e. $\langle\Psi|\Psi\rangle = 1$, for simplicity. Because the set $\{|\psi_j\rangle\}$ of eigenstates of $\hat{X}$ forms an orthonormal basis of the system states' Hilbert space, any arbitrary normalized state can be written as a linear combination of eigenstates $|\Psi\rangle = \sum_j \lambda_j|\psi_j\rangle$, with the normalization $\langle\Psi|\Psi\rangle = \sum_j |\lambda_j|^2 = 1$, such that the probability for the measurement to yield the result x_j is given by $\Pr(X = x_j) = |\lambda_j|^2$. The measurement

yielding the result x_j projects the system into a conditional *a posteriori* state

$$|\Psi'\rangle = \frac{\hat{\Pi}_j|\Psi\rangle}{\sqrt{\Pr(X=x_j)}} = \frac{\lambda_j}{|\lambda_j|}|\psi_j\rangle \ . \tag{1.35}$$

According to quantum mechanics, the result of a measurement cannot be predicted with certainty, except if the system is prepared in an eigenstate of the measured observable. Otherwise a measurement can only be expected to result in an eigenstate of the observable with a certain probability determined by the *a priori* state of the system. This probabilistic nature of measurement outcomes is inherent to the foundations of quantum mechanics, through the key principle known as *Born's rule*, and stands in stark contrast with classical physics where the result of a measurement can be predicted with certainty given prior complete knowledge of the system. As a consequence, it is of little interest to consider the result of a single probabilistic measurement, but rather the probability distribution of results obtained from an ensemble of measurements performed on identically prepared systems. The statistical properties of the measurement of an observable $\hat{X}$ can be characterized by the mean and variance, respectively given by

$$\langle\hat{X}\rangle = \sum_j x_j \Pr(X=x_j) = \sum_j x_j \langle\Psi|\hat{\Pi}_j|\Psi\rangle = \langle\Psi|\hat{X}|\Psi\rangle \ , \tag{1.36}$$

$$\mathrm{Var}(\hat{X}) = \langle(\hat{X}-\langle\hat{X}\rangle)^2\rangle = \langle\hat{X}^2\rangle - \langle\hat{X}\rangle^2 \ . \tag{1.37}$$

In the case of Gaussian states, which are the most readily available states in quantum optics experiments, the mean and variance fully characterize the probability distribution of measurement results.

1.2.4 Semi-classical picture

When considering the fluctuations associated with a bright monochromatic field, such as a strong laser beam, it is often advantageous to separate the field amplitude operator into its scalar mean $\langle\hat{a}\rangle = \alpha$, corresponding to the classical carrier field amplitude, and a noise operator $\delta\hat{a}(t)$, representing the fluctuations and modulations of the field, such that [20]

$$\hat{a}(t) = \alpha + \delta\hat{a}(t) \ . \tag{1.38}$$

These substitutions have the merit of simplifying the calculation of the quadrature variances, which then read

$$\mathrm{Var}(\hat{X}) = \frac{1}{2}\langle(\delta\hat{a}+\delta\hat{a}^\dagger)^2\rangle = \langle\delta\hat{X}^2\rangle \ , \quad \mathrm{Var}(\hat{P}) = -\frac{1}{2}\langle(\delta\hat{a}-\delta\hat{a}^\dagger)^2\rangle = \langle\delta\hat{P}^2\rangle \tag{1.39}$$

Moreover the reference to a bright field implies that the carrier mean field amplitude is much larger than any noise component, so that we may linearize any product of bright field amplitude operators by neglecting quadratic terms of the field fluctuations. A useful example is the linearization of the photon number operator that enters into the Hamiltonian giving the electromagnetic field energy in Equation (1.27). Moreover the photon number corresponds to the quantity measured by an ideal photodetector, and is therefore used in many theoretical description of measurements. The linearization of the photon number operator reads

$$\begin{aligned}\hat{n} &= \hat{a}^\dagger \hat{a} = (\alpha^* + \delta a^\dagger)(\alpha + \hat{a}) \\ &= |\alpha|^2 + |\alpha|(\delta\hat{a}e^{-i\phi_\alpha} + \delta\hat{a}^\dagger e^{i\phi_\alpha}) + \delta\hat{a}^\dagger\delta\hat{a} \\ &\approx |\alpha|^2 + \sqrt{2}|\alpha|\delta\hat{X}^{\phi_\alpha} \ , \end{aligned} \tag{1.40}$$

where we used the notation $\alpha = |\alpha|e^{i\phi_\alpha}$ and the definition of the field quadratures given in Equation (1.30).

A bright field in the semi-classical picture is best visualized in a *ball-on-stick* figure, where the mean carrier field amplitude is represented by a vector in phase space, and the field fluctuations are depicted as a ball with diameter given by the quadrature variances, positioned at the tip of the vector. A few examples of the representation of quantum states of light are given at the end of this Section (Figure 1.2).

1.2.5 Carrier and sideband noise

In 1.1.4 we introduced the classical sideband representation of a modulated field, where modulations applied onto a carrier field are depicted by a pair of upper and lower sideband frequency modes positioned at equal distance from the carrier mode on the frequency axis. Even in the absence of a modulation, quantum mechanics imposes that all sidebands of a carrier field are filled with non-null fluctuations due to the zero-point energy of the sideband mode fields $\hbar\Omega/2$. As a consequence the carrier field carries a broadband (white) amplitude and phase noise at sideband frequencies.

Considering a pair of upper and lower sideband modes at frequencies $\omega_{cw} \pm \Omega$, with ω_{cw} the carrier frequency, the linearized field amplitude operator reads

$$\hat{a}(t) = \alpha e^{-i\omega_{cw}t} + \frac{1}{\sqrt{2}}\left(\delta\hat{a}_+ e^{-i(\omega_{cw}+\Omega)t} + \delta\hat{a}_- e^{-i(\omega_{cw}-\Omega)t}\right) \ , \tag{1.41}$$

where the sideband fluctuation operators $\delta\hat{a}_\pm$ obey the bosonic commutation relation (1.26), and the factor of $1/\sqrt{2}$ ensures that $\hat{a}(t)$ does too. By assuming that the amplitude of the carrier field is much larger than the amplitude of the fluctuations in the

sidebands, we may use the linearization of the photon number operator (1.40) to write

$$\begin{aligned}\hat{n} &= |\alpha|^2 + \frac{|\alpha|}{\sqrt{2}}\left[(\delta\hat{a}_+ e^{-i\Omega t} + \delta\hat{a}_- e^{i\Omega t})e^{-i\phi_\alpha} + (\delta\hat{a}_+^\dagger e^{i\Omega t} + \delta\hat{a}_-^\dagger e^{-i\Omega t})e^{i\phi_\alpha}\right] \\ &= |\alpha|^2 + |\alpha|\left[\delta\hat{X}_+^{\phi_\alpha}\cos(\Omega t) + \delta\hat{P}_+^{\phi_\alpha}\sin(\Omega t) + \delta\hat{X}_-^{\phi_\alpha}\cos(\Omega t) - \delta\hat{P}_-^{\phi_\alpha}\sin(\Omega t)\right] \\ &= |\alpha|^2 + |\alpha|\left[(\delta\hat{X}_+^{\phi_\alpha} + \delta\hat{X}_-^{\phi_\alpha})\cos(\Omega t) + (\delta\hat{P}_+^{\phi_\alpha} - \delta\hat{P}_-^{\phi_\alpha})\sin(\Omega t)\right] \ , \end{aligned} \tag{1.42}$$

where it appears that the fluctuation in the photon number at a frequency Ω is a result of the simultaneous beating of the carrier with the upper and lower sidebands at frequencies $\omega_{cw} \pm \Omega$. Identification of the noise terms in Equations (1.40) and (1.42) further shows that the carrier field quadrature fluctuations arise from a cyclic mixing of conjugate sideband field quadrature fluctuations,

$$\delta\hat{X}^{\phi_\alpha}(t) = \frac{\delta\hat{X}_+^{\phi_\alpha} + \delta\hat{X}_-^{\phi_\alpha}}{\sqrt{2}}\cos(\Omega t) + \frac{\delta\hat{P}_+^{\phi_\alpha} - \delta\hat{P}_-^{\phi_\alpha}}{\sqrt{2}}\sin(\Omega t) \ . \tag{1.43}$$

1.2.6 Frequency domain and power spectra

In the preceding subsection we have observed that the carrier field quadrature fluctuations are composed of the cyclic mixing of conjugate quadrature fluctuations from the sidebands. In order to study the contribution of each sideband to the carrier field fluctuations, it i convenient to resolve the field fluctuations in the frequency domain. We start by describing the sidebands as a continuum of optical modes with frequency dependent field amplitude operators, $\hat{\boldsymbol{a}}(\Omega)$, where the frequency Ω is defined relative to the carrier frequency ω_{cw}. Given the commutation relations (1.26), the two-frequency commutation relation of sideband modes can be derived [22],

$$\left[\hat{\boldsymbol{a}}(\Omega), \hat{\boldsymbol{a}}^\dagger(\Omega')\right] = \delta(\Omega - \Omega') \ . \tag{1.44}$$

The time dependent creation and annihilation operators are related to the frequency dependent operators via the Fourier transform,

$$\hat{a}(t) = \frac{1}{\sqrt{2\pi}}\int_{-\infty}^{+\infty} \hat{\boldsymbol{a}}(\Omega)e^{-i\Omega t}d\Omega \ , \tag{1.45}$$

$$\hat{a}^\dagger(t) = [\hat{a}(t)]^\dagger = \frac{1}{\sqrt{2\pi}}\int_{-\infty}^{+\infty} \hat{\boldsymbol{a}}^\dagger(\Omega)e^{i\Omega t}d\Omega \ , \tag{1.46}$$

and obey the two-time commutation relation,

$$\left[\hat{a}(t), \hat{a}(t')\right] = \delta(t - t') \ . \tag{1.47}$$

The field quadrature operators then satisfy the commutation relations in frequency and time domain, respectively,

$$\left[\hat{\mathcal{X}}(\Omega), \hat{\mathcal{P}}(\Omega')\right] = i\delta(\Omega + \Omega') \ , \tag{1.48}$$

$$\left[\hat{X}(t), \hat{P}(t')\right] = i\delta(t - t') \ . \tag{1.49}$$

Experimentally, the fluctuations of each optical sideband mode are resolved by Fourier decomposition of the photocurrent obtained by directing the carrier beam onto a photodetector. However the Fourier transform of a time-dependent stochastic observable $\delta\hat{X}(t)$ does not exist in general, but we may define a truncated Fourier transform,

$$\delta\hat{\mathcal{X}}_\tau(\Omega) = \frac{1}{\sqrt{2\tau}} \int_{-\tau}^{\tau} \delta\hat{X}(t) e^{i\Omega t} dt. \tag{1.50}$$

The truncated Fourier transform makes more sense from an experimental point of view than the Fourier transform, as real measurement times are finite. Averaging over independent measurements gives the spectral variance $\langle|\delta\hat{\mathcal{X}}_\tau(\Omega)|^2\rangle$. Under the condition that $\delta\hat{X}(t)$ is a weak-sense stationary process, and in the limit of very long measurement times, i.e. $\tau \to \infty$, the Wiener-Khinchin theorem relates this spectral variance to the Fourier transform of the autocorrelation function [19],

$$S_{\delta\hat{X}}(\Omega) = \lim_{\tau\to\infty} \langle|\delta\hat{\mathcal{X}}_\tau(\Omega)|^2\rangle = \int_{-\infty}^{+\infty} \langle\delta\hat{X}(t)\delta\hat{X}(0)\rangle e^{i\Omega t} dt, \tag{1.51}$$

which is called the *power spectral density* (PSD). The PSD is linked to the expectation value of the product of frequency modes, i.e. the frequency correlation function, by the relation

$$\langle\delta\hat{\mathcal{X}}(\Omega)\delta\hat{\mathcal{X}}(\Omega')\rangle = S_{\delta\hat{X}}(\Omega)\delta(\Omega + \Omega') \ . \tag{1.52}$$

Furthermore, using the inverse Fourier transform on the PSD leads to a direct relation between the area under the PSD and the variance of the observable,

$$\frac{1}{2\pi} \int_{-\infty}^{+\infty} S_{\delta\hat{X}}(\Omega) d\Omega = \langle\delta\hat{X}^2\rangle \ . \tag{1.53}$$

Coming back to Equation (1.43), we calculate the spectral variance at frequency Ω of the carrier field quadrature fluctuations,

$$\langle|\delta\hat{\mathcal{X}}^{\phi_\alpha}(\Omega)|^2\rangle = \frac{1}{4}\left[\langle(\delta\hat{X}_+^{\phi_\alpha} + \delta\hat{X}_-^{\phi_\alpha})^2\rangle + \langle(\delta\hat{P}_+^{\phi_\alpha} - \delta\hat{P}_-^{\phi_\alpha})^2\rangle\right] \tag{1.54}$$

$$= \frac{1}{4}\left[\langle(\delta\hat{X}_+^{\phi_\alpha})^2\rangle + \langle(\delta\hat{X}_-^{\phi_\alpha})^2\rangle + \langle(\delta\hat{P}_+^{\phi_\alpha})^2\rangle + \langle(\delta\hat{P}_-^{\phi_\alpha})^2\rangle\right] + \frac{1}{2}\left[\langle(\delta\hat{X}_+^{\phi_\alpha}\delta\hat{X}_-^{\phi_\alpha})^2\rangle - \langle(\delta\hat{P}_+^{\phi_\alpha}\delta\hat{P}_-^{\phi_\alpha})^2\rangle\right] \ , \tag{1.55}$$

which results in a combination of the variances of upper and lower sideband conjugate quadrature fluctuations. The last line in Equation (1.55) contains the possible correlations between upper and lower sideband fluctuations, and is a key term for the understanding and realization of quantum-enhanced sensing as developed in Chapter 3 of this thesis.

1.2.7 Quantum states of light

In the language of quantum mechanics, physical systems are characterized by a state which determines the expectation values of the system's observables, and consequently the result of measurements of these observables on the system. Here we present a few categories of quantum states that are relevant for a good understanding of this thesis.

Fock states

First and foremost are the energy eigenstates of an harmonic oscillator, which are called *Fock states*, and represents the occupancy of the system by quanta of energy. In the present thesis we primarily deal with mechanical and optical resonators in which the quanta of energy are the well-known phonon and photon, respectively. Following upon the quantization of the electromagnetic field, the set of Fock states $|n\rangle$ ($n \in \mathbb{N}$) describing systems with n photons is an orthonormal set of eigenstates of the number operator $\hat{n}$, defined by

$$\hat{n}|n\rangle = n\hat{n} \ , \qquad \langle n|n'\rangle = \delta_{nn'} \ , \qquad \sum_n |n\rangle\langle n| = 1 \ . \tag{1.56}$$

Because of this definition Fock states are also called *number states*.

The annihilation and creation operators, $\hat{a}$ and $\hat{a}^\dagger$, remove and add a quantum of energy to a number state such that

$$\hat{a}|n\rangle = \sqrt{n}|n-1\rangle \ , \qquad \hat{a}^\dagger|n\rangle = \sqrt{n+1}|n+1\rangle \ . \tag{1.57}$$

The orthogonality of number states therefore imposes that the expectation value of the annihilation and creation operators, and consequently of the field quadrature operators, is null, i.e.

$$\langle\hat{a}\rangle = \langle n|\hat{a}|n\rangle = \langle\hat{a}^\dagger\rangle = 0 \ , \qquad \langle\hat{X}^\theta\rangle = \langle\hat{P}^\theta\rangle = 0 \ . \tag{1.58}$$

Furthermore the variance of the field quadratures increases with the occupation number, reading

$$\langle(\delta\hat{X}^\theta)^2\rangle = \langle(\delta\hat{P}^\theta)^2\rangle = n + \frac{1}{2} \ , \tag{1.59}$$

which is explained by the fact that the phase of a number state is not defined.

The state with zero occupation $|0\rangle$ is coined the *vacuum state* and represents the zero-point energy state of the system. The non-zero variance of the field quadrature operators indicates that the vacuum state is not free of fluctuations. The vacuum state is a *state of minimum uncertainty* in the sense that the magnitude of its fluctuations is at the minimum level allowed by the uncertainty principle. The noise induced by vacuum fluctuations on the measurement of a system observable is often referred as *quantum noise* or *shot noise*.

Coherent states

Due to its undefined phase and zero mean, it appears unlikely that a Fock state could represent the state of a classical sinusoidal monochromatic wave such as a laser beam, even in the limit of high number of photons which is often considered the classical limit. For this purpose it is more convenient to employ the so-called *coherent states* which are said to be the "most classical" quantum states of a harmonic oscillator.

Coherent states are defined as the normalized eigenstates of the annihilation operator,

$$\hat{a}|\alpha\rangle = \alpha|\alpha\rangle \ , \qquad \langle\alpha|\hat{a}^\dagger = \alpha^*\langle\alpha| \ , \qquad \langle\alpha|\alpha\rangle = 1 \ . \tag{1.60}$$

In this way the classical electric field in Equation (1.11) can be interpreted as the expectation value of the quantized electric field in Equation (1.23), for a system in a coherent state. The complex eigenvalue α can then be related to the electromagnetic field amplitude.

By evaluating the expectation value and the variance of the number operator,

$$\langle\hat{n}\rangle = \langle\alpha|\hat{a}^\dagger\hat{a}|\alpha\rangle = |\alpha|^2 \ , \tag{1.61}$$

$$\mathrm{Var}(\hat{n}) = \langle\alpha|\hat{a}^\dagger\hat{a}\hat{a}^\dagger\hat{a}|\alpha\rangle - \langle\alpha|\hat{a}^\dagger\hat{a}|\alpha\rangle^2 = |\alpha|^2 \ , \tag{1.62}$$

we notice that they are equal which is characteristic of a Poisson distribution. Indeed it can be shown that the photon number probability distribution of a coherent state follows a Poisson distribution

$$\Pr(n) = |\langle n|\alpha\rangle|^2 = \frac{|\alpha|^{2n}}{n!}e^{-|\alpha|^2} \ . \tag{1.63}$$

The coherent states are quantum states that closely resemble classical states, but they display their quantum features in the form of quantum fluctuations. Coherent states are states of minimum uncertainty as the variances of their field quadratures

equal those of a vacuum state,

$$\langle(\delta\hat{X}^\theta)^2\rangle = \langle(\delta\hat{P}^\theta)^2\rangle = \frac{1}{2} \ . \tag{1.64}$$

In a phase space representation, the coherent state can be viewed as a vacuum state displaced in amplitude and phase quadratures by amounts given by the expectation value of the field quadrature operators,

$$\langle\hat{X}\rangle = \frac{1}{\sqrt{2}}(\alpha+\alpha^*) = \sqrt{2}\,\mathrm{Re}(\alpha) \ , \qquad \langle\hat{P}\rangle = \frac{1}{i\sqrt{2}}(\alpha-\alpha^*) = \sqrt{2}\,\mathrm{Im}(\alpha) \ , \tag{1.65}$$

as pictured on Figure 1.2.

Thermal states

An harmonic oscillator in thermal equilibrium with its environment is described by a thermal state. This situation applies to the radiation of a black body, and is famously known for the derivation of the Planck radiation law. More relevant to this thesis, the thermal state is the state of a mechanical resonator in thermal equilibrium with its environment.

The thermal state is not a pure state, meaning that it cannot be described by a state vector but rather by a density operator [21],

$$\hat{\rho}_{th} = \frac{\exp\left(-\frac{\hbar\omega}{k_B T}[\hat{n}+\frac{1}{2}]\right)}{\mathrm{Tr}\left[\exp\left(-\frac{\hbar\omega}{k_B T}[\hat{n}+\frac{1}{2}]\right)\right]} \ , \tag{1.66}$$

where T is the temperature of the environment, k_B is the Boltzmann constant, and ω is the natural frequency of the harmonic oscillator (cf. Equation (1.27)). The expectation value of an observable $\hat{X}$ for a state described by a density operator $\hat{\rho}$ is given by $\langle\hat{X}\rangle = \mathrm{Tr}(\hat{\rho}\hat{X})$. Using this formula the mean and variance of the number operator for a thermal state can be calculated [21], resulting in

$$\langle\hat{n}\rangle = \frac{1}{\exp(\hbar\omega/k_B T)-1} \ , \qquad \mathrm{Var}(\hat{n}) = \langle\hat{n}\rangle + \langle\hat{n}\rangle^2 \ . \tag{1.67}$$

We may also calculate the expectation value and variance of the field quadrature operators

$$\langle\hat{X}^\theta\rangle = \langle\hat{P}^\theta\rangle = 0 \ , \tag{1.68}$$

$$\langle(\delta\hat{X}^\theta)^2\rangle = \langle(\delta\hat{P}^\theta)^2\rangle = \langle\hat{n}\rangle + \frac{1}{2} \ . \tag{1.69}$$

Similar to the number state, the thermal state has no defined phase (cf. Figure 1.2). In the limit of high thermal excitation of the harmonic oscillator, $k_BT \gg \hbar\omega$, the mean number of quanta can be approximated by $\langle\hat{n}\rangle \approx k_BT/\hbar\omega$. This is usually the case for a macroscopic mechanical resonator at room temperature. On the other hand for a system where the thermal energy provided by the environment is much smaller than the quantum of energy of the harmonic oscillator, $k_BT \ll \hbar\omega$, the expected occupancy is much lower than one, i.e. $\langle\hat{n}\rangle \approx \exp(-\hbar\omega/k_BT) \ll 1$, and the thermal state approaches the vacuum state. This is the case for optical fields in thermal equilibrium at room temperatures ($\langle\hat{n}\rangle \sim 10^{-7}$) which is the reason why the optical sidebands in the absence of modulation can be considered to be in a vacuum state.

Quadrature squeezed states

Quadrature squeezed states are quantum states that possess a reduced noise variance below the shot noise level in one quadrature, coined the *squeezed quadrature*. In order to not violate Heisenberg uncertainty principle, quadrature squeezed states must compensate with excess noise above the shot noise level in the conjugate quadrature, also referred to as the *anti-squeezed quadrature*. Mathematically, this translates into

$$\langle(\delta\hat{X}^\theta)^2\rangle < \frac{1}{2}\,, \qquad \langle(\delta\hat{P}^\theta)^2\rangle > \frac{1}{2}\,, \qquad \langle(\delta\hat{X}^\theta)^2\rangle\langle(\delta\hat{P}^\theta)^2\rangle \geq \frac{1}{4}\,, \tag{1.70}$$

for an arbitrary squeezed quadrature $\hat{X}^\theta$.

Squeezed states are generated mathematically by the action of the *squeezing operator* [21],

$$\hat{S}(\xi) = e^{\frac{1}{2}(\xi^*\hat{a}^2 - \xi\hat{a}^{\dagger 2})} = e^{\frac{ir_s}{2}(\hat{X}^{\theta_s}\hat{P}^{\theta_s} + \hat{X}^{\theta_s}\hat{P}^{\theta_s})}\,, \tag{1.71}$$

where $\xi = r_s e^{2i\theta_s}$, with $r_s \in \mathbb{R}^+$ the *squeeze parameter* and θ_s the *squeezing angle*. The squeezing operator describes a nonlinear process that creates correlations between pairs of quanta, e.g. photons. We will refer to amplitude and phase quadrature squeezing when $\theta_s = 0$ and $\theta_s = \pi/2$, respectively.

Squeezing of an arbitrary quadrature $\hat{X}^\theta$ reads

$$\hat{S}^\dagger(\xi)\hat{X}^\theta\hat{S}(\xi) = \hat{X}^\theta\cosh(r_s) - \hat{X}^{2\theta_s-\theta}\sinh(r_s)\,, \tag{1.72}$$

and the conjugate quadrature variances of a squeezed vacuum state $\hat{S}|0\rangle$ are given by

$$\langle(\delta\hat{X}^\theta)^2\rangle = \frac{1}{2}\left[\cosh^2(r_s) + \sinh^2(r_s) - 2\cos(2\theta - 2\theta_s)\cosh(r_s)\sinh(r_s)\right]\,, \tag{1.73}$$

$$\langle(\delta\hat{P}^\theta)^2\rangle = \frac{1}{2}\left[\cosh^2(r_s) + \sinh^2(r_s) + 2\cos(2\theta - 2\theta_s)\cosh(r_s)\sinh(r_s)\right]\,. \tag{1.74}$$

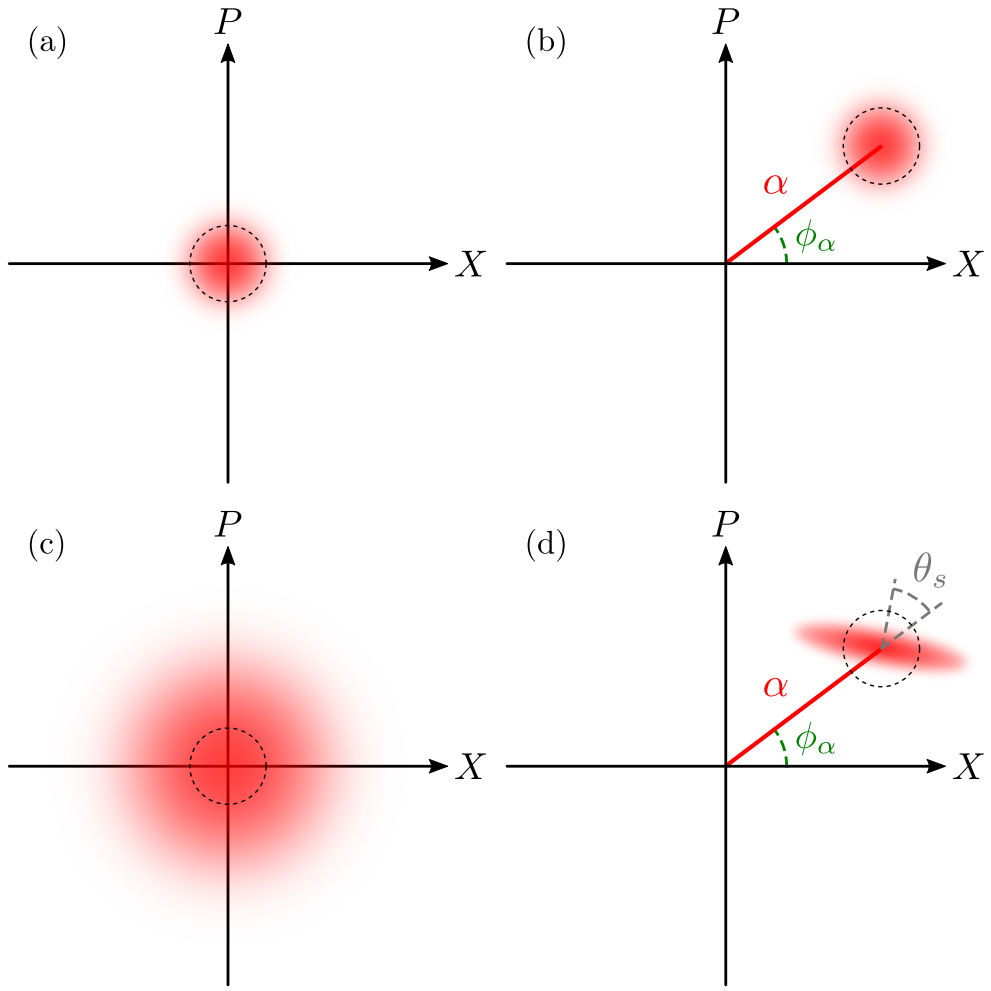

FIGURE 1.2: Ball-on-stick representation of quantum states in phase space. (a) Vacuum state , (b) coherent state, (c) thermal state, (d) bright quadrature squeezed state. The black dashed circle indicates the quadrature variance of the vacuum state.

Unlike the coherent and vacuum states, quadrature squeezed states may possess correlations between conjugate quadrature fluctuations, yielding

$$\langle \delta\hat{X}^\theta \delta\hat{P}^\theta + \delta\hat{P}^\theta \delta\hat{X}^\theta \rangle = 2\cosh(r_s)\sinh(r_s)\sin(2\theta - 2\theta_s) \ , \tag{1.75}$$

for a squeezed vacuum state. The quadrature angles for which the variances of conjugate quadratures reaches a minimum and a maximum, and are uncorrelated, are $\theta = \theta_s$ and $\theta = \theta_s + \pi/2$.

1.3 Detection of light

Along with the development of quantum mechanics, and quantum optics in particular, numerous sophisticated experimental techniques have been developed to put the theory

to the test and observe the quantum behavior of light [20]. A few of these techniques have been employed for the experiments presented in this thesis and are reviewed in this section.

In quantum optics experiment, light is the main tool that gathers, carries and delivers information about a quantum system, which could be, for example, the light itself, a solid state system, or a mechanical oscillator. It is therefore essential to employ effective and efficient means to extract this information. There exist various ways that information can be encoded and carried by the light, and there exist as many optical detection techniques to collect it. For example, one might be interested in the photon statistics of the light field, requiring single photon or photon resolving detectors, i.e. *intensity detection* techniques, while another might want to measure the phase or amplitude modulations imprinted onto an optical field, thus needing a broadband phase-sensitive detector, i.e. a *field detection* technique. In general an optical field cannot be measured and processed directly due to its high frequency, much faster than conventional electronic measurement devices, but it can be measured indirectly by interfering it with a known reference optical field, commonly called the *local oscillator* (LO), such that modulations of the amplitude or phase are mixed down to lower frequencies that can be resolved with an intensity detector and processed with conventional electronic devices.

1.3.1 Intensity detector

The most basic intensity detector employed in the experiments presented in this thesis is a reverse-biased semiconductor PIN photodiode that relies on the photo-electric effect to convert the optical field energy into a photocurrent. It is a destructive detector in the sense that extracting information from the optical field irremediably destroys the carrier of information due to absorption of the optical energy.

Practically, an intensity photodetector is characterized by a quantum efficiency η_{QE} which describes the probability for a photon impinging onto the detector to be converted into a measurable signal. For a photodiode, the quantum efficiency is obtained as the ratio of the rate of electron generation over the rate of photon absorption. It can be calculated from the value of the *spectral responsivity* R_λ (in A/W) specified by the manufacturer of the photodiode, $\eta_{QE} = (hc/q_e) \cdot R_\lambda/\lambda$, with q_e the electron charge. The quantum efficiency represents the loss experienced by the optical field upon detection.

As the name indicates, an intensity detector measures the intensity of an optical field, which is proportional to the square of the field amplitude. An intensity detector is therefore able to measure amplitude modulations of the optical field due to the beating of the carrier field with the modulated sidebands, which mixes down the sideband

component to an AC component of the photocurrent which can be processed by conventional electronic devices. This is easily seen by deriving the classical photocurrent from Equation (1.14),

$$i_{det}(t) \propto |E_{AM}(t)|^2 \approx E^2 + 2EM\sin(\Omega_{mod}t) \ , \tag{1.76}$$

where we have neglected quadratic terms of the sideband modulation. The result of the intensity detection is quite different in case of a phase modulation because the lower and upper sideband beat signals interfere destructively, thus the photocurrent carries no modulation.

In the language of quantum mechanics the photocurent produced by an intensity detector is proportional to the photon number operator (cf Equation (1.40))

$$i_{det}(t) = g_{det}\hat{n}(t) \approx g_{det}\left(|\alpha|^2 + \sqrt{2}|\alpha|\delta\hat{X}^{\phi_\alpha}\right) \ , \tag{1.77}$$

with g_{det} the gain of the detector. In accordance with the classical case, the intensity detector can only measure the amplitude quadrature of the light field, and a phase sensitive detection scheme, such as homodyne detection, is necessary to measure an arbitrary quadrature.

1.3.2 Optical loss

In a classical picture, optical loss results in a reduction of the optical power that is modeled by an input-output relation $P_{out} = \eta P_{in}$, with $\eta < 1$. However this representation turns out to be incomplete in the quantum picture, as scaling down the field operators $\hat{a}_{out} = \sqrt{\eta}\hat{a}_{in}$ does not preserve the commutation relations, $[\hat{a}_{out}, \hat{a}^\dagger_{out}] = \eta[\hat{a}_{in}, \hat{a}^\dagger_{in}] = \eta \neq 1$. The solution to this problem comes by adding vacuum fluctuations from a loss mode, what is equivalent to modeling the loss by the interference of the optical field with a vacuum field on a beam splitter with transmittivity η [21].

The input-output relations for a (lossless) beam splitter with input fields $\hat{a}_{in}$ and $\hat{b}_{in}$, and transmittivity η (Figure 1.3(a)) are given by

$$\hat{a}_{out} = \sqrt{\eta}\hat{a}_{in} + \sqrt{1-\eta}\hat{b}_{in} \ , \tag{1.78}$$

$$\hat{b}_{out} = \sqrt{\eta}\hat{b}_{in} - \sqrt{1-\eta}\hat{a}_{in} \ , \tag{1.79}$$

where the minus sign in Equation (1.79) accounts for the $\pi/2$ phase shift experienced by the fields upon reflection. It is straightforward to check that the canonical commutation relations are now obeyed by the two output fields, $[\hat{a}_{out}, \hat{a}^\dagger_{out}] = [\hat{b}_{out}, \hat{b}^\dagger_{out}] = 1$.

The classical representation of optical loss holds for the mean photon number of a bright field, which is proportional to the optical power. For example, the output mean

photon number of a coherent state $|\alpha\rangle$, is given by,

$$\langle \hat{n}_{out} \rangle = \langle \hat{a}^{\dagger}_{out} \hat{a}_{out} \rangle = \eta \langle \hat{a}^{\dagger}_{in} \hat{a}_{in} \rangle = \eta |\alpha|^2 \ . \tag{1.80}$$

The quantum representation is particularly relevant when looking at the small fluctuations of the fields, whose quadrature variances suffer from loss in accordance with,

$$\langle (\delta \hat{X}^{\theta}_{out})^2 \rangle = \eta \langle (\delta \hat{X}^{\theta}_{in})^2 \rangle + \frac{(1-\eta)}{2} \ . \tag{1.81}$$

For an input coherent state, the variances of the field quadrature fluctuations are not affected by loss because the field fluctuations of the coherent and vacuum state are both completely uncorrelated. On the other hand, the noise correlations carried by a squeezed state are blurred by the uncorrelated noise introduced by the vacuum state, which leads to a reduction of the squeezing strength (cf. Figure 1.3(b)). For this reason, it is essential to reduce loss in quantum optics experiments which make use of field correlations, such as the quantum-enhanced sensitivity measurements that are described in Chapter 3.

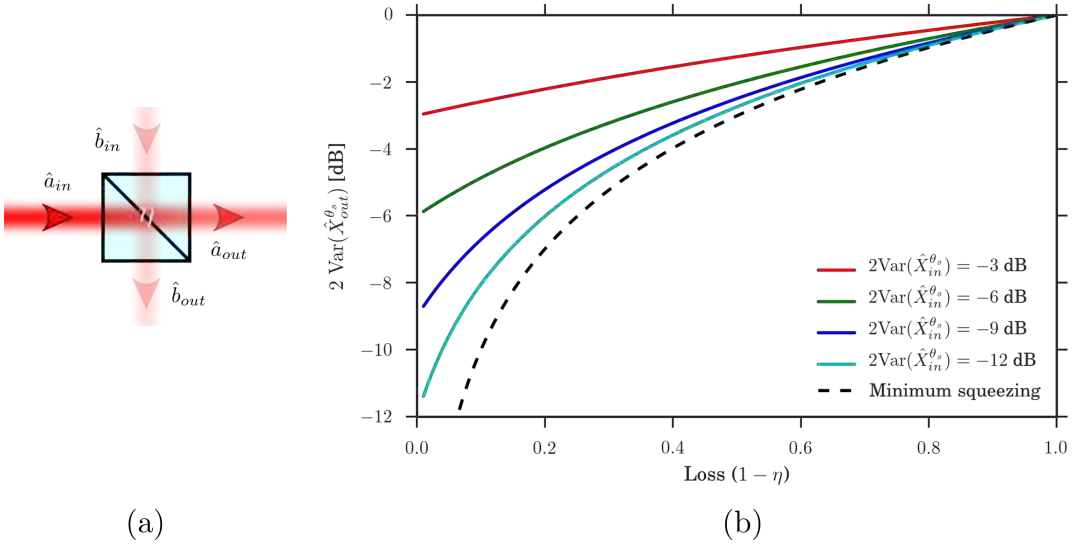

(a) (b)

FIGURE 1.3: (a) Model of a beam splitter with transmittivity η. In quantum optics, optical loss are represented by interfering the optical field $\hat{a}_{in}$ with a vacuum field $\hat{b}_{in}$ on a beam splitter. The mixing of uncorrelated vacuum field fluctuations with the input field fluctuations damages any correlation on the input noise, such as squeezed quadrature fluctuations. (b) Degradation of the squeezed quadrature variance, $\mathrm{Var}(\hat{X}^{\theta_s}_{out})$, for increasing optical loss $(1-\eta)$, and for various initial squeezing strength. The dashed line indicates the minimum squeezed variance achievable in the presence of loss.

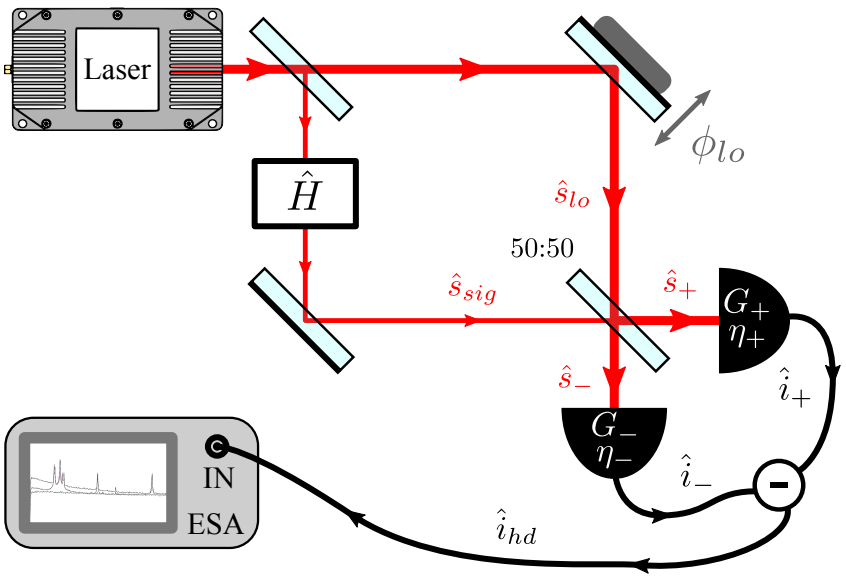

FIGURE 1.4: Schematic of a balanced homodyne detector.

1.3.3 Balanced homodyne detector

Direct detection of an optical field intensity cannot provide information about the phase quadrature fluctuations of the field, and alternative detection techniques are therefore needed. Homodyne detection allows measurements on an arbitrary field quadrature by interfering a signal field with a reference field whose phase and amplitude are known, and which is called the local oscillator (LO). Both the signal field and the LO have the same carrier frequency such that the intensity of the combined optical fields presents modulations of the signal and LO sidebands in a quadrature determined by the relative phase between the signal field and the LO. Balanced homodyne detection further implies that the signal field and the LO are interfered onto a 50:50 beam splitter, then both outputs of the beam splitter are directly detected. By taking the difference of the two detector outputs, it is possible to cancel the classical noise carried by the LO while boosting the signal measured from the modulation of the signal field.

A schematic of a typical balanced homodyne detection setup is shown on Figure 1.4. The LO and the signal field are commonly derived from the same laser beam, so that they oscillate at the same frequency and occupy the same spatial mode. Information is then encoded onto the signal field by some process $\hat{H}$, which could be an unknown measurement interaction with a physical system, or a chosen modulation for optical communication, for example. Formally we consider both the LO and the signal field to

be bright fields represented in the semi-classical picture by

$$\hat{s}_{sig}(t) = \bar{s}_{sig} + \delta\hat{s}_{sig}(t) \ , \tag{1.82}$$

$$\hat{s}_{lo}(t) = [\bar{s}_{lo} + \delta\hat{s}_{lo}(t)]\, e^{i\phi_{lo}} \ , \tag{1.83}$$

where $\bar{s}_{sig} = \langle\hat{s}_{sig}\rangle$ and $\bar{s}_{lo} = |\langle\hat{s}_{lo}\rangle|$ are the mean field amplitudes chosen to be real such that the phase of the LO relative to the signal field is ϕ_{lo}. The LO phase can be controlled by tuning the optical path-length of the local oscillator, what can be achieved in free space by displacing a mirror mounted on a piezoelectric element, or in optical fibers by altering the refractive index via the Pockel effect with an electro-optic modulator (EOM).

Considering first the case of an unbalanced homodyne detector, the signal and the LO fields are interfered on a beam splitter with transmittivity ε, resulting in the fields

$$\hat{s}_{+}(t) = \sqrt{\varepsilon}\hat{s}_{sig}(t) + \sqrt{1-\varepsilon}\hat{s}_{lo}(t) \ , \tag{1.84}$$

$$\hat{s}_{-}(t) = \sqrt{\varepsilon}\hat{s}_{lo}(t) - \sqrt{1-\varepsilon}\hat{s}_{sig}(t) \ . \tag{1.85}$$

Each field is directed toward a photodetector which provides a current signal proportional to the photon flux in the field. Imperfect mode matching of the LO with the signal field and nonunity detection efficiency of the photodetectors can be modeled as loss through a beam splitter, such that the detected fields read

$$\hat{s}_{d\pm}(t) = \sqrt{\eta_{\pm}}\hat{s}_{\pm}(t) + \sqrt{1-\eta_{\pm}}\delta\hat{s}_{v\pm}(t) \ , \tag{1.86}$$

where $\eta_{\pm}$ represent the detection loss in each detection path, and $\delta\hat{s}_{v\pm}$ represent the admixed vacuum field fluctuations. The photocurrents produced by the two photodetectors are proportional to the intensity of the detected fields and can be written,

$$\hat{i}_{\pm}(t) = G_{\pm}\hat{s}^{\dagger}_{d\pm}(t)\hat{s}_{d\pm}(t) \ , \tag{1.87}$$

where $G_{\pm}$ represent the gain of the photodetectors, including the transformation of a photon flux into an electron current.

The two photocurrents are subtracted, and split into a DC and AC components by use of frequency filters. The resulting DC current is proportional to the intensity of the interference between the LO and the signal field, and is given by

$$\begin{aligned}\bar{i}_{hd} =& \langle\hat{i}_{+} - \hat{i}_{-}\rangle \\ =& \eta_{+}G_{+}\left[(1-\varepsilon)\bar{s}^2_{lo} + \varepsilon\bar{s}^2_{sig}\right] - \eta_{-}G_{-}\left[\varepsilon\bar{s}^2_{lo} + (1-\varepsilon)\bar{s}^2_{sig}\right] \\ &+ 2\bar{s}_{lo}\bar{s}_{sig}\left(\eta_{+}G_{+} + \eta_{-}G_{-}\right)\sqrt{\varepsilon(1-\varepsilon)}\cos(\phi_{lo}) \ ,\end{aligned} \tag{1.88}$$

It is dependent on the phase of the LO relative to the signal field, and can be used as an error signal to lock the phase of the LO.

The AC component of the difference current is given by

$$\begin{aligned}\delta\hat{i}_{hd} =& \hat{i}_+ - \hat{i}_- - \langle \hat{i}_+ - \hat{i}_- \rangle && (1.89)\\ \approx& \left[G_+\eta_+(1-\varepsilon) - G_-\eta_-\varepsilon\right]\sqrt{2}\bar{s}_{lo}\delta\hat{X}_{lo} + \left[G_+\eta_+ + G_-\eta_-\right]\sqrt{2\varepsilon(1-\varepsilon)}\bar{s}_{lo}\delta\hat{X}^{\phi_{lo}}_{sig}\\ &+ G_+\sqrt{2\eta_+(1-\eta_+)(1-\varepsilon)}\bar{s}_{lo}\delta\hat{X}^{\phi_{lo}}_{v+} + G_-\sqrt{2\eta_-(1-\eta_-)\varepsilon}\bar{s}_{lo}\delta\hat{X}^{\phi_{lo}}_{v-} \ , && (1.90)\end{aligned}$$

where we used the bright field assumption to neglect second order noise terms, and assumed that the LO is much brighter than the output signal, i.e. $\bar{s}_{lo} \gg \bar{s}_{out}$, in order to remove linear contributions in the mean signal field amplitude $\bar{s}_{sig}$. This condition is essential for enhancing the measurement of the signal field quadrature $\delta\hat{X}^{\phi_{lo}}_{sig}$ over the signal amplitude noise and the LO noise.

To further suppress the LO noise contribution to the difference current, the homodyne detector must be balanced by fulfilling the condition,

$$G_+\eta_+(1-\varepsilon) = G_-\eta_-\varepsilon \ . \tag{1.91}$$

In practice the detection efficiencies and gains of the photodetectors are fixed by their design and fabrication, what leaves little room for the tuning of $G_\pm$ and $\eta_\pm$. On the other hand the beam splitting ratio ε of the homodyne detector can be easily adjusted by using a combination of two polarizing beam splitters (PBS) and a half-wave plate (HWP). In such a configuration, the signal and LO fields are combined on an initial PBS in orthogonal polarization modes, s and p. Then their respective polarizations are rotated by the HWP such that both fields have components in the s and p polarizations. These components are finally interfered on the second PBS by projection onto the s and p polarization modes. The splitting ratio of the LO and signal fields can therefore be controlled by turning the HWP. Balancing the homodyne detector is then easily achieved by canceling the DC part of the difference current while blocking the signal field, i.e. $\bar{i}_{hd} = 0$ for $\bar{s}_{sig} = 0$.

For a balanced homodyne detector the DC and AC difference currents simplify to

$$\begin{aligned}\bar{i}_{hd} =& (\eta_+G_+ - \eta_-G_-)\bar{s}^2_{sig} + 2\eta_{hd}G_{hd}\bar{s}_{lo}\bar{s}_{sig}\cos(\phi_{lo}) \ , && (1.92)\\ \delta\hat{i}_{hd} =& \sqrt{2}G\bar{s}_{lo}\left[\eta\delta\hat{X}^{\phi_{lo}}_{sig} + \sqrt{(1-\eta_+)\eta_-\varepsilon}\delta\hat{X}^{\phi_{lo}}_{v+} + \sqrt{\eta_+(1-\eta_-)(1-\varepsilon)}\delta\hat{X}^{\phi_{lo}}_{v-}\right] . && (1.93)\end{aligned}$$

where we have introduced the homodyne detection loss and gain parameters, $\eta_{hd} = \sqrt{\eta_+\eta_-}$ and $G_{hd} = \sqrt{G_+G_-}$, respectively. It is now clear that the difference current carries the signal field fluctuations (including detection loss) in the quadrature determined by the phase ϕ_{lo}. The power spectral density of the signal field fluctuations in an

arbitrary quadrature can then be extracted from the difference current,

$$\langle|\delta\hat{i}_{hd}(\Omega)|^2\rangle = \eta_{hd}G_{hd}^2\bar{s}_{lo}^2\left[2\eta_{hd}\langle|\delta\hat{X}_{sig}^{\phi_{lo}}(\Omega)|^2\rangle + \sigma - \eta_{hd}\right] , \tag{1.94}$$

where $\sigma = (1-\varepsilon)\sqrt{\eta_+/\eta_-} + \varepsilon\sqrt{\eta_-/\eta_+}$ is unity for equal detection loss at the two photodiodes, or equivalently equal gain of the photodetectors. Eventually the balanced homodyne detector is equivalent to a detector that measures the signal field quadrature $\delta\hat{X}_{sig}^{\phi_{lo}}$, with quantum efficiency η_{hd} and gain $2\eta_{hd}G_{hd}^2\bar{s}_{lo}^2$.

Visibility of interference

Homodyne detection relies on the interference of the LO and signal fields to measure an arbitrary quadrature of the signal field fluctuations. The quality of the interference depends on the efficient mode matching of the LO and signal fields, i.e. the spatial overlap of their mode profiles and the accordance of their polarization vectors. Any deviation from a perfect mode matching translates into an increase in detection loss. In practice the interference can hardly be perfect due to slight misalignment and astigmatism of optical components such as mirrors or lenses, that distort the spatial profile of the optical fields.

Considering the interference of classical LO and signal fields on a beam splitter with transmittivity ε, the efficiency of the mode matching can be represented by a parameter η_m such that the LO and signal vector field amplitudes can be written

$$\vec{s}_{lo}(\vec{r}) = \bar{s}_{lo}e^{i\phi_{lo}}\vec{u}_{\parallel}(\vec{r}) , \qquad \vec{s}_{sig} = \sqrt{\eta_m}\bar{s}_{sig}\vec{u}_{\parallel}(\vec{r}) + \sqrt{1-\eta_m}\bar{s}_{sig}\vec{u}_{\perp}(\vec{r}) , \tag{1.95}$$

where $\vec{u}_{\parallel}(\vec{r})$ represents the spatial mode profile of the LO, and $\vec{u}_{\perp}(\vec{r})$ is a spatial mode vector that describes the part of the signal field mode profile that does not interfere with the LO.

The intensity of the interference is given by the spatial scalar product of the vector fields at the output of the beam splitter (cf. Equations (1.84) and (1.85)),

$$I_+ = \vec{s}_+^{\,*}\cdot\vec{s}_+ = \varepsilon I_{sig} + (1-\varepsilon)I_{lo} + 2\sqrt{\varepsilon(1-\varepsilon)\eta_m I_{sig}I_{lo}}\cos\phi_{lo} , \tag{1.96}$$

$$I_- = \vec{s}_-^{\,*}\cdot\vec{s}_- = (1-\varepsilon)I_{sig} + \varepsilon I_{lo} - 2\sqrt{\varepsilon(1-\varepsilon)\eta_m I_{sig}I_{lo}}\cos\phi_{lo} , \tag{1.97}$$

where $I_{sig} = |\vec{s}_{sig}|^2$ and $I_{lo} = |\vec{s}_{lo}|^2$ are the intensities of the signal field and the LO, respectively. Assuming equal intensities in the signal and LO fields, and a 50:50 beam splitting ratio, we obtain a measure of the quality of the interference at each beam

splitter outputs, called the *visibility*.

$$\mathcal{V} = \frac{I_{max} - I_{min}}{I_{max} + I_{min}} = \sqrt{\eta_m} \ , \tag{1.98}$$

with $I_{max} = \max_{\phi_{lo}} I_{\pm}$, and $I_{min} = \min_{\phi_{lo}} I_{\pm}$.

Prior to every homodyne detection measurement, a direct evaluation of the visibility can be easily performed by setting equal powers in the LO and signal fields, and measuring the minimum and maximum intensities of the interference fringe while scanning the phase of the LO. A low visibility indicates a poor alignment of the optical setup or a poor adjustment of the field polarizations, that should then be corrected.

Chapter 2

Cavity optomechanics with microtoroid resonators

During this thesis work, an essential part of our experimental setup has been a tiny, mushroom-looking, silica structure (cf. Figure 2.1) with excellent optical and mechanical properties, the so-called microtoroid resonator. Combining the behavior of both a high-quality optical cavity and a high-quality mechanical resonator, it is a particularly suitable candidate for experiments in cavity optomechanics.

Due to recent progress in nano- and microfabrication, a wide variety of cavity optomechanical system have been investigated [28]. The range of system parameters that they offer covers several order of magnitudes, e.g. cavity resonance frequency from microwave to optical frequency, mechanical resonance frequencies from kilohertz to gigahertz, and resonator mass from femtogram to gram scales. Some of the most studied optomechanical systems are optical cavities with cantilevers [29], suspended micromirrors [30, 31], and membranes [32–35], optomechanical crystals [36, 37], whispering-gallery mode microresonators [38, 39], and microwave nanomechanical cavities [40–42].

In the first part of this chapter we review the characteristics and properties of a general optical cavity, before focusing on the specificities of our microtoroid cavities. We describe the operation of a microtoroid cavity within our experimental setup, and provide a characterization of its parameters. In the second part we turn our attention to the mechanical properties of the microtoroid resonator. We introduce the theoretical framework necessary to represent and understand the mechanical motion from a classical to a quantum picture. Finally we combine both the optical and the mechanical degrees of freedom of our microtoroid resonator in a general quantum theory of optomechanical interactions. This chapter thus forms the common basis from which to build up our understanding of the specific theoretical and experimental work presented in this thesis.

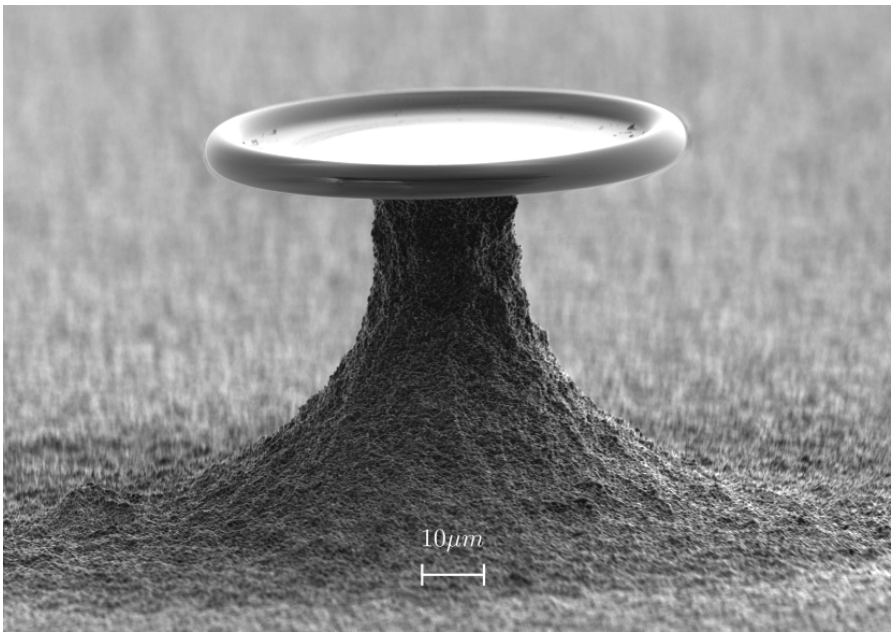

FIGURE 2.1: Scanning electron microscope (SEM) image of a microtoroid resonator.

2.1 Microtoroids as optical resonators

2.1.1 Introduction to optical cavities

The simplest representation of an optical cavity is a Fabry-Pérot resonator [43], consisting of two mirrors separated by a distance L facing each other (cf. Figure 2.2). Light entering the Fabry-Pérot optical cavity will reflect multiple times from the mirrors and produce interference patterns. In the ideal case where the two mirrors are perfectly reflecting, only a discrete set of standing wave patterns can be sustained by the cavity. This spatial modes of the optical cavity can be identified by their wavelength which is an integer fraction of the round-trip length of the light into the cavity, i.e. $\lambda_l = 2L/l$, where l is the *integer mode number*. In the frequency domain the cavity modes are evenly separated by the *free spectral range* (FSR) of the cavity, given by

$$\Delta\nu_{FSR} = \frac{c}{2n_g L} \ , \tag{2.1}$$

where n_g is the group index of the constituent media within the optical cavity.

In practice, light may escape the Fabry-Pérot optical cavity through one of the mirrors, or be absorbed or scattered, which is described by a total energy decay rate κ, thereby spreading the discrete set of cavity mode frequencies into continuous resonance spectra. The spreading of the resonance spectra may lead to an overlap of optical modes in frequency what is indicated by the *finesse* of the cavity, $\mathcal{F} = 2\pi \times \Delta\nu_{FSR}/\kappa$, which gives the average number of round-trips that a photon can complete before escaping

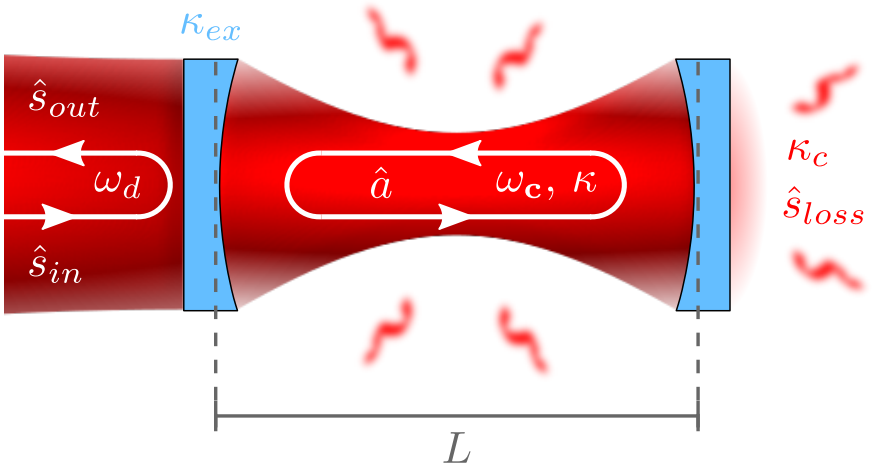

FIGURE 2.2: Single-sided Fabry-Perot optical cavity with length L. An input field $\hat{s}_i n$ at frequency ω_d is coupled to an optical cavity mode field $\hat{a}$ at an energy coupling rate κ_{ex}. The cavity mode field suffers optical loss described by the coupling to a loss channel field $\hat{s}_{loss}$ at a rate κ_c. The optical cavity has a resonance frequency ω_c and a width $\kappa = \kappa_{ex} + \kappa_c$.

the cavity. High-finesse cavities are commonly used to enhance the interaction between optical fields and other physical systems such as atoms and ions in cavity quantum electrodynamics, or mechanical oscillators in cavity optomechanics. Another quantity of interest is the ratio of energy stored in the optical cavity mode over the energy loss, coined the *quality factor* (or Q factor), and given by $Q = \omega_c/\kappa$, where ω_c is the angular frequency of the optical resonance. High-Q cavities are best suited for preserving the coherence of optical states over extended periods of time and gather interests for the development of optical quantum memories.

2.1.2 Input-output formalism

The practical observation of the evolution of an optical cavity mode field can only be achieved by monitoring the energy leaking out of the cavity. The input-output theory describes the time-evolution of the field amplitude of a cavity mode, $\hat{a}$, coupled to one or many external systems constituting its environment. One may distinguish different loss ports through which energy escapes the optical cavity mode, e.g. the light escaping via one of the two mirrors, the light absorbed within the cavity, or the light scattered into other optical modes. Here we will restrain ourselves to a cavity sustaining a single optical mode coupled to one input-output channel at an energy exchange rate κ_{ex}, and one loss channel at a rate κ_c, such as the single-sided Fabry-Pérot cavity depicted in Figure 2.2. In a frame rotating at the input (or drive) field frequency, ω_d, Heisenberg

equation of motion describing the time-evolution of the cavity field amplitude reads [22],

$$\dot{\hat{a}} = \left(i\Delta - \frac{\kappa}{2}\right)\hat{a} + \sqrt{\kappa_{ex}}\hat{s}_{in} + \sqrt{\kappa_c}\hat{s}_{loss}, \tag{2.2}$$

where $\Delta = \omega_d - \omega_c$ is the detuning of the input field with respect to the cavity resonance. $\hat{s}_{in}$ and $\hat{s}_{loss}$ are the field amplitudes of the input and loss channels, respectively. The input and cavity field amplitudes are normalized such that $P_{in} = \hbar\omega_d\langle\hat{s}_{in}^{\dagger}\hat{s}_{in}\rangle$ is the input power launched to the cavity, and $n_c = \langle\hat{a}^{\dagger}\hat{a}\rangle$ is the mean number of photons in the cavity mode.

The output field $\hat{s}_{out}$ is a linear combination of the input field and the cavity field leaking through the output port, which can be derived from energy conservation [43]

$$\hat{s}_{out} = \hat{s}_{in} - \sqrt{\kappa_{ex}}\hat{a} \tag{2.3}$$

The output field follows the same normalization as the input field, where $P_{out} = \hbar\omega_d\langle\hat{s}_{out}^{\dagger}\hat{s}_{out}\rangle$ is the output power from the cavity.

A follow up question is now, how to consider more input and output fields. Input fields must enter as additional driving sources in Equation (2.2) with their respective coupling rates, and each output field would obey a linear relation with the input and cavity fields similar to Equation (2.3). Such a representation is required for a double-sided Fabry-Pérot cavity or for a microtoroid with coupled counter-rotating optical modes. One must keep in mind that the total energy decay rate κ is always the sum of all energy decay rates, e.g. $\kappa = \kappa_{ex} + \kappa_c$ in the case of a single-sided Fabry-Pérot cavity.

2.1.3 Classical field dynamics

The classical amplitudes of the fields are given by the mean of the optical field amplitudes, e.g. $a = \langle\hat{a}\rangle$, so we may rewrite Equations (2.2) and (2.3) in terms of the classical field amplitudes,

$$\dot{a} = \left(i\Delta - \frac{\kappa}{2}\right)a + \sqrt{\kappa_{ex}}s_{in}, \qquad s_{out} = s_{in} - \sqrt{\kappa_{ex}}a. \tag{2.4}$$

Here we have chosen the loss channel field to be in a vacuum state, such that $\langle\hat{s}_{loss}\rangle = 0$. This is a reasonable assumption given that at optical frequencies the photon occupation of the environment at room temperature is (very close to) zero.

For a monochromatic drive field with constant amplitude $\bar{s}_{in}$, the steady-state amplitudes of the cavity and output fields are calculated to be,

$$\bar{a} = \frac{\sqrt{\kappa_{ex}}}{\kappa/2 - i\Delta}\bar{s}_{in} \ , \tag{2.5}$$

$$\bar{s}_{out} = \left(1 - \frac{\kappa_{ex}}{\kappa/2 - i\Delta}\right)\bar{s}_{in} \ . \tag{2.6}$$

We may chose the phase of the cavity field, $\phi_c = \arg(\bar{a})$, to be the zero reference in the frame rotating at the drive field frequency, such that $\bar{a} = |\bar{a}| = \sqrt{n_c}$, therefore the phases of the input and output fields are given by $\phi_{in} = -\arctan[2\Delta/\kappa]$, and $\phi_{out} = -\arctan[2\Delta/(\kappa_c - \kappa_{ex})]$. The cavity imposes a phase shift on fields that are detuned from the cavity resonance, while fields on resonance with the cavity remain in phase with the cavity mode field.

The field amplitudes are not easily accessible experimentally as photodetectors measure the energy of an electromagnetic field. Therefore it is interesting to calculate the power of the field circulating in the cavity and the power of the field at the output of the cavity, yielding

$$P_c = \frac{\hbar\omega_d\bar{a}^2}{\tau_{rt}} = \frac{\mathcal{F}}{\pi}\frac{2\eta}{1+\bar{\Delta}^2}P_{in} \ , \tag{2.7}$$

$$P_{out} = \hbar\omega_d|\bar{s}_{out}|^2 = \left(1 - \frac{4\eta(1-\eta)}{1+\bar{\Delta}^2}\right)P_{in} \ , \tag{2.8}$$

where $\tau_{rt} = \Delta\nu_{FSR}^{-1}$ is the round-trip time of a photon inside the cavity. The optical coupling parameter, $\eta = \kappa_{ex}/\kappa$, indicates the proportion of the energy escaping the cavity that leaks into the output channel. The frequency spectrum of the circulating power and output power have Lorentzian profiles with full width at half-maximum (FWHM) equal to the overall energy decay rate κ. The normalized detuning, $\bar{\Delta} = 2\Delta/\kappa$, then indicates how strongly detuned the driving field is with respect to the spectral width of the cavity resonance.

Several points merit to be emphasized so far. First of all Equation (2.7) shows that the circulating power of the cavity field is strongly enhanced over the input power in high-finesse cavities, with a maximum power enhancement achieved by driving the cavity on resonance. On one hand the build-up of optical power in the cavity is beneficial for applications requiring high pump power in nonlinear media such as lasers [44], and optical parametric oscillators (OPO) [13]. On the other hand, high circulating power may lead to undesired thermal effects due to the absorption of light into the cavity medium [11], or unwanted nonlinear effects due to the Kerr nonlinearity [45].

A second interesting point is that the power spectrum of the output field is symmetric with respect to the detuning of the drive field from the cavity resonance, whereas the

phase shift induced by the cavity is not. The asymmetry in the phase response of the cavity with respect to the frequency detuning may be used in elaborate phase locking schemes (e.g. Pound-Drever-Hall (PDH) frequency stabilization [46, 47]) to preserve the detuning of the drive field from the cavity resonance despite frequency drifts of the drive field or the cavity resonance.

2.1.4 Cavity coupling regimes

From Equations (2.5) and (2.6), we observe that the amplitude and phase response of a cavity to an input field is completely determined by the normalized quantity η and Δ. We may distinguish three regimes depending on the values of the optical coupling parameter η:

- $\eta < 1/2$: When the energy exchange rate at the input-output port of the cavity is lower than the energy decay rate to the loss channel, the cavity is *undercoupled*. The amplitude of the field leaving the cavity from the output port is then smaller than the amplitude of the input field, and most of the energy of the cavity is lost to the environment.

- $\eta = 1/2$: When the energy injected into the cavity match the energy lost to the environment, the cavity is *critically coupled*. The amplitude of the field leaving the cavity from the output port is equal to the amplitude of the input field giving rise to complete destructive interference on resonance. This situation is also referred to in more general terms as impedance matching.

- $\eta > 1/2$: When the energy exchange rate at the input-output port of the cavity is larger than the energy decay rate to the loss channel, the cavity is *overcoupled*. The amplitude of the field leaving the cavity from the output port is larger than the amplitude of the input field, and most of the energy of the cavity is coupled to the output field.

In the case of a single-sided Fabry-Pérot cavity, where the energy can exit the cavity only through one of the two mirrors (neglecting scattering and absorption loss), the three coupling regimes are accessed by tuning the transmittivity of the mirrors. Undercoupling corresponds to the transmittivity of the input-output mirror being lower than the one of the back mirror. Critical coupling corresponds to equal transmittivity of the two mirrors. Overcoupling corresponds to the transmittivity of the input-output mirror being higher than the one of the back mirror.

Figure 2.3 shows the amplitude and phase of the cavity and output fields as a function of normalized detuning, and for three values of the optical coupling parameter, $\eta = 0.1$, 0.5, and 0.8, showing the three coupling regimes. The phases of the cavity

and output fields are plotted relative to the phase of the input field. Assuming that the energy decay rate to the loss channel is kept constant, only the coupling rate to the output is varied. Recalling that the finesse of the cavity is inversely proportional to the total energy decay rate, we may recast Equation (2.7) into

$$\frac{P_c}{P_{in}} = \frac{4\eta(1-\eta)}{(1+\bar{\Delta}^2)} \frac{Q_c}{l\pi}, \tag{2.9}$$

where $Q_c = \omega_c/\kappa_c$ is the *intrinsic quality factor* of the cavity resonance and l is the integer mode number. It is clear that the maximum circulating power enhancement in the cavity is reached at critical coupling, on resonance. It results in all the power of the input field being absorbed and dissipated within the cavity, resulting in a zero output power. The critical coupling regime is of interest for applications that require strong pump powers, however the absence of measurable output on resonance complicates its experimental implementation. In the undercoupled regime the properties (phase, field fluctuations) of the output field are inherited in majority from the input field, whereas in the overcoupled regime the properties of the output field derive essentially from the properties of the cavity field. The overcoupled regime provides the highest interaction between the input field and the cavity as most of the input field is coupled into the cavity and most of the cavity field is coupled to the output field. It results in a very pronounced phase response to small deviations of the input field frequency from the resonance. We will see in Chapter 3 that this resonance effect allows for an efficient transduction of mechanical displacements onto the optical phase of the output field in cavity optomechanical systems. We must also point out that increasing the input-output coupling rate while keeping the loss rate fixed widens the frequency bandwidth of the resonance, what is not visible on Figure 2.3 due to the scaling of the abscissae.

2.1.5 Whispering-gallery modes

The electromagnetic modes of a microtoroid or a microsphere resonator are called *whispering-gallery modes* (WGM) in analogy to the propagation of acoustic waves along the wall of St Paul's Cathedral, first described by Lord Rayleigh at the end of the nineteenth century. The longitudinal and transverse profiles of WGM in microspheres can be fully derived analytically from the wave equation by separation of variables [48]. For toroidal cavities, however, exact analytical solutions to the wave equation are not derivable as the wave equation in toroidal coordinates is not separable. Approximate solutions have been obtained [49–53] and show that optical WGM of toroids are not pure transverse electric (TE) or transverse magnetic (TM) modes, i.e. neither the electric nor the magnetic fields are perpendicular to the direction of propagation. Nevertheless microtoroid cavities exhibit TE-like and TM-like modes whose transverse profiles and

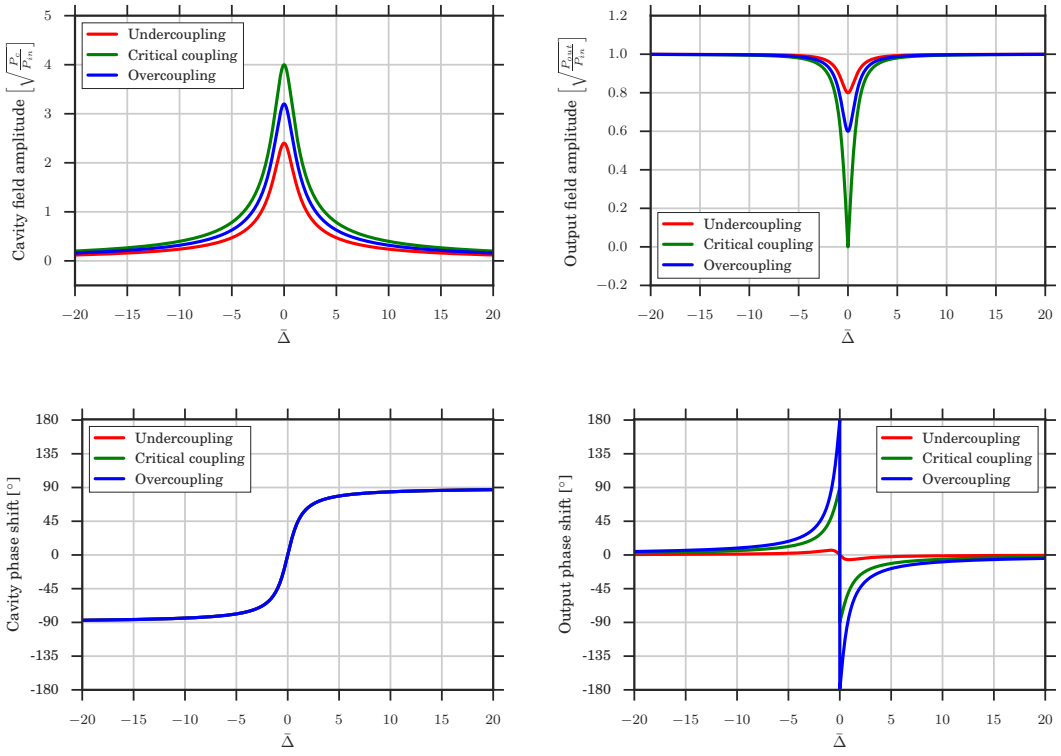

FIGURE 2.3: Illustration of the field amplitude (Top) and phase (Bottom) of the cavity (Left) and output (Right) as a function of the normalized detuning, $\bar{\Delta} = 2\Delta/\kappa$, for the three coupling regimes, undercoupling (Red), critical coupling (Green) and overcoupling (Blue) represented by the values of the coupling parameter, $\eta = 0.1$, 0.5 and 0.8, respectively. The maximum amplitude of the cavity field is achieved on resonance at critical coupling and is given by the square root of the intrinsic Q-factor of the resonance, here $Q_c/l\pi = 16$.

resonance frequencies can be obtained via the approximation of a toroid to an oblate spheroid under the conditions of large cavity optical path length to mode wavelength ratio and large major to minor diameters ratio [52], or via finite element method (FEM) simulations [54].

Figure 2.4 shows the transverse mode profiles of the first two quasi-TE and quasi-TM WGMs, and two higher order WGMs of a fused-silica toroid cavity with major radius $R_{tor} = 29$ μm, and minor radius $r_{tor} = 2.5$ μm. The transverse mode profiles are calculated via FEM simulations following the method in [54]. The black arrows indicate the orientation of the electric field and the color gradient shows the intensity of the cavity mode field. The dimension of the toroids are chosen to resemble the typical dimensions of our microtoroid resonators.

At a frequency around 282 THz corresponding to a free-space wavelength around 1064 nm, and for a microtoroid with the dimensions given above, the FSR of the fundamental quasi-TE_{00} and quasi-TM_{00} modes is calculated via FEM simulations, $\Delta\nu_{FSR} \approx 1.060$ THz, and corresponds to a shift in the WGM free-space wavelength,

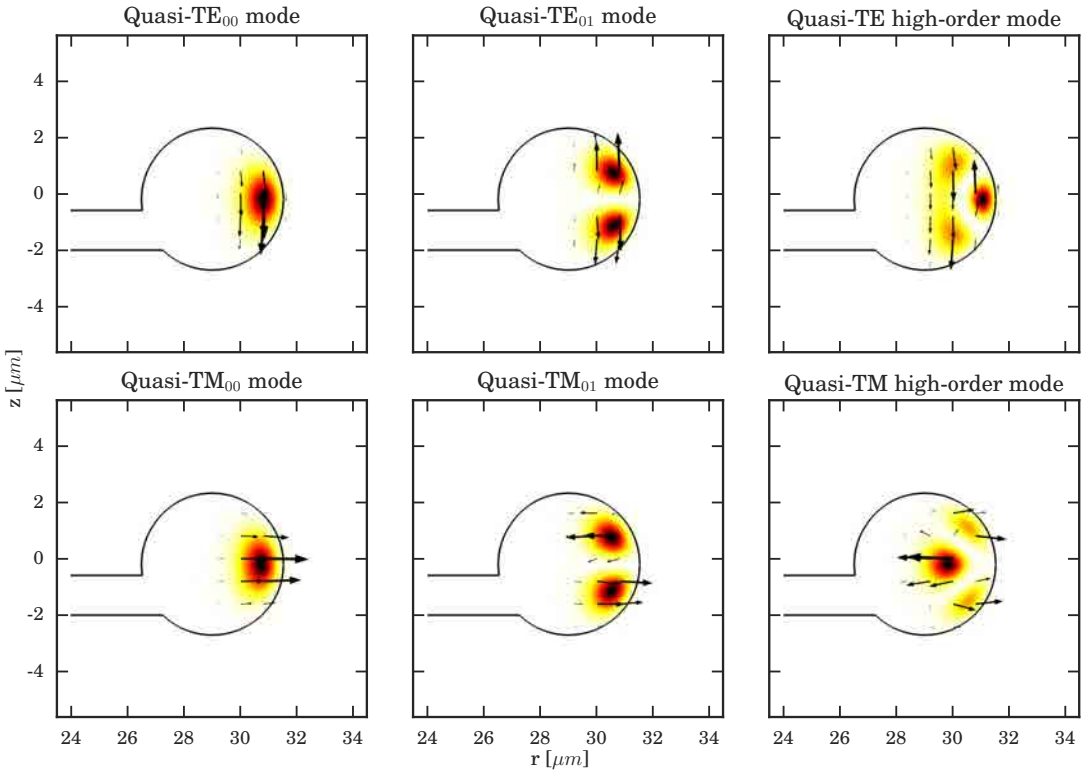

FIGURE 2.4: Transverse mode profile of optical whispering-gallery modes in a microtoroid resonator obtained via FEM simulations [54]. The black arrows indicate the orientation of the electric field and the color gradient shows the intensity of the cavity mode field. The toroid cavity has major radius $R_{tor} = 29$ µm, and minor radius $r_{tor} = 2.5$ µm, and is made of fused-silica, $n_{SiO_2} = 1.4496$ [55]. The dimensions of the microtoroid cavity reflect typical geometries of the microtoroids we operate in our laboratory.

$\Delta\lambda_{FSR} \approx 4.0$ nm. A similar result can be obtained analytically by calling Equation (2.1) with the refractive index $n_g \approx 1.4496$ [55] and the mode radius $R \approx 31$ µm. This corresponds to the WGM being localized near the outer edge of the toroid cavity ($R_{tor} < R < R_{tor} + r_{tor}$), what matches with the optical modes shown on the left panels of Figure 2.4.

2.1.6 Evanescent near-field coupling

There exist several ways of coupling light in and out of a WGM cavity, e.g. prism couplers [10], side-polished fiber couplers [56–58], and fiber tapers [59]. All rely on the evanescent near-field coupling between the modes of the input-output coupler and the WGM resonator [60]. When light undergoes total internal reflection at the boundary from a high (e.g. silica) to a low (e.g. air) refractive index material, a part of the optical field penetrates into the low index medium and remains confined as an evanescent wave along the boundary. If a third medium with high refractive index is positioned within a few wavelengths from the interface between the two initial mediums, the evanescent field

from the first medium will "feel" the third medium and electromagnetic energy will be transferred from the optical mode of the first medium to the optical mode of the third medium, and vice versa. This process is also called *frustrated total internal reflection.*

Prism couplers have been used to couple free-space laser beams to WGM [10]. It is a versatile and efficient method as the phase and mode matching between the coupler and the WGM resonator mode can be easily controlled by tuning the input beam parameters. However, it requires a rather bulky setup that is hardly suitable for probing micron scale cavities such as our microtoroids. Side-polished fiber couplers are made by partial removal of the cladding in a bent section of the fiber, thereby giving access to the evanescent field of the fiber guided mode. This type of fiber coupler has the practical advantage of single-mode fiber operation but achieves comparatively poor phase matching and low coupling [56–58].

Tapered fiber coupling enables high-efficiency coupling of more than 99% [61] from a single-mode fiber to a single WGM, and is suitable for probing micron scale cavities due to the small dimensions and handiness of optical fibers. Tapered fibers are fabricated by locally heating and stretching a section of a single-mode optical fiber in order to form a region with reduced diameter which remains connected to the unaltered part of the fiber by a gradual taper transition. In the waist region the optical mode is no longer guided by the waveguide formed by the core and cladding of the fiber as the former becomes negligibly small, but is guided by the waveguide formed by the cladding and the air. Therefore, the mode guided through the waist region becomes evanescent, and the evanescent field becomes more delocalized out of the fiber as the waist diameter is reduced to a size on the order of the mode wavelength. Energy can be transferred between the guided mode of the tapered fiber and the WGM of the optical cavity by overlapping their evanescent fields, which translates into bringing the microtoroid and waist region of the tapered fiber close to each other.

Coupled mode theory gives the coupling strength between the fiber mode and the WGM as an overlap integral of their electric fields [62–64]. Analytical approximate representations of the electric fields can be derived for the microtoroid cavity mode [49–53] and for the tapered fiber mode [62, 65]. However calculating the three-dimensional overlap integral is not trivial and holds little interest in our discussion so we will only provide a qualitative understanding of the dependency of the coupling strength over relevant system parameters.

First of all, the integral of the overlapping fields along the direction of propagation of the optical modes provide a phase-matching condition in the form $\sqrt{\kappa_{ex}} \propto 1-\cos(\beta_c-\beta_f)$ [59, 64], where $\beta_c \approx n_{tor}\omega_c/c$ is the phase constant of the WGM and $\beta_d = (n_{fib}\omega_d/c) \times \sqrt{1-\delta^2}$ is the phase constant of the fiber mode (input mode). Here n_{tor} and n_{fib} denote the refractive indexes of the microtoroid cavity and the tapered fiber, respectively. δ

is a term proportional to the ratio of the mode wavelength to the mode field diameter of the tapered fiber and becomes significant for fiber radii on the order of the mode wavelength [65]. Phase-matching depends essentially on the radius of the of the tapered fiber, and on the refractive indexes of the fiber and microtoroid. In order to be able to reach a perfect phase-matching the refractive index of the taper must be higher than the refractive index of the microtoroid, then the radius of the taper waist must be adjusted to match the phase constants. In a coupling experiment the refractive indexes are fixed by the choice of fiber and microtoroid but the radius of the tapered fiber at the coupling region can be tuned by moving the fiber along the taper gradient.

Once the condition for phase-matching are reached, the optical coupling strength can be enhanced by increasing the overlap between the mode fields of the tapered fiber and the WGM cavity. As the evanescent field amplitudes decay exponentially out of the guiding mediums with high refractive indexes, the overlap integral gives an exponential dependence of the coupling strength with the separation d between the tapered fiber and the WGM resonator, which can be approximated by $\sqrt{\kappa_{ex}} \propto \exp(\alpha_c d)$, where the decay length of the evanescent field out of the WGM cavity is given by $\alpha_c^{-1} = (c/\omega_c)/\sqrt{n_{tor}^2 - 1}$.

Last but not least the polarizations of the mode fields of the toroid and tapered fiber must match in order to achieve maximum coupling. Indeed it is clear from Figure 2.4 that the eigenmodes of a microtoroid cavity have a definite linear polarization and therefore cannot accept orthogonal polarizations of the input field. On the other hand it might be desirable to place part of the input field into an orthogonal polarization to the WGM polarization as it will pass through the fiber without feeling the presence of the cavity and may thus serve as a phase reference to the field that is coupled in and out of the optical cavity, such as in a Hänsch-Couillaud polarization spectroscopy scheme [66].

2.1.7 Optical spectroscopy of whispering-gallery modes

The characteristics of an optical cavity are obtained by measuring its frequency spectrum. The resonance spectrum of a cavity is obtained by recording the power of the cavity output field while scanning the frequency of the input field coupled into the cavity. Figure 2.5 shows the experimental setup we operate to characterize optical resonances of our microtoroid cavities. We use a free-space diode laser[1] in a Littman-Metcalf configuration [67] which allows for wide mode-hop-free operation at wavelengths between 1050 nm and 1068 nm. The laser provides a coarse and a fine tuning of its frequency by controlling the orientation of a pivoting tuning mirror with a DC motor or a piezoelectric transducer, respectively. The power of the input beam probing the cavity resonances is controlled by the combination of a half-wave plate (HWP) and a polarizing beam

[1] New Focus Velocity^{TM}TLB6721 Widely Tunable Laser. Mode-hop free operation from 1050 nm to 1068 nm.

splitter (PBS). The collimated free-space laser beam is focused by an aspheric lens[2] into a single-mode optical fiber[3]. An identical aspheric lens is used at the output of the fiber. A single mode fused fiber optic coupler (FFOC) splits the optical power towards a fiber-loop cavity (FLC) in one path and the microtoroid resonator in the other path. The resonance spectrum of the FLC is recorded by a photodetector[4] and serves as a reference to calibrate the resonance spectrum of the microtoroid cavity. The fiber optical field is coupled to the microtoroid cavity via a tapered fiber. The silica microtoroid can be selected among twenty microtoroids sitting on a silicon chip. The position of the tapered fiber in the setup is fixed but the chip sits on a 3-axis stage[5] with manual and piezoelectric actuators, that provides a precise control over the position of the microtoroid resonator relative to the fiber, thus a control over the optical mode coupling. Additionally the chip is mounted on a Peltier element[6] driven by a feedback PID temperature controller[7] which allows the tuning and stabilization of the temperature of the microtoroid WGM. The polarization of the optical fields at the input of the FLC and microtoroid cavity is tuned by fiber polarization controllers[8] (FPC) in order to optimize the optical coupling to the cavity modes.

In order to identify the high-Q resonances of our microtoroid cavities we must first tune the laser frequency continuously over a range larger than one FSR ($\Delta\nu_{scan} > 1$ THz, or equivalently $\Delta\lambda_{scan} > 4$ nm) by using the coarse tuning capability of the laser. The coarse tuning can operate at a maximum speed of 12 nm.s^{-1} which limits the scanning rate over one FSR to about 1.5 Hz, therefore we operate our oscilloscope in roll-mode to get a faster display of the resonance spectrum of the cavity. The optical coupling to the WGMs is tuned by adjusting the position of the microtoroid relative to the tapered fiber, and by adjusting the polarization of the input field. While sweeping the frequency of the laser, high-Q resonances are identified by sharp dips in the measured output power, as illustrated on the top right panel of Figure 2.3. Once a suitable resonance is found the scanning frequency range is reduced to a few hundreds of megahertz in order to increase the resolution of the measured resonance spectrum. The laser frequency is henceforth modulated by applying a triangular wave signal from a signal generator to the piezoelectric transducer of the tuning mirror. A maximum frequency range of about 30 GHz around the cavity resonance can be scanned at rates up to 200 Hz.

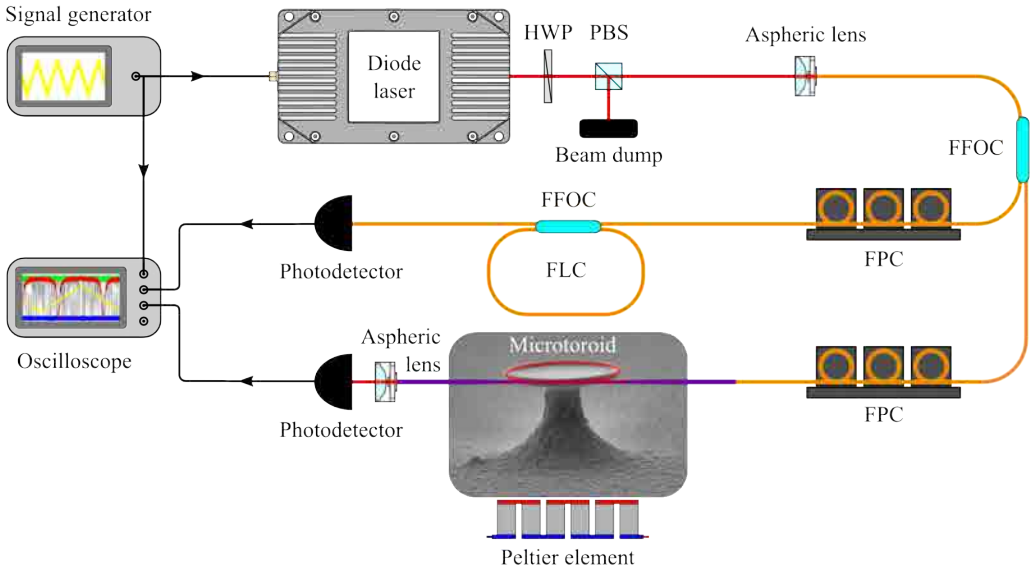

FIGURE 2.5: Experimental setup for optical spectroscopy of microtoroid WGMs. An optical beam from a widely tunable diode laser is coupled into a fiber to probe the resonances of a fiber-loop cavity (FLC) and of a microtoroid cavity. The resonance spectra are recorded by sweeping the frequency of the laser and measuring the optical power at the output of the FLC and microtoroid cavities. The FLC serves as a reference for the frequency calibration of the WGMs spectra. The polarization of the input fields coupled into the optical cavities is tuned by fiber polarization controllers (FPC) in order to optimize the coupling strength. The resonance properties of the microtoroid cavity are tuned by varying the thermal expansion of the microtoroid with a Peltier element. HWP - Half-wave plate, PBS - Polarizing beam splitter, FFOC - Fused fiber optic coupler.

Frequency calibration of the cavity spectrum

The measurement result we obtain by sweeping the laser frequency across the resonances of the microtoroid cavity shows the transmission through the tapered fiber as a function of scanning time. It is not straightforward to relate the scanning time to the laser frequency as the precise conversion from the voltage applied to the piezoelectric transducer of the tuning mirror to the laser frequency is not provided by the manufacturer of the diode laser. A well-known technique for calibrating the frequency response of a cavity resonance uses optical sidebands as frequency references. The phase of the input field is modulated at a known frequency ω_{mod} larger than the width of the cavity resonance such that two optical sidebands are generated at frequencies $\omega_d \pm \omega_{mod}$. As the laser frequency is swept over the cavity resonance the sidebands couple to the cavity what

[2]Thorlabs C240TME-1064, f = 8.07 mm, NA = 0.5.
[3]Thorlabs SM980-5.8-125.
[4]Thorlabs PDA10CF-EC
[5]Thorlabs MAX311D/M
[6]Thorlabs TEC1.4-6
[7]Wavelength Electronics LFI-3751
[8]Thorlabs FPC030 and FPC020

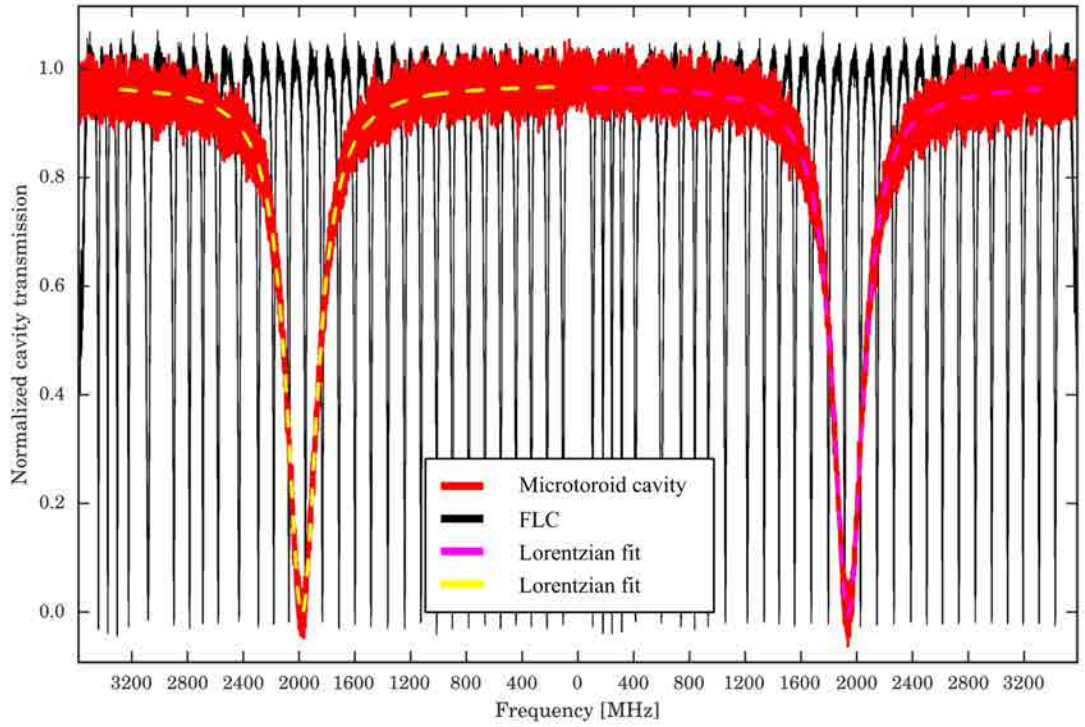

FIGURE 2.6: Frequency scan of a cavity resonance on critical coupling. The frequency scan is calibrated via the FSR, $\Delta\nu_{FSR}^{(FLC)} = 119$ MHz, of FLC resonances (black). A Lorentzian fit (yellow and magenta) to the cavity resonance (red) gives a resonance width $\kappa/2\pi = 265$ MHz.

generates two additional dips in the output power scan which are each separated from the main cavity resonance by ω_{mod}.

The sharpest resonances we measure from our microtoroid cavities are typically in the order of 300 MHz wide which means that the use of optical sidebands for calibration requires a phase modulator and a signal generator with high bandwidths. We use instead a FLC with a known FSR to calibrate the frequency scan of the microtoroid cavity. The FLC is simply made by joining an output port of a FFOC[9] to one input port. The FSR of our FLC was first measured by two different means which gave similar results. With a fiber coupled phase modulator[10] we generated optical sidebands at a few megahertz to measure the FWHM of the FLC, $\kappa_{FLC}/2\pi = 1.30$ MHz, then the FSR, $\Delta\nu_{FSR}^{(FLC)} = 119$ MHz. Alternatively we measured the length of the fiber loop cavity, $L_{FLC} = 171$ cm and estimated the refractive index of the fiber[11] from the manufacturer's spec sheet, $n = 1.472$, to calculate the FSR using Equation (2.1). We found very good agreement between the values obtained from the two methods.

[9] Thorlabs FC1064-99B-APC
[10] Photline NIR-MPX-LN-0.1
[11] Corning® HI 1060 FLEX

Figure 2.6 shows a frequency scan of one resonance of a microtoroid cavity. The scan is calibrated by using the resonances of a FLC (black trace), and gives a resonance width of the WGM at critical coupling, $\kappa/2\pi = 265$ MHz. Optical resonances are measured close to room temperature, here 28.23°C, and at atmospheric pressure. The sharpest resonances we measured on various microtoroids have intrinsic optical Q factors around, $Q_c \approx 2 \times 10^6$, and an estimated finesse, $\mathcal{F} \approx 4000$.

2.1.8 Effect of the taper-toroid separation on resonances

We have already noted that reducing the gap between the fiber and the toroid leads to an increase in the coupling rate which itself translates into a widening of the cavity resonance spectrum. However not only the bandwidth but also the frequency of the resonance is affected by a change in the taper-toroid separation. Indeed as the fiber is brought closer to the microtoroid, the effective refractive index surrounding the WGM cavity increases. Therefore the shape of the WGM is pulled toward the tapered fiber and the optical path length of the WGM becomes longer. As a result the wavelength of the WGM increases, or equivalently its resonance frequency decreases.

The resonance frequency shift can be analytically derived by including the (small) variation of the refractive index induced by the fiber into the wave equation of the WGM, and solving to first order using perturbation theory [38]. It results that the amplitude of the resonance frequency shift increases exponentially with the reduction of the separation between the tapered fiber and the microtoroid, $\Delta\omega_c(d) \propto -\exp(-2\alpha_c d)$, with d the taper-toroid separation. It must be noted that the dependency of the frequency shift and the dependency of the optical coupling rate on the taper-toroid separation are approximately the same.

Figure 2.7(a) shows six frequency scans of a resonance of a microtoroid cavity at various separations of the tapered fiber and microtoroid. As the separation is reduced the central frequency of the resonance is shifted towards lower values and the width of the resonance increases. Each resonance spectrum was fitted with a Lorentzian function according to Equation (2.8) and the resonance frequency and bandwidth were retrieved from the fit, as wells as the normalized power transmission on resonance. The intrinsic energy decay rate of the cavity was obtained from the bandwidth of a cavity resonance in the undercoupled limit, $\kappa_c \approx \kappa = 2\pi \times 142MHz$. The taper-toroid coupling rate was calculated by subtracting the intrinsic energy decay rate from the fitted Lorentzians FWHM, and is plotted on Figure 2.7(b) alongside the resonance frequency shift and the normalized power transmission on resonance as a function of the separation between the tapered fiber and the microtoroid cavity. We fitted two exponential functions to the measured resonance frequency shifts and coupling rates which gave us two values for the decay length of the evanescent field, $(\alpha_c^{(1)})^{-1} = 0.43$ μm and $(\alpha_c^{(2)})^{-1} = 0.26$

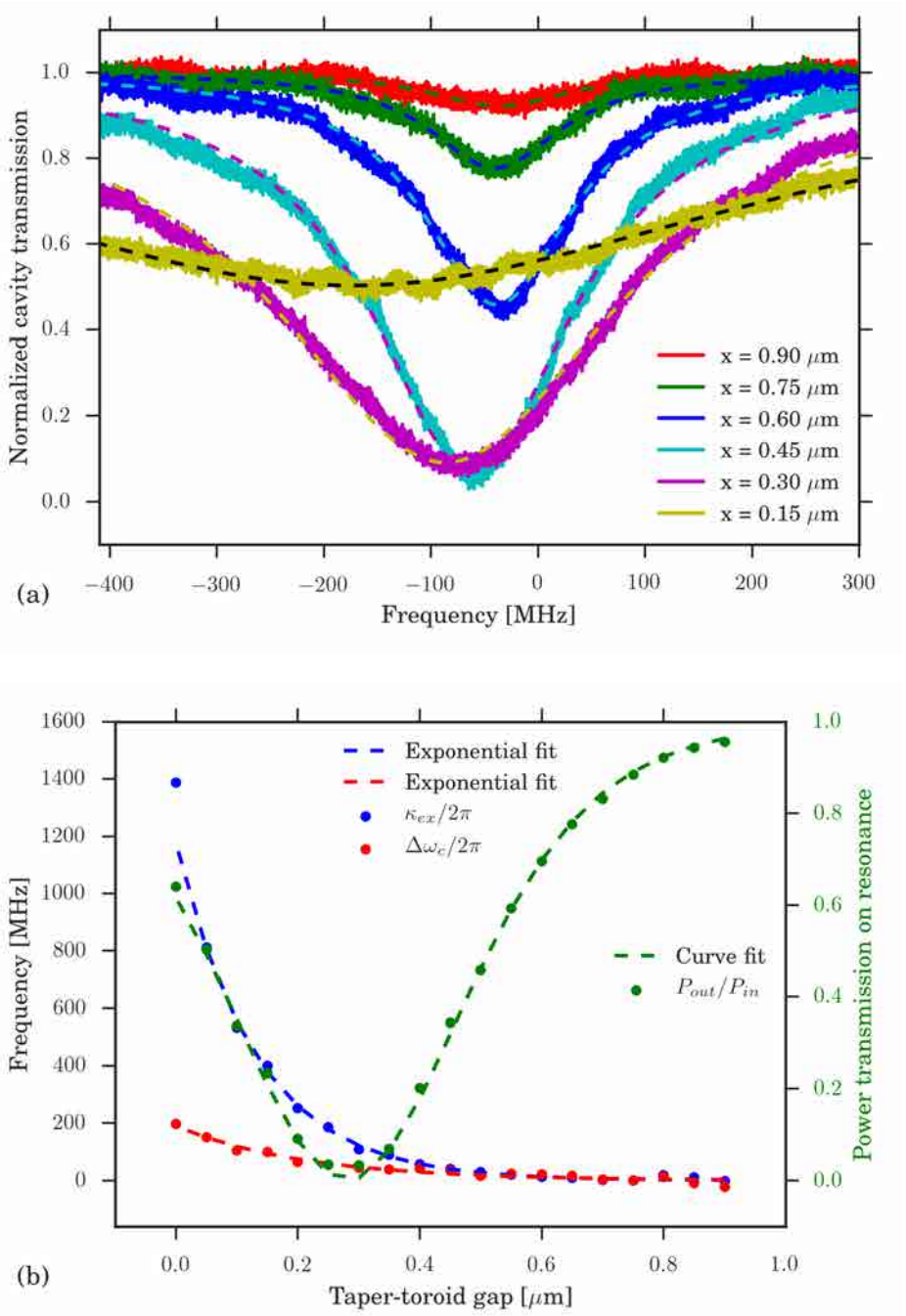

FIGURE 2.7: (a) Frequency scans of a microtoroid resonance at various taper-toroid separations with lower values of x corresponding to smaller gaps. The dashed curves are Lorentzian fits to the toroid resonance. As the taper-toroid gap is reduced the resonance frequency decreases and the resonance width increases, moving from an undercoupled cavity resonance ($x \geqslant 0.45$ μm) to an overcoupled cavity resonance ($x \leqslant 0.30$ μm). (b) Taper-toroid coupling rates (blue dots), resonance frequency shifts (red dots) and output powers on resonance (green dots) at various taper-toroid separations. Exponential fits to the taper-toroid coupling rates (blue dashed curve) and resonance frequency shifts (red dashed curve) gives a decay length of the evanescent field of the WGM, $(\alpha_c^{(1)})^{-1} = 0.43$ μm and $(\alpha_c^{(2)})^{-1} = 0.26$ μm, respectively. The output power on resonance as a function of the taper-toroid gap is calculated via Equation (2.8) by using the parameters of the exponential fit to the optical coupling rate. The results (green dashed curve) show a good agreement with measurements (green dots).

μm, respectively. The higher value of $\alpha_c^{(2)}$ may be explained by the contribution of the evanescent field from the tapered fiber. Nevertheless both values show a discrepancy to the theoretical decay length $(\alpha_c)^{-1} = 0.16$ μm calculated for a refractive index of the fused silica microtoroid $n_{tor} = 1.4496$ [55] and a cavity mode wavelength $\lambda_c = 2\pi c/\omega_c = 1064$ nm, indicating that the evanescent fields from the toroid and the fiber are less confined than predicted by theory.

In order to check the coherence of the values obtained from the exponential fit to the measured coupling rates with the model of the coupled cavity, we used these values in Equation (2.8) to calculate the output power on resonance ($\Delta = 0$) as a function of the taper-toroid gap. The results show a good agreement with measurements as shown by the green dot and dashed curves on Figure 2.7(b).

2.1.9 Nonlinear effects in fused silica microtoroids

The power circulating in high finesse cavities is several orders of magnitude higher than the power launched into the cavity. The concentration of this optical power into the small volume of a micrometer-scale resonator enhances optical nonlinearities [10]. Our microtoroids are made of fused silica which is an amorphous isotropic material with no $\chi^{(2)}$-nonlinearities, therefore the lowest order nonlinearities that may arise are $\chi^{(3)}$-nonlinearities such as the Raman or Kerr nonlinearities. Additionally thermal nonlinearities may arise due to the absorption of optical power by the medium of the optical cavity [11, 12]. The nonlinear effects induced by variations of the temperature of the resonator usually dominate the optically-induced nonlinear effects.

Optical nonlinearities

The Raman nonlinearity concerns the inelastic scattering of optical photons onto vibrational phonons in the silica structure, commonly known as Raman scattering. The high powers circulating in the WGM of silica microcavities enhance the Raman gain leading to stimulated Raman scattering when the Raman gain exceeds the losses of a neighboring WGM. Ultra-high-Q WGM resonators have been used to achieve Raman lasing and even cascaded Raman scattering at very low threshold pump power [44, 68–71]. Compared to Q-factors of the WGM cavities used in previous achievements of stimulated Raman scattering, our microtoroid cavities achieve Q-factors two orders of magnitude below, therefore we do not exceed the threshold power for stimulated Raman scattering in our experiments.

The Kerr nonlinearity causes a modification of the refractive index of a medium dependent on the intensity of the light circulating in this medium, $n(I) = n_0 + n_2 I$ where n_2 is the second-order nonlinear refractive index with values in the order of 10^{-20}

$m^2.W^{-1}$ for typical glass materials. A change in the refractive index of a WGM cavity means an elongation of the optical path length of the cavity resulting in a red-shift of the cavity resonance frequencies. Assuming small variations of the refractive index, $n_2 I \ll n_0$, the Kerr-induced resonance frequency shift is given to first order by,

$$\Delta\omega_c(n) \approx n_2 I \frac{d\omega_c}{dn}(n_0) \approx -\omega_c(n_0)\frac{n_2 I}{n_0}. \tag{2.10}$$

With sufficiently high optical intensities, the Kerr effect may generate parametric gain and oscillations [13, 72], and also lead to an optical bistability in the steady-state of the optical cavity mode [45]. However the Kerr-nonlinearity is usually dominated by thermal nonlinearities, although is has been observed experimentally at room temperature for high power modulation frequencies [73] as the response of the Kerr-nonlinearity is faster than the thermal effects in silica.

Our typical fundamental WGM with a finesse of 4000 and a mode diameter around 2 μm achieves circulating intensities up to 4 MW/cm^2 for an input power of a 100 μW. Given a linear refractive index $n_0 = 1.45$ and a nonlinear refractive index $n_2 = 2.7\times10^{-16}$ cm^2/MW at an optical wavelength of 1064 nm [55], the expected Kerr-induced frequency shift in our microtoroids amount to $\Delta\omega_c \approx -7.4 \times 10^{-10} \cdot \omega_c \approx 0.21 MHz$ what is three orders of magnitude smaller than the sharpest widths of our cavity resonances. It results that for an input optical power on the order of or less than a hundred microwatts, the circulating optical intensities in our microtoroids are too low for producing any significant effect via Raman or Kerr nonlinearities, therefore we do not consider optical nonlinearities in our work.

Thermal nonlinearities

Variations of the temperature of the medium constituting a WGM cavity affects the resonance frequency of the WGM in two manners, by a change in the refractive index of the medium, known as the *thermo-refractive effect*, and by the thermal expansion of the cavity. The resonance frequencies of a microtoroid cavity are inversely proportional to its dimensions and refractive index, therefore the resonance frequency shift induced by a (small) temperature variation δT is to first order,

$$\Delta\omega_c(T + \delta T) \approx -\omega_c(T)\left(\alpha_T + \frac{1}{n}\frac{dn}{dT}\right)\delta T, \tag{2.11}$$

where α_T is the thermal expansion coefficient. For a fused silica microtoroid with parameters $n = 1.45$, $\alpha_T = 5.5 \times 10^{-7}$ K^{-1} and $dn/dT = 9.6 \times 10^{-6}$ K^{-1} [55], we calculate a resonance frequency shift of -2.02 GHz/K at 1064 nm. Note that the thermo-refractive effect has a bigger impact than the thermal expansion of silica. Figure 2.8(a) shows five resonance scans of a microtoroid WGM at critical coupling for various temperature of

the microtoroid. The temperature of the microtoroid is controlled by a feedback loop consisting of a Peltier element, a thermistor and a PID controller. We extract a resonance frequency shift of -1.72 GHz/K at a scan wavelength around 1064 nm (Figure 2.8(b)). The deviation from the calculated value may result from an incomplete thermalization of the silica torus in the ambient air, meaning that the temperature of the torus may differ from the temperature measured by the thermistor, or from different values of the silica material parameters which are not precisely known for microtoroids.

Besides direct tuning of the temperature of the microtoroid by controlling the temperature of the environment, the temperature of the toroid cavity may change due to absorption of light by the silica. The part of the light circulating in the high-Q WGM cavity which is absorbed by the silica, leads to an increase of the temperature by an amount δT following the heat equation,

$$\rho c_p \dot{\delta T}(\vec{r},t) = k\vec{\nabla}^2 \delta T(\vec{r},t) + \left|\bar{a}(t)\cdot\vec{e}(\vec{r})\right|^2 \kappa_{abs}, \tag{2.12}$$

where κ_{abs} is the loss rate at which optical energy is absorbed by the medium, ρ is the density of the medium, c_p its specific heat capacity, k its thermal conductivity, $\vec{e}(\vec{r})$ represents the field distribution of the WGM, and $\bar{a}(t)$ its classical field amplitude. The first term on the second hand side of the equation accounts for the heat diffusion in the medium and the second represents the heat absorbed by the medium. Due to the local and non-uniform repartition of the mode field energy within the toroid cavity, the temperature distribution in the toroid cavity for a steady-state equilibrium ($\dot{\delta T} = 0$ and $\dot{\bar{a}} = 0$) is not uniform, and the contribution of the thermo-refractive effect and thermal expansion is higher where the optical field is stronger. For simplicity however, it is reasonable to model the spatial distribution of temperature variations $\delta T(\vec{r})$ as a uniform effective temperature δT across the WGM volume, which is proportional to the absorbed power,

$$\delta T = \beta \kappa_{abs} \hbar \omega_d |\bar{a}|^2 = \beta \frac{4\eta\eta_{abs}}{1+\bar{\Delta}^2} P_{in}, \tag{2.13}$$

where $\eta_{abs} = \kappa_{abs}/\kappa$ is the absorption fraction of the cavity power loss, i.e the power lost by the cavity mode due to absorption relative to the total power lost. We measured a dependence of the resonance frequency on input power of -0.8 MHz/μW by looking at the resonance frequency shifts of a WGM at critical coupling for various input powers, as shown on Figure 2.8(c). Assuming that the red-shift of the resonance with increasing input power is due to the photothermal effect only we calculate a temperature increase with input power of $2\beta\eta_{abs} \approx 0.5$ K/mW.

The resonance frequency shift induced by a variation of the temperature may cause a thermal bistability [10–12] as the system of interdependent equations (2.5), (2.11) and

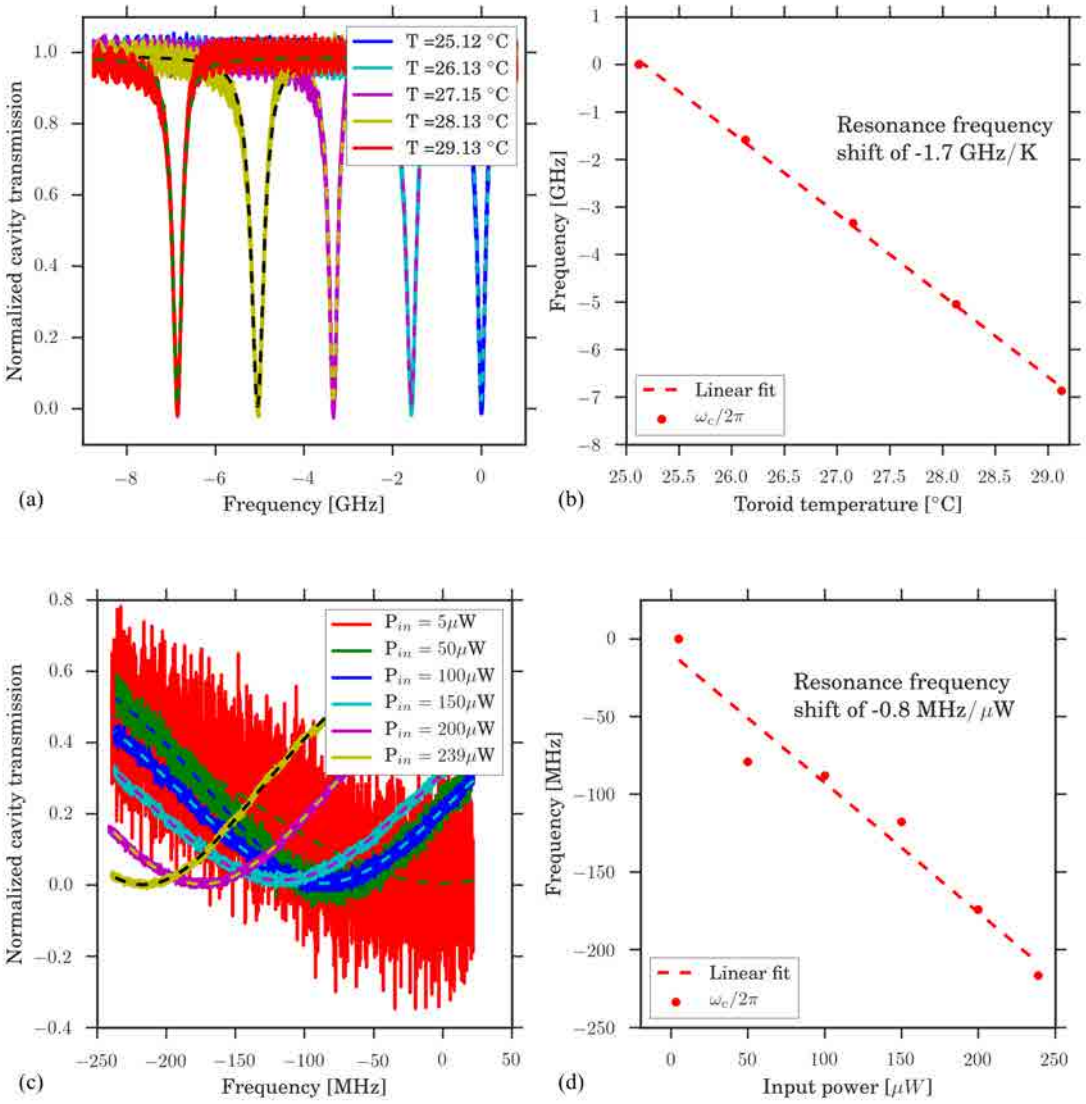

FIGURE 2.8: Frequency scans of a microtoroid resonance at critical coupling for various temperatures (a) and input power (c). The dashed curves are Lorentzian fits to the toroid resonances. As the temperature is increased by heating the microtoroid with a Peltier element (a), the resonance frequency decreases due to the thermo-refractive effect and thermal expansion. A similar behavior is observed when the input power is increased (c) due to the absorption of optical power by the silica, leading to heating of the microtoroid cavity. The duration of a frequency scan is around 15 ms what is long enough to let the microtoroid heat up and thermalize following the absorption of optical power. Resonance frequency shifts (red dots) at various temperatures (b) and input powers (d). A linear fit to the resonance frequency shifts (red dashed curve) gives a dependence of the resonance frequency on the temperature of -1.72 GHz/K (b). Similarly a dependence of the resonance frequency on the input power of -0.8 MHz/µW is found from (d).

(2.13), which combines into

$$\hbar\omega_d|\bar{a}|^2 = \frac{4\eta/\kappa}{1+\left(\bar{\Delta}+2\omega_c\left(\alpha_T+\frac{1}{n}\frac{dn}{dT}\right)\beta\eta_{abs}\hbar\omega_d|\bar{a}|^2\right)^2}P_{in}, \tag{2.14}$$

admits three solutions when the input power exceeds a threshold given by

$$P_{thresh} = \left[3\sqrt{3}\left(\alpha_T+\frac{1}{n}\frac{dn}{dT}\right)\beta\eta_{abs}\eta(1-\eta)Q_c\right]^{-1}. \tag{2.15}$$

For typical parameters of our silica microtoroids ($(\alpha_T + \frac{1}{n}\frac{dn}{dT}) = -6.1\times10^{-6}$ K^{-1}, $\beta\eta_{abs} = 250$ K/W, $Q_c = 2\times10^6$) the lowest threshold power, achieved at critical coupling ($\eta = 1/2$), is around 250 µW. We usually perform the experiments presented in this thesis at input powers lower than this threshold power therefore avoiding thermal bistabilities.

2.2 Microtoroids as mechanical resonators

2.2.1 Classical representation of a mechanical oscillator

The simplest way of picturing a mechanical oscillator is as a mass on a spring. It consists of an object with mass m subjected to a restoring force, $\vec{F} = -k_x\vec{x}$ when displaced by a distance $\vec{x}$ from its equilibrium position. Considering displacements in one dimension only the equation of motion for such a system is given by $m\ddot{x} + k_x x = 0$, and has the solutions $x(t) = A\cos(\sqrt{k_x/m}t + \phi)$ where the amplitude A and the phase ϕ depends on the initial conditions of the system. The periodic motion of this simple mechanical oscillator corresponds to the evolution of a classical harmonic oscillator with frequency $\Omega_m = \sqrt{k_x/m}$. In order to get a feeling for the dependence of the oscillator's frequency on the oscillator's characteristics, it is convenient to make an analogy with the string of a guitar. Increasing the tension on a guitar string increases the pitch of the note produced when plucking the string. This is equivalent to getting a higher oscillation frequency by increasing the spring constant of the oscillator. Following the analogy, reducing the size of the oscillator increases the oscillator's frequency, in the same way as shortening the guitar string by fretting it gives access to higher pitched notes.

A guitar string cannot sustain a note forever though, and the reason is that its vibration is damped by the contact to the body of the guitar and to the surrounding air. Taking into account the damping of oscillations, the equation of motion of a mechanical oscillator becomes, $m\ddot{x} + k_v\dot{x} + k_x x = 0$, where k_v is the viscous damping coefficient which quantifies the frictional force opposing the motion of the oscillator. The equation of motion of the damped mechanical oscillator may be recast in more general terms that characterize any kind of damped harmonic oscillator, then reading $\ddot{x} + \Gamma_m\dot{x} + \Omega_m^2 x = 0$,

where $\Gamma_m = k_v/m$ is the energy damping rate, i.e. the rate at which the mechanical oscillator loses energy via friction. We can define a quality factor of the mechanical oscillator, $Q_m = \Omega_m/\Gamma_m$, which represents the ratio of energy stored by the oscillator over the energy lost per cycle due to the damping of its oscillations.

In order to finalize the modeling of the mechanical oscillator dynamics we must look at the response of the oscillator to an external force F_{ex}, what is described by the equation of motion,

$$m\frac{d^2x(t)}{dt^2} + m\Gamma_m\frac{dx(t)}{dt} + m\Omega_m^2 x(t) = F_{ex}(t). \tag{2.16}$$

Assuming that the force applied to the oscillator is periodic, the above equation is best solved in the Fourier domain [12] with solutions given by,

$$\mathcal{X}(\Omega) = \chi_m(\Omega)\mathcal{F}_{ext}(\Omega), \tag{2.17}$$

where we introduced the *mechanical susceptibility* of the oscillator,

$$\chi_m^{-1} = m\left(\Omega_m^2 - \Omega^2 - i\Omega\Gamma_m\right). \tag{2.18}$$

At low frequencies, $\Omega \ll \Omega_m$, the linear response of the oscillator to a sinusoidal force is simply given by its spring constant as $\chi_m(\Omega \ll \Omega_m) \approx (m\Omega_m^2)^{-1} = 1/k_x$. When the frequency of the external force is on the order of the oscillator's frequency ($\Omega \approx \Omega_m$) the response of the oscillator is resonant with a maximum gain at the resonance frequency $\Omega_{res} = \Omega_m\sqrt{1 - 1/2Q_m^2}$. The mechanical oscillators we consider in this thesis have high Q factors, $Q_m \gg 1$, so that we can safely identify the resonance frequency with the oscillator's frequency, i.e. $\Omega_{res} \equiv \Omega_m$, and the resonance response is then given by $\chi_m(\Omega_m) = (m\Omega_m\Gamma_m)^{-1} = Q_m/k_x$. At high frequencies, $\Omega \gg \Omega_m$, the oscillator cannot follow fast changing driving forces so its response drops by $1/m\Omega^2$. The oscillator do not respond instantaneously to an external force but with a phase delay given by $\arg(\chi_m) = \arctan[\Omega\Gamma_m/(\Omega_m^2 - \Omega^2)]$.

2.2.2 Quantum representation of a mechanical oscillator

We now consider the oscillator's position and momentum as Hermitian Hilbert space operators, $\hat{x}$ and $\hat{p}$, respectively. In the quantum framework the position and momentum operators do not commute but rather obey the commutation relation, $[\hat{x}, \hat{p}] = i\hbar$. The Hamiltonian of the mechanical harmonic oscillator is given by

$$\hat{H} = \frac{\hat{p}^2}{2m} + \frac{1}{2}m\Omega_m^2\hat{x}^2 \tag{2.19}$$

[12] The Fourier transform of a time-dependent function $f(t)$ is defined by, $f(\Omega) = \int_{-\infty}^{+\infty} f(t)e^{i\Omega t}dt$.

where the first term represents the kinetic energy of the quantum mechanical oscillator and the second term represents its potential energy.

We define a phonon annihilation and creation operators,

$$\hat{b} = \frac{1}{2}\left(\frac{\hat{x}}{x_{zpf}} + i\frac{\hat{p}}{p_{zpf}}\right), \qquad \hat{b}^\dagger = \frac{1}{2}\left(\frac{\hat{x}}{x_{zpf}} - i\frac{\hat{p}}{p_{zpf}}\right), \tag{2.20}$$

respectively, so that we may recast the Hamiltonian of the quantum harmonic oscillator in the form

$$\hat{H} = \hbar\Omega_m\left(\hat{b}^\dagger\hat{b} + \frac{1}{2}\right). \tag{2.21}$$

We have introduced the zero-point motion and the zero-point momentum of the mechanical harmonic oscillator,

$$x_{zpf} = \sqrt{\frac{\hbar}{2m\Omega_m}}, \qquad p_{zpf} = m\Omega_m x_{zpf}, \tag{2.22}$$

respectively, which indicate the standard deviation of the position and momentum of the oscillator in its quantum ground state. The creation and annihilation operators satisfy the commutation relation, $[\hat{b}, \hat{b}^\dagger] = 1$, and the operator $\hat{n}_m = \hat{b}^\dagger\hat{b}$ is the phonon number operator, whose average, $\langle\hat{b}^\dagger\hat{b}\rangle = n_m$, is the mean phonon occupation of the mechanical oscillator. In the following we will discard the last term in Equation (2.21) which represents the constant zero-point energy of the oscillator, i.e. the ground state energy of the oscillator $\langle 0|\hat{H}|0\rangle = \hbar\Omega_m/2$, where $|0\rangle$ represents the vacuum state of the mechanical oscillator.

2.2.3 A mechanical oscillator in thermal equilibrium

A mechanical oscillator in equilibrium with its environment is naturally driven by the thermal energy of its environment which couples via the damping rate Γ_m. The motion of a mechanical oscillator in thermal equilibrium with its environment is associated with Brownian motion, i.e. a non-Markovian random process, and follows sinusoidal oscillations with random amplitude and phase varying on a time scale set by the damping rate Γ_m^{-1} [74]. Furthermore the motion of real mechanical resonators, such as microtoroids, combines the vibrations of a collection of quantum harmonic oscillators, which makes it difficult to directly analyze this motion in real-time. Therefore it is common to analyze the spectral components of the oscillator's motion in the frequency domain, where the contribution of each harmonic oscillator can be distinguished from the others.

The motion of the mechanical oscillator is best described in the frequency domain by the power spectral density (cf. 1.2.6) of the position operator,

$$S_{\delta\hat{x}}(\Omega) = \int_{-\infty}^{+\infty}\langle\delta\hat{x}(t)\delta\hat{x}(0)\rangle e^{i\Omega t}dt\ . \tag{2.23}$$

In the quantum regime, the time-evolutions of the position operator do not commute therefore the PSD is not symmetric [75]. This asymmetry has even been observed experimentally for a mechanical resonator near its quantum ground state [76]. It is however common to define a symmetric or single-sided PSD,

$$\mathcal{S}_{\delta\hat{x}}(\Omega) = \frac{1}{2}\left(S_{\delta\hat{x}}(\Omega) + S_{\delta\hat{x}}(-\Omega)\right), \tag{2.24}$$

which is equal to the double-sided PSD in the classical limit. In the following we consider single-sided PSD of the mechanical position operators.

For a mechanical oscillator in thermal equilibrium with its environment at a temperature T, the fluctuation-dissipation theorem connects the PSD of the oscillator's position to the dissipative part of the oscillator's susceptibility [75],

$$\mathcal{S}_{\delta\hat{x}}(\Omega) = \hbar \coth\left(\frac{\hbar\Omega}{2k_BT}\right) \mathrm{Im}(\chi_m(\Omega)) \underset{k_BT \gg \hbar\Omega}{\longrightarrow} \frac{2k_BT}{\Omega} \mathrm{Im}(\chi_m(\Omega)). \tag{2.25}$$

The last part of Equation (2.25) represents the classical high-temperature case where the thermal energy from the environment drives the oscillator to a high mean phonon occupation ($n_m \gg 1$). For a single high-Q mechanical oscillator the PSD shows a Lorentzian-like resonance with width Γ_m at frequency Ω_m, and by integrating over the frequency spectrum we find the variance of the oscillator's position to be

$$\langle \delta\hat{x}^2 \rangle = x_{zpf}^2 \coth\left(\frac{\hbar\Omega_m}{2k_BT}\right) \underset{k_BT \gg \hbar\Omega}{\longrightarrow} x_{zpf}^2 \frac{2k_BT}{\hbar\Omega_m}. \tag{2.26}$$

This relates the variance of the oscillator's position to the temperature of the environment when the oscillator is only thermally excited. We may generalize the notion of the temperature of a mechanical oscillator to any oscillator in an equilibrium state, by defining an effective temperature associated to the variance of the oscillator's position,

$$T_{\mathit{eff}} = \frac{\langle \delta\hat{x}^2 \rangle}{x_{zpf}^2} \frac{\hbar\Omega_m}{2k_B} = \frac{n_m \hbar\Omega_m}{k_B}, \tag{2.27}$$

which can be calculated from the area under the PSD.

2.2.4 Mechanical modes of a microtoroid resonator

In a similar way as an optical resonator may sustain a variety of spectral and spatial modes, mechanical resonators as well display a variety of mechanical modes oscillating at different frequencies. The mechanical modes of a mechanical resonator are intrinsic acoustic modes determined by the geometry and mechanical properties of the resonator. The three-dimensional motion of an acoustic mode is represented by a vector field $\vec{u}(\vec{r}, t)$ which indicates the displacement at time t of an infinitesimally small cubic volume

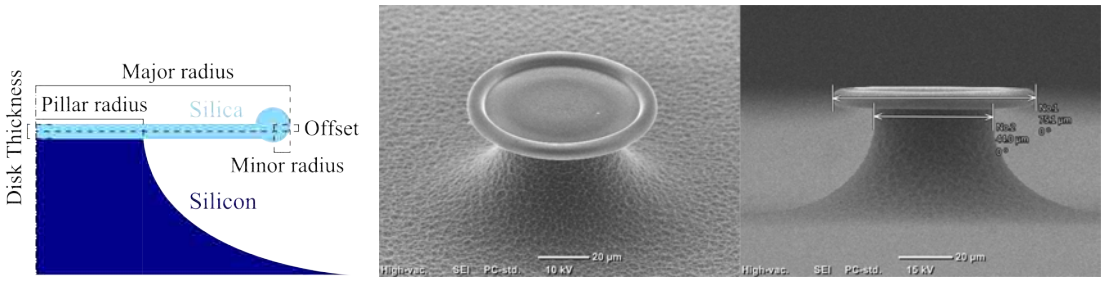

FIGURE 2.9: (a) Half-plane geometry of a macrotoroid with relevant parameters used in the FEM simulations. The complete three-dimensional model of a microtoroid is obtained by revolving the half-plane around its left-axis. The silica disk and torus are colored in light blue and the silicon pillar is colored in dark blue. (b) SEM micrographs of a microtoroid with major radius around 37.5 µm and pillar radius around 22 µm. The dimensions of the microtoroid measured with a SEM provide an indication on the typical dimensions of the microtoroids we use in our experiments.

element at position $\vec{r}$. Considering an isotropic homogeneous material in the absence of external forces, the displacement field obeys the following elastodynamics wave equation

$$\rho \frac{\partial^2 \vec{u}}{\partial t^2}(\vec{r},t) = (\lambda+\mu)\vec{\nabla}\left(\vec{\nabla}\cdot\vec{u}(\vec{r},t)\right) + \mu\left(\vec{\nabla}\cdot\vec{\nabla}\right)\vec{u}(\vec{r},t), \tag{2.28}$$

where the density of the material constituting the mechanical resonator is denoted by ρ, and its Lamé constants by

$$\lambda = \frac{\sigma E}{(1+\sigma)(1-2\sigma)} \tag{2.29}$$

$$\mu = \frac{E}{2(1+\sigma)}, \tag{2.30}$$

with σ its Poisson's ratio and E its Young modulus. Due to the finite dimensions of real mechanical resonators the wave equation accepts a discrete spectrum of solutions which form the set of orthonormal[13] mechanical modes of the resonator $\{\vec{u}_n(\vec{r},t) = \vec{u}_n(\vec{r})e^{-i\Omega_n t}, n \in \mathbb{N}\}$ with eigenfrequencies Ω_n. Any elastic deformation of the resonator can then be written as a linear combination of the mechanical modes,

$$\vec{u}(\vec{r},t) = \sum_n d_n(t)\vec{u}_n(\vec{r}), \tag{2.31}$$

where $d_n(t) = \langle \vec{u}(\vec{r},t), \vec{u}_n(\vec{r})\rangle$ is the time-dependent displacement amplitude of the n-th mode.

[13] In the sens of the spatial scalar product defined by

$$\langle \vec{A}(\vec{r}), \vec{B}(\vec{r})\rangle = \frac{1}{V}\int_V \vec{A}(\vec{r})\vec{B}(\vec{r})d^3r.$$

The complex geometry and composition of a microtoroid, i.e. a silica torus built around a silica disk supported by a silicon pillar, prevents the direct analytical derivation of the mechanical modes from the elastodynamics wave equation. Therefore we resort to FEM simulations to determine the mechanical eigenfrequencies and eigenmodes of our microtoroids. The geometry of the toroid used in our simulations is depicted in Figure 2.9(a). The parameters that we may vary are the major and minor radii of the torus, the radius of the pillar, the thickness of the disk, and the offset of the plane of the torus relative to the plane of the disk. We assume a rotational symmetry of the toroid around the central axis of the torus and pillar for facilitating the simulations. This is a reasonable assumption given the precision achieved in microtoroid fabrication, as can be seen on the scanning electron microscope (SEM) pictures in Figure 2.9(b). Even though the design geometry is rotationally symmetric the discrete mesh consisting of more than 10,000 nodes is not evenly distributed across the microtoroid geometry what leads to a lift of degeneracy between mechanical modes. The lift of degeneracy is also observed experimentally as our microtoroids are obviously not perfectly symmetric.

Figure 2.10 shows the displacement field of the 21 lowest-frequency mechanical eigenmodes obtained by solving Equation (2.28) via a FEM simulation. The microtoroid used in the simulation has major radius 38.1 μm, minor radius 3.1 μm, pillar radius 18.4 μm, disk thickness 2.86 μm, and offset 1.57 μm. This parameters were selected following the prior knowledge of the typical dimensions of our microtoroids measured with a SEM, and in order to match the simulated eigenfrequencies with the mechanical resonance frequencies obtained from the recorded noise power spectrum shown on Figure 2.11. This noise spectrum results from the transduction of mechanical displacements onto the optical field of the microtoroid cavity, thus providing an indication on the optomechanical coupling strength of the various mechanical mode to the optical cavity mode. Details on the measurement procedures will be given in a later part of this thesis. Most of the peaks displayed on the noise power spectrum corresponds to thermally excited mechanical resonances of the microtoroid, and by comparing their frequencies with the one obtained by FEM simulations we may identify each measured resonance with their displacement field.

Among the variety of mechanical modes shown in Figure 2.10 we may distinguish a family of modes known as *crown modes* [77] characterized by sinusoidal oscillations in the vertical direction along the torus perimeter (1, 3, 4, 6, 8, 12, 16, 21). Each crown mode possess a frequency degenerate pair mode for which the nodes and antinodes are swapped. Other modes involve a deformation of the silicon pillar, such as modes 7 and 15, or of both the silicon pillar and the silica torus, such as modes 10 and 13. The majority of these modes however couple poorly to the toroid optical cavity field and are therefore of little interest in the context of this thesis, namely optomechanics.

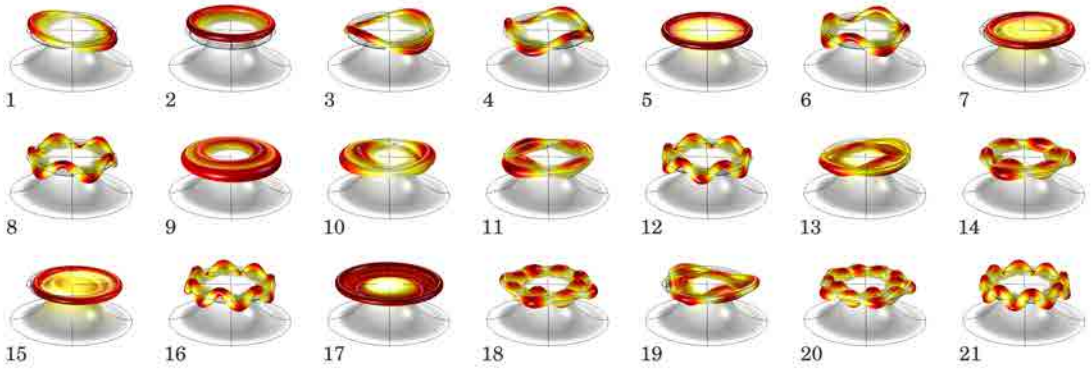

FIGURE 2.10: Mode shapes of the 21 lowest-frequency modes of a microtoroid resonator obtained from FEM simulations. The color code indicates the amplitude of the deformation of the microtoroid, from white to dark red. The initial geometry of the microtoroid at rest is represented by black wires. Modes 1, 3, 4, 6, 8, 12, 16, and 21 are crown modes. Mode 5 is a torsion mode. Mode 17 is the radial breathing mode and mode 2 is the fundamental flexural mode.

The most interesting modes for experiments in optomechanics are the mechanical modes displaying a radially symmetric displacement field, such as modes 2, 9 and 17. Mode 17 shows the highest coupling to the optical cavity mode of the microtoroid, as seen on Figure 2.11, and consists mainly of a radial expansion and contraction of the silica torus, thus its name, the *radial breathing mode* (RBM). Mode 2 involves the flexural motion of the silica disk, thereby making the torus oscillating in the vertical direction, and it is referred to as the *fundamental flexural mode* (FFM). The resonance frequency of the FFM lies in a frequency range more easily accessible by common laboratory electronics (e.g. electronic amplifiers, signal generators) and optical components (e.g. optical modulators, high-efficiency photo-diodes) compared to the frequency of the RBM which is one order of magnitude higher. In this thesis we focus our interest onto the FFM.

2.2.5 From a 3D displacement field to a scalar displacement

The three-dimensional displacement field of a mechanical modes constitutes a rather complex and cumbersome analytical model for studying the dynamics of a microresonator. It is preferable to describe the time-dependent motion of a mechanical resonator as a scalar displacement field $x(t)$, and recover the formalism introduced in the beginning of this thesis' section.

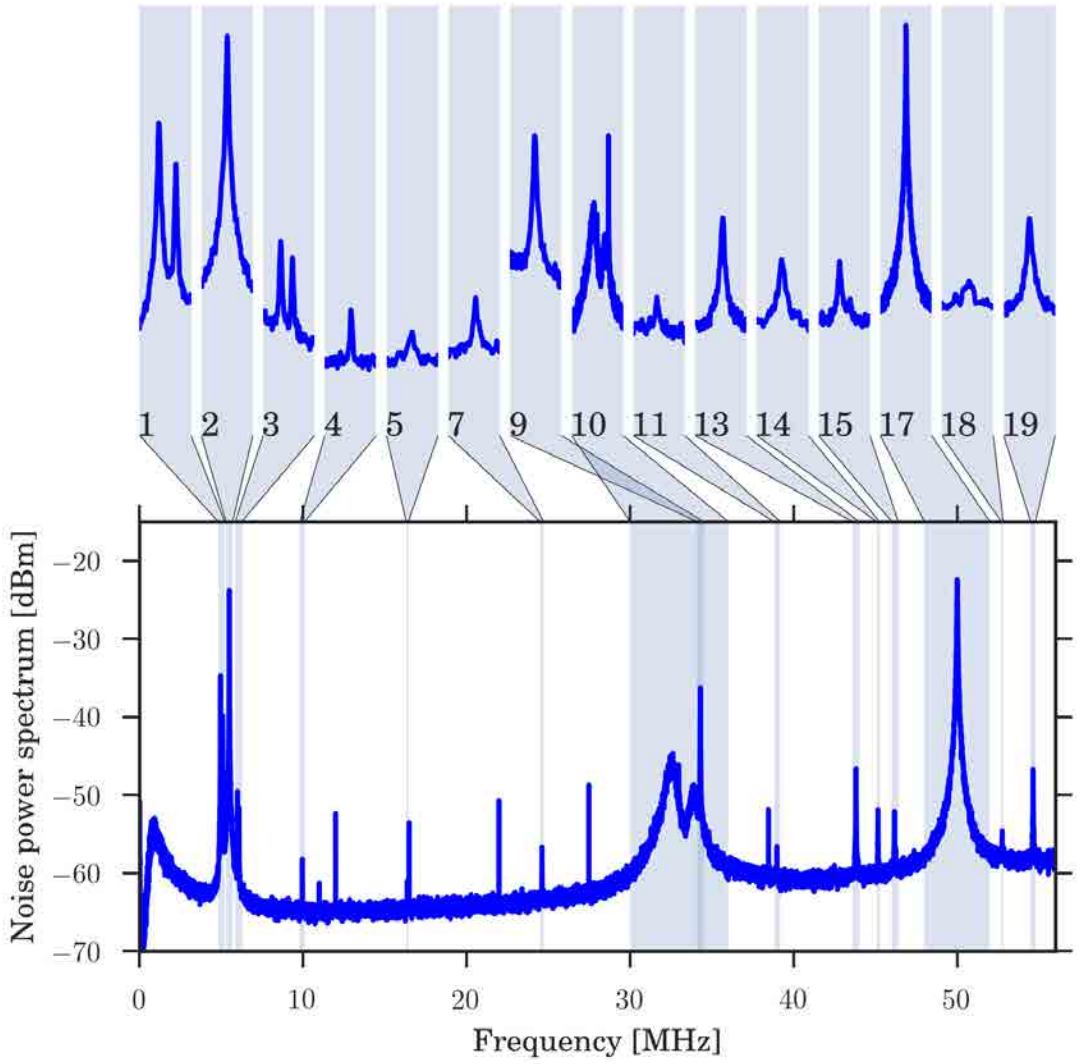

FIGURE 2.11: Noise power spectrum showing mechanical resonances. Each resonance is identified with a mechanical mode obtained by FEM simulation. Peaks appearing on the power spectrum at 11 MHz, 16.5 MHz, 22MHz, 27.5 MHz, 33 MHz, 38.5 MHz are artifacts of the fast Fourier transform algorithm used in the measurement procedure that will be presented in a later part of this thesis. The peak at 12 MHz comes from a modulation internal to the laser unit of our experimental setup. The modes 6, 8, 12 and 16, corresponding to crown modes, do not appear on the noise spectrum as they couple poorly to our measurement apparatus.

We may define the scalar displacement $x(t)$ to be the scalar projection of the displacement field $\vec{u}(\vec{r},t)$ onto a weighting vector $\vec{w}(\vec{r})$, readily

$$\begin{aligned} x(t) &= \langle \vec{w}(\vec{r}), \vec{u}(\vec{r},t) \rangle \,, \\ &= \sum_n d_n(t) \, \langle \vec{w}(\vec{r}), \vec{u}_n(\vec{r}) \rangle \,, \\ &= \sum_n x_n(t), \end{aligned} \tag{2.32}$$

where $x_n(t)$ represents the time-dependent scalar displacement of the n-th mechanical eigenmode of the resonator. The weighting function can be chosen such that the scalar displacement corresponds to a particular displacement of the microresonator, e.g. displacements along the vertical or radial direction of a microtoroid resonator, or more specifically in relation to a physical process dependent on the mechanical displacements such as optomechanical or electromechanical coupling. For example, in the framework of optomechanics involving a Fabry-Pérot cavity with a movable mirror, a judicious choice of the weighting function connects the scalar displacement to the center-of-mass mirror movement if it was displaced as a whole [78].

Effective mass of a mechanical oscillator

In order to complete the representation of the microresonator's displacement as a scalar displacement we must define an effective mass for each mechanical eigenmode. Starting with the displacement field of Equation (2.31), the potential energy of the mechanical resonator is given by [78]

$$U = \sum_n \frac{1}{2} m_n \Omega_n^2 |d_n(t)|^2, \tag{2.33}$$

where we have introduced the moving mass of the n-th mechanical eigenmode as $m_n = \int_V \rho |\vec{u}_n(\vec{r})|^2 d^3r$, with ρ the mass density of the microresonator's constituent medium. For an isotropic medium and because of the normalization of the mechanical eigenmodes, the moving masses of all eigenmodes are equal and given by the mass of the volume over which the integral is performed. The definition of the effective mass of the mechanical eigenmodes ensues from the preservation of the potential energy when projecting the displacement field onto a scalar displacement, i.e.

$$U = \sum_n \frac{1}{2} m_{eff,n} \Omega_n^2 |x_n(t)|^2, \tag{2.34}$$

implying that the effective mass reads,

$$m_{eff,n} = \frac{m_n}{\langle \vec{w}(\vec{r}), \vec{u}_n(\vec{r}) \rangle^2}. \tag{2.35}$$

Scalar projection of external forces

In the representation of the resonator's displacement as a scalar displacement, forces acting on the resonator must also be projected onto the scalar space such that we can describe the motion of the resonator with Equation (2.16). The total energy of the mechanical resonator subjected to an external force $\vec{F}_{ex}(\vec{r}, t)$ is given by [78],

$$\mathcal{H} = \sum_n \frac{1}{2} m_n \left(\frac{dd_n}{dt}(t) \right)^2 + \frac{1}{2} m_n \Omega_n^2 \left(d_n(t) \right)^2 - d_n(t) \left\langle \vec{F}_{ex}(\vec{r}, t), \vec{u}_n(\vec{r}) \right\rangle, \tag{2.36}$$

which is the sum of the energies of all mechanical eigenmode where the first term denotes the kinetic energy of the n-th mechanical eigenmode, the second its potential energy, and the last term represents the work of internal constraints opposed to the external force acting on the resonator. The equation of motion for each mechanical mode are then derived from Hamilton's equations, and reads

$$m_n \frac{d^2 d_n}{dt^2}(t) + m_n \Omega_n^2 d_n(t) = \left\langle \vec{F}_{ex}(\vec{r}, t), \vec{u}_n(\vec{r}) \right\rangle . \tag{2.37}$$

By using the definitions of the scalar displacement and effective mass introduced in Equations (2.32) and (2.35), respectively, we may recast Equation (2.37) into scalar space, i.e.

$$m_{eff,n} \frac{dx_n}{dt}(t) + m_{eff,n} \Omega_n^2 x_n(t) = F_{ex,n}(t), \tag{2.38}$$

where the external scalar force acting on the n-th mechanical eigenmode is equal to

$$F_{ex,n}(t) = \left\langle \vec{F}_{ex}(\vec{r}, t), \vec{u}_n(\vec{r}) \right\rangle \langle \vec{w}(\vec{r}), \vec{u}_n(\vec{r}) \rangle . \tag{2.39}$$

Note that the scalar force contributing to the dynamics of the n-th mechanical eigenmode of the resonator is the projection of the external vector force onto the n-th component of the weighting vector decomposed in the orthonormal basis $\{\vec{u}_n(\vec{r}),\, n \in \mathbb{N}\}$, therefore the total external scalar force acting on the resonator's displacement $x(t)$ is the scalar projection of the vector force on the weighting vector, i.e

$$\begin{aligned} F_{ex}(t) &= \sum_n F_{ex,n}(t), \\ &= \left\langle \vec{F}_{ex}(\vec{r}, t), \sum_n \langle \vec{w}(\vec{r}), \vec{u}_n(\vec{r}) \rangle \, \vec{u}_n(\vec{r}) \right\rangle , \\ &= \left\langle \vec{F}_{ex}(\vec{r}, t), \vec{w}(\vec{r}) \right\rangle , \end{aligned} \tag{2.40}$$

which is consistent with the definition of the scalar projection of the displacement field in Equation (2.32).

In the rest of this thesis we will continue our analysis of a mechanical resonator's motion in the scalar representation, and we will mostly focus on the dynamics of a single mechanical eigenmode of the resonator for simplicity.

2.3 Microtoroids as a cavity optomechanical system

2.3.1 Nature of the optomechanical coupling

A generic cavity optomechanical system is obtained by combining the Fabry-Pérot optical cavity presented in Section 2.1 with the mass-on-a-spring oscillator introduced in

Section 2.2 (Figure 2.12). A light field is coupled through a fixed partially transmitting mirror on one side of the Fabry-Pérot cavity, and is reflected onto a highly-reflective movable mirror on the other side. A radiation pressure force resulting from the momentum imparted upon reflection of the optical cavity field drives the motion of the movable mirror. At the same time the motion of the movable mirror alters the boundary conditions of the optical cavity, thereby changing its resonance properties. The displacement of the boundary conditions can be represented by a scalar displacement $x(t)$ (cf. 2.2.5), such that the resonance frequency of an optical mode of the cavity is shifted by

$$\omega_c(x(t)) = \omega_0 + g(x(t) - x_0) + \underset{x \to x_0}{o}(x(t) - x_0), \tag{2.41}$$

where x_0 corresponds to an equilibrium of the system and can be set to an arbitrary value by an appropriate choice of system coordinates. Equation (2.41) is nothing else than a Taylor series where $\omega_0 = \omega_c(x_0)$ is the resonance frequency of the optical cavity mode in equilibrium, and we have introduced the *optomechanical coupling parameter*

$$g = \frac{\partial \omega_c}{\partial x}(x_0). \tag{2.42}$$

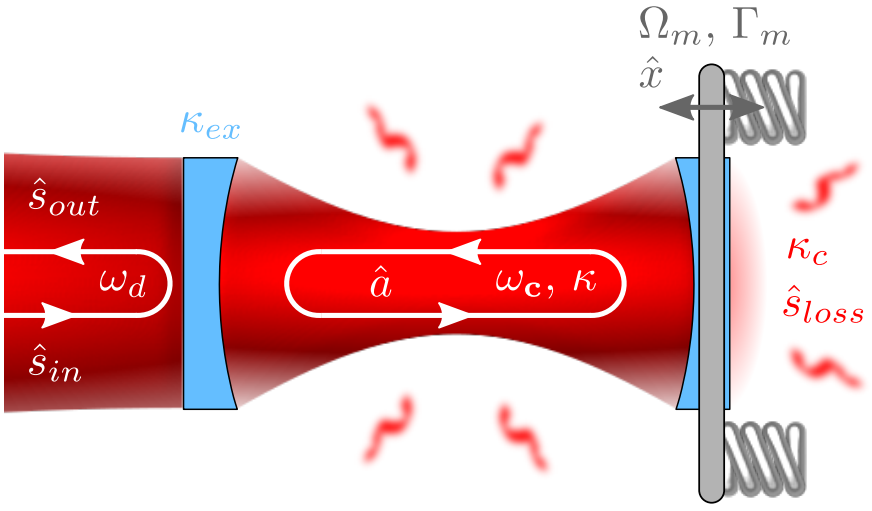

FIGURE 2.12: Optomechanical Fabry-Perot cavity consisting of a single-sided Fabry-Perot optical cavity with a highly-reflective movable mirror. The optical cavity has a resonance frequency ω_c and a width $\kappa = \kappa_{ex} + \kappa_c$, and is driven by an input field $\hat{s}_i n$ at frequency ω_d coupling to the cavity mode field $\hat{a}$ through a partially transmitting mirror at a rate κ_{ex} . The cavity mode field suffers optical loss described by the coupling to a loss channel field $\hat{s}_{loss}$ at a rate κ_c. The movable mirror's position $\hat{x}$ oscillates at a frequency Ω_m with a dissipation rate Γ_m.

The last term in Equation (2.41) is negligible for small displacements, $x(t) - x_0$, relative to the size of the optical cavity. This is the case when considering the motion of a microtoroid resonator, so it will be omitted in the rest of this thesis.

We know from Section 2.1 that the frequency of an optical cavity resonance is inversely proportional to the length of the cavity, therefore it is usual to set $g = -\omega_0/L$ for a Fabry-Pérot cavity of length L, and $g = -\omega_0/R$ for a WGM resonator of radius R, by an appropriate scaling of the scalar displacement.

2.3.2 Mechanically-induced modulation of the optical field

Taking into account the resonance frequency shift due to the moving boundary of the cavity, the (classical) time-evolution of the cavity field driven by a monochromatic input with constant amplitude $\bar{s}_{in}$ and frequency ω_d is given by

$$\dot{a}(t) = \left(-i(\omega_0 + gx(t)) - \frac{\kappa}{2}\right) a(t) + \sqrt{\kappa_{ex}}\bar{s}_{in} e^{-i\omega_d t}, \tag{2.43}$$

where we have set $x_0 = 0$ for simplicity. By considering the mechanical displacement as a classical harmonic oscillation $x(t) = \delta x \sin(\Omega_m t)$, the solution for the intracavity field amplitude reads,

$$a(t) = \sqrt{\kappa_{ex}}\bar{s}_{in} \sum_{n=-\infty}^{+\infty} \frac{(-i)^n \, \mathrm{J}_n(\xi)}{\kappa/2 - i(\Delta + n\Omega_m)} e^{-i(\omega_d + n\Omega_m)t + i\xi\cos(\Omega_m t)} \ , \tag{2.44}$$

after all transient have decayed on a timescale of the photon cavity lifetime κ^{-1} [77]. In the above, we introduced the detuning $\Delta = \omega_d - \omega_0$ of the driving field with respect to the cavity resonance in the equilibrium position x_0, and the modulation depth $\xi = g\delta x/\Omega_m$. We used the identity, $\exp(-i\xi\cos(\Omega_m t)) = \sum_{n=-\infty}^{+\infty}(-i)^n \, \mathrm{J}_n(\xi)\exp(in\Omega_m t)$ [25], to expand a complex modulated exponential into a series of Bessel functions of the first kind, J_n ($n \in \mathbb{Z}$). For a small modulation depth, $\xi \ll 1$, the modulated intracavity field amplitude can be approximated to,

$$a(t) \approx \bar{a} e^{-i\omega_d t} \left[1 + \underbrace{\frac{\bar{\Omega}_m}{1 - i(\bar{\Delta} + \bar{\Omega}_m)} \frac{\xi}{2} e^{-i\Omega_m t}}_{\text{anti-Stokes}} - \underbrace{\frac{\bar{\Omega}_m}{1 - i(\bar{\Delta} - \bar{\Omega}_m)} \frac{\xi}{2} e^{i\Omega_m t}}_{\text{Stokes}} \right] \ , \tag{2.45}$$

where $\Omega_m = 2\Omega_m/\kappa$ is the sideband resolution parameter, indicating the number of mechanical oscillations a photon can experience before escaping the cavity, and $\bar{Delta} = 2\Delta/\kappa$ is the normalized detuning. $\bar{a}$ is the mean intracavity field amplitude in the frame rotating at the input field frequency ω_d, and in the absence of mechanical interaction (cf. Equation (2.5)). Comparing Equation (2.45) with Equations (1.14) and (1.16), it is clear

that the mechanical oscillator acts as a modulator for the intracavity field amplitude. Via the optomechanical interaction, intracavity photons at the drive frequency ω_d are scattered into lower and upper sidebands, also referred to as Stokes and anti-Stokes sidebands, at frequencies $\omega_d - \Omega_m$ and $\omega_d + \Omega_m$, respectively. The probability for a photon to scatter into the Stokes or anti-Stokes sidebands is determined by the cavity resonance. For non-zero detuning the asymmetries between the amplitudes and phases of the Stokes and anti-Stokes sideband fields translate in both an amplitude and phase modulation of the intracavity field. At zero detuning the intracavity field amplitude reads,

$$a(t) \approx \bar{a} e^{-i\omega_d t} \left(1 + \frac{\bar{\Omega}_m}{1+\bar{\Omega}_m^2} \frac{\xi}{2} \left[(1 + i\bar{\Omega}_m) e^{-i\Omega_m t} - (1 - i\bar{\Omega}_m) e^{i\Omega_m t} \right] \right) , \tag{2.46}$$

$$\approx \bar{a} e^{-i\omega_d t} \left(1 + i\xi \frac{\bar{\Omega}_m}{1+\bar{\Omega}_m^2} \left[\bar{\Omega}_m \cos(\Omega_m t) - \sin(\Omega_m t) \right] \right) , \tag{2.47}$$

thus carries only a phase modulation. Figure 2.13 illustrates the optomechanically induced phase modulation of the intracavity field in a phase space picture.

2.3.3 Radiation pressure backaction

While the motion of the cavity boundary affects the phase and amplitude of the optical intracavity field, at the same time the optical field exerts a radiation pressure force onto the cavity boundary. In the simple case of a Fabry-Pérot cavity, the radiation pressure force results from the momentum transfer of the photons upon reflection on the movable

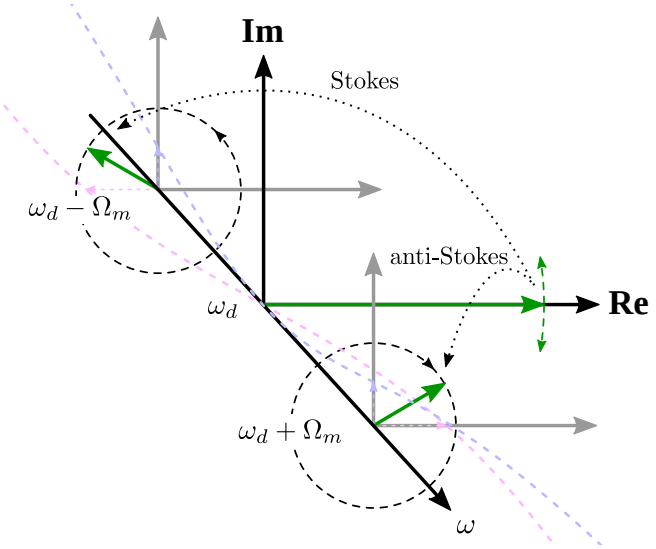

FIGURE 2.13: Phase space picture of the intracavity field carrying a phase modulation due to mechanically driven Stokes and anti-Stokes scattering of intracavity photons.

mirror, what gives

$$F_{rp}(t) = \frac{|a(t)|^2}{\tau_{rt}} 2\hbar k = \hbar \frac{\omega_d}{L} |a(t)|^2 = -\hbar g |a(t)|^2 \ , \tag{2.48}$$

where $\tau_{rt} = 2L/c$ is the cavity round-trip time, and $k = \omega_d/c$ is the momentum of the intracavity photons. Now taking into account the mutual coupling of the optical and mechanical degrees of freedom via the optomechanical interaction results in the coupled system of equations (cf. Equations (2.4) and (2.16)),

$$\dot{a}(t) = \left(i(\Delta - g x(t)) - \frac{\kappa}{2} \right) a(t) + \sqrt{\kappa_{ex}} s_{in}(t) \ , \tag{2.49}$$

$$m_{eff} \ddot{x}(t) + m_{eff} \Gamma_m \dot{x} + m_{eff} \Omega_m^2 x(t) = -\hbar g |a(t)|^2 \ , \tag{2.50}$$

for a mechanical oscillator with effective mass m_{eff}, natural frequency Ω_m and damping rate Γ_m.

Optomechanical bistability

By considering an input field with constant amplitude $\bar{s}_{in}$, stable solutions ($\bar{a}$, $\bar{x}$) of the coupled system of nonlinear differential equations can be derived by setting all time derivatives to zero, resulting in

$$\bar{a} = \frac{\sqrt{\kappa_{ex}} \bar{s}_{in}}{(\kappa/2 - i(\Delta - g\bar{x}))} \ , \qquad \bar{x} = -\frac{\hbar g |a(t)|^2}{m_{eff} \Omega_m^2} \ . \tag{2.51}$$

Figure 2.14 illustrates the solutions of the system of equations as the intersections of the two curves giving the mean number of intracavity photons $n_c = |\bar{a}|^2$ as a function of the mechanical displacement $\bar{x}$. The system possess at least one stable solution, and for input powers above the threshold condition [79],

$$|\bar{s}_{in}|^2 \geq \frac{\sqrt{3}}{9} \frac{\Omega_m^2 m_{eff} \kappa^2}{\eta \hbar g^2} \ , \tag{2.52}$$

the system accepts two additional solutions corresponding to one stable and one unstable equilibrium state of the optomechanical system. Above the threshold condition the optomechanical system exhibits a bistable behavior, which can be revealed experimentally in the hysteresis of the cavity transmission when varying the input power [80].

2.3.4 Optomechanical interaction Hamiltonian

Having described the classical phenomena related to radiation pressure interactions in a cavity optomechanical system, we must now look at the optomechanical coupling between stochastic fluctuations of the optical field and mechanical displacement. The

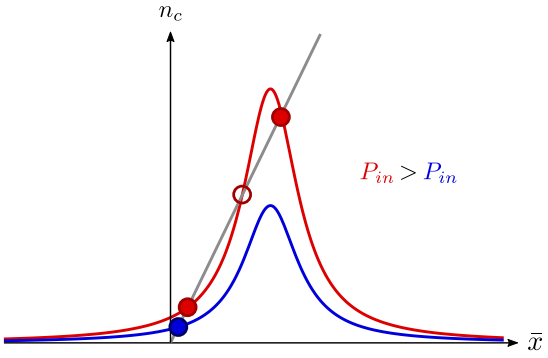

FIGURE 2.14: Illustration of the solutions of the system of equations (2.51). Each equation describes a curve mapping the mechanical displacement $\bar{x}$ onto the mean intracavity photon number n_c. The intersections of the two curves indicate solutions of the system of equations, i.e. equilibrium states of the optomechanical system. Full circles denote stable equilibrium states and empty circles denote unstable equilibrium states.

Hamiltonian formulation of a generic optomechanical system [81] considers the interaction of a single optical mode with a single mechanical harmonic oscillator, so that the Hamiltonian reads

$$\hat{H} = \frac{\hat{p}^2}{2m_{eff}} + \frac{1}{2}m_{eff}\Omega_m^2\hat{x}^2 + \hbar\omega_0\left(\hat{a}^\dagger\hat{a} + \frac{1}{2}\right) + \hbar g\hat{x}\hat{a}^\dagger\hat{a} \tag{2.53}$$

where $\hat{x}$ and $\hat{p}$ are the position and momentum operators of the mechanical oscillator with effective mass m_{eff} and natural frequency Ω_m. $\hat{a}^\dagger$ and $\hat{a}$ are the photon creation and annihilation operators of the optical mode with photon number operator $\hat{n}_c = \hat{a}^\dagger\hat{a}$ and resonance frequency ω_0. An alternative way of writing the Hamiltonian of the optomechanical system expresses the mechanical oscillator's position and momentum operators in terms of phonon annihilation and creation operators, $\hat{b}$ and $\hat{b}^\dagger$ defined in Equation (2.20), respectively, such that

$$\hat{H} = \hbar\Omega_m\left(\hat{b}^\dagger\hat{b} + \frac{1}{2}\right) + \hbar\omega_0\left(\hat{a}^\dagger\hat{a} + \frac{1}{2}\right) + \hbar g_0\left(\hat{b} + \hat{b}^\dagger\right)\hat{a}^\dagger\hat{a}, \tag{2.54}$$

where we have introduced the *vacuum optomechanical coupling rate* $g_0 = g \cdot x_{zpf}$. The last two terms in Equations (2.53) and (2.54) represent the energy of the free cavity field with its resonance frequency shifted by the moving boundary condition according to Equation (2.41). The other terms represent the energy of the mechanical harmonic oscillator.

2.3.5 Quantum Langevin equations

The Hamiltonian representation introduced above describes a closed system with no addition or dissipation of energy. The dissipative dynamics of the optomechanical system driven by an input field $\hat{s}_{in}e^{-i\omega_d t}$ is described by a set of quantum Langevin equations (QLE) [82] written in the frame rotating at the input field frequency,

$$\frac{d\hat{a}}{dt}(t) = \left(i\Delta - \frac{\kappa}{2}\right)\hat{a} - ig\hat{x}(t)\hat{a}(t) + \sqrt{\kappa_{ex}}\hat{s}_{in}(t) + \sqrt{\kappa_c}\hat{s}_{loss}(t), \tag{2.55}$$

$$\frac{d\hat{x}}{dt}(t) = \frac{\hat{p}(t)}{m_{eff}}, \tag{2.56}$$

$$\frac{d\hat{p}}{dt}(t) = -m_{eff}\Omega_m^2\hat{x}(t) - \hbar g\hat{a}^\dagger\hat{a} - \Gamma_m\hat{p}(t) + \hat{F}_{ex}(t). \tag{2.57}$$

where $\Delta = \omega_d - \omega_0$ indicates the detuning of the drive field from the cavity resonance, Γ_m is the damping rate at which energy is dissipated from the mechanical oscillator, and the operator $\hat{F}(t)$ comprises the forces that act on the mechanical oscillator, excluding the radiation pressure force from the intracavity field. Additionally to the input field, the intracavity field is driven by field fluctuations from the loss port of the cavity $\hat{s}_{loss}(t)$.

Linearized equations of motion

The optomechanical interaction involves the nonlinear mixing of optical and mechanical field operators. However since we are interested in the small fluctuations of the optical and mechanical fields we linearize the QLE by separating the field operators into a mean value component corresponding to the classical part of the field amplitude, and a noise operator corresponding to the stochastic fluctuations of the field amplitude around its mean, e.g.

$$\hat{a}(t) = \bar{a} + \delta\hat{a}(t), \tag{2.58}$$

for the cavity mode field, where $\langle\hat{a}\rangle = \bar{a}$ and $\langle\delta\hat{a}\rangle = 0$. The mean values of the field amplitudes are obtained from the static part of the QLE. By assuming $(\bar{x}, \bar{a})$ to belong to a stable state of the optomechanical system, the linearized QLE for the fluctuations of optical and mechanical field amplitudes are obtained by keeping only terms of first order in the fluctuations, reading

$$\frac{d}{d}\delta\hat{a}(t) = \left(i\Delta - \frac{\kappa}{2}\right)\delta\hat{a}(t) - ig\bar{a}\delta\hat{x}(t) + \sqrt{\kappa_{ex}}\delta\hat{s}_{in}(t) + \sqrt{\kappa_c}\delta\hat{s}_{loss}(t), \tag{2.59}$$

$$\frac{d}{dt}\delta\hat{x}(t) = \frac{\delta\hat{p}(t)}{m_{eff}}, \tag{2.60}$$

$$\frac{d}{dt}\delta\hat{p}(t) = -m_{eff}\Omega_m^2\delta\hat{x}(t) - \hbar g\bar{a}\left(\delta\hat{a}^\dagger(t) + \delta\hat{a}(t)\right) - \Gamma_m\delta\hat{p}(t) + \delta\hat{F}_{ex}(t), \tag{2.61}$$

where the detuning now takes into account the static frequency shift, $\Delta = \omega_d - \omega_0 - g\bar{x}$, induced by the mean of the radiation pressure and external forces applied to the cavity boundary, $\hbar g\bar{a}^2 + \langle \hat{F}_{ext} \rangle$.

As the annihilation and creation operators are not Hermitian operators and are therefore not measurable, it is preferable to write the optomechanical system dynamics in terms of amplitude and phase quadrature operators which are measurable observables, resulting in

$$\frac{d}{dt}\delta\hat{X}_a(t) = -\frac{\kappa}{2}\delta\hat{X}_a(t) - \Delta\delta\hat{P}_a(t) + \sqrt{\kappa_{ex}}\delta\hat{X}_{in} + \sqrt{\kappa_c}\delta\hat{X}_{loss}(t) \ , \tag{2.62}$$

$$\frac{d}{dt}\delta\hat{P}_a(t) = -\frac{\kappa}{2}\delta\hat{P}_a(t) + \Delta\delta\hat{X}_a(t) + \sqrt{\kappa_{ex}}\delta\hat{P}_{in} + \sqrt{\kappa_c}\delta\hat{P}_{loss}(t) - g_c\delta\hat{x}(t) \ , \tag{2.63}$$

$$\frac{d}{dt}\delta\hat{x}(t) = \frac{\delta\hat{p}(t)}{m_{eff}} \ , \tag{2.64}$$

$$\frac{d}{dt}\delta\hat{p}(t) = -m_{eff}\Omega_m^2\delta\hat{x}(t) - \hbar g_c\delta\hat{X}_a(t) - \Gamma_m\delta\hat{p}(t) + \delta\hat{F}_{ex}(t) \ , \tag{2.65}$$

where we have introduced the effective optomechanical coupling rate $g_c = \sqrt{2}g\bar{a}$.

When considering continuous monochromatic fields as input to the cavity optomechanical system, the QLEs are most conveniently solved in the Fourier domain. However, when considering pulsed fields as input, the QLEs must be solved in the time domain. The QLEs can be solved in the time or frequency domain depending

Chapter 3

Quantum-enhanced measurements of mechanical displacements

The interest in ultra high-sensitivity measurements of mechanical displacement was sparked by the quest for the detection of gravitational waves. Large-scale interferometers were designed to detect the infinitesimal deformation of space induced by the passing of a gravitational waves. The relative position of massive mirrors are measured continuously with a very high precision by detecting the interference of optical beams reflected off the mirrors. Early studies on the limits of position measurements in large-scale gravitational-wave detectors [5, 7, 83] set the basis of optical probing of mechanical displacements which found applications in spin detection [84], attometer-scale displacement measurements [30, 77], chip-based room temperature magnetometry [85], and dynamic biological measurements [86].

Two fundamental quantum noise contributions limit the sensitivity of continuous measurements of mechanical displacements. The *imprecision noise* is inherent to every optical measurement as it arises upon detection from the quantum fluctuations of the optical probe field. The *quantum backaction noise* (QBA) results from the driving of mechanical motion due to the stochastic radiation pressure force imparted by amplitude fluctuations of the probe field. The imprecision noise and the QBA noise follow inverse scalings with the probe power, therefore an optimal sensitivity, called the standard quantum limit (SQL), is reached when the two noise contributions are equal. Displacement measurements with an imprecision noise below the SQL have been performed [38, 40, 87, 88], and the QBA noise have also been observed [33, 89], but so far measurements at the SQL remain elusive.

In this chapter we investigate the use of squeezed light as a quantum sensing resource to enhance the sensitivity of displacement measurements. Squeezing-enhanced measurements have already been performed with Mach-Zehnder [90], Michelson [91–93], Sagnac [94], and large-scale gravitational-wave interferometers [95], and applied to displacement measurements of particles in biological samples [86], however there is little study of there applications in the context of cavity optomechanics with micromechanical resonator.

3.1 Continuous displacement sensing

3.1.1 Cavity optomechanics in the Fourier domain

While considering a cavity optomechanical system driven by a monochromatic laser field with constant amplitude, the QLEs are most easily solved in the Fourier domain where the fields are described by their spectral components. Using the Fourier transform on Equations 2.62, 2.63, 2.64, and 2.65, we obtain

$$-i\Omega\delta\hat{\mathcal{X}}_a(\Omega) = -\frac{\kappa}{2}\delta\hat{\mathcal{X}}_a(\Omega) - \Delta\delta\hat{\mathcal{P}}_a(\Omega) + \sqrt{\kappa_{ex}}\delta\hat{\mathcal{X}}'_{in}(\Omega) + \sqrt{\kappa_c}\delta\hat{\mathcal{X}}'_{loss}(\Omega)\ , \tag{3.1}$$

$$-i\Omega\delta\hat{\mathcal{P}}_a(\Omega) = -\frac{\kappa}{2}\delta\hat{\mathcal{P}}_a(\Omega) + \Delta\delta\hat{\mathcal{X}}_a(\Omega) + \sqrt{\kappa_{ex}}\delta\hat{\mathcal{P}}'_{in}(\Omega) + \sqrt{\kappa_c}\delta\hat{\mathcal{P}}'_{loss}(\Omega) - g_c\delta\hat{\chi}(\Omega)\ , \tag{3.2}$$

$$-i\Omega\delta\hat{\chi}(\Omega) = \frac{\delta\hat{p}(\Omega)}{m_{eff}}\ , \tag{3.3}$$

$$-i\Omega\delta\hat{p}(\Omega) = -m_{eff}\Omega_m^2\delta\hat{\chi}(\Omega) - \hbar g_c\delta\hat{\mathcal{X}}_a(\Omega) - \Gamma_m\delta\hat{p}(\Omega) + \delta\hat{\mathcal{F}}_{ex}(\Omega)\ . \tag{3.4}$$

The QLE in the Fourier domain can be conveniently written in matrix form by separating the noise sources from the field quadratures, such that

$$\begin{pmatrix} \delta\hat{\mathcal{X}}_a(\Omega) \\ \delta\hat{\mathcal{P}}_a(\Omega) \end{pmatrix} = \frac{2}{\kappa}\mathbf{M_c}\begin{pmatrix} \sqrt{\kappa_{ex}}\delta\hat{\mathcal{X}}'_{in}(\Omega) + \sqrt{\kappa_c}\delta\hat{\mathcal{X}}'_{loss}(\Omega) \\ \sqrt{\kappa_{ex}}\delta\hat{\mathcal{P}}'_{in}(\Omega) + \sqrt{\kappa_c}\delta\hat{\mathcal{P}}'_{loss}(\Omega) - g_c\delta\hat{\chi}(\Omega) \end{pmatrix}\ , \tag{3.5}$$

$$\begin{pmatrix} \delta\hat{\chi}(\Omega) \\ \delta\hat{p}(\Omega) \end{pmatrix} = \chi_m(\Omega)\left[-\hbar g_c\delta\hat{\mathcal{X}}_a(\Omega) + \delta\hat{\mathcal{F}}_{ex}(\Omega)\right]\begin{pmatrix} 1 \\ -im_{eff}\Omega \end{pmatrix}\ , \tag{3.6}$$

where we have introduced a dimensionless matrix mapping the field fluctuations from noise sources onto the intracavity field fluctuations,

$$\mathbf{M_c} = \frac{\kappa}{2}\chi_c(\Omega)\begin{pmatrix} \kappa/2 - i\Omega & -\Delta \\ \Delta & \kappa/2 - i\Omega \end{pmatrix}. \tag{3.7}$$

The transfer of field fluctuations from external noise sources to the optical cavity and mechanical resonator is described by an optical and mechanical susceptibility,

$$\chi_c(\Omega) = \left[\left(\frac{\kappa}{2} - i\Omega\right)^2 + \Delta^2\right]^{-1} , \tag{3.8}$$

$$\chi_m(\Omega) = \left[m_{eff}\left(\Omega_m^2 - \Omega^2 - i\Omega\Gamma_m\right)\right]^{-1} , \tag{3.9}$$

respectively. Fluctuations in the position and momentum of the mechanical resonator are driven by optical noise in the amplitude quadrature of the intracavity field via a radiation pressure interaction. Reciprocally, mechanical position fluctuations are transduced onto the amplitude and phase quadrature of the intracavity field on top of optical noise from the input and loss ports of the cavity. At zero detuning of the input field the mechanical noise affects only the phase quadrature fluctuations of the intracavity field, meaning that the radiation pressure force, proportional to the amplitude quadrature of the intracavity field, is independent of mechanical noise.

3.1.2 Probing the mechanical motion

In practice the optomechanical system observables, namely the amplitude and phase quadratures of the intracavity optical field and the position and momentum of the mechanical resonator, are not easily accessible and are inferred from measurements of the output field fluctuations exiting the optical cavity. We recall from Chapter 2 the input-output relation giving the output field fluctuations in terms of the input and intracavity field fluctuations,

$$\delta\hat{\mathcal{X}}'_{out} = \delta\hat{\mathcal{X}}'_{in} - \sqrt{\kappa_{ex}}\delta\hat{\mathcal{X}}_a , \tag{3.10}$$

$$\delta\hat{\mathcal{P}}'_{out} = \delta\hat{\mathcal{P}}'_{in} - \sqrt{\kappa_{ex}}\delta\hat{\mathcal{P}}_a , \tag{3.11}$$

then insert the intracavity field fluctuations given by Equation (3.5), such that we get the output field fluctuations in terms of the input and mechanical noise,

$$\begin{pmatrix} \delta\hat{\mathcal{X}}'_{out} \\ \delta\hat{\mathcal{P}}'_{out} \end{pmatrix} = (\mathbf{I_2} - 2\eta\mathbf{M_c}) \begin{pmatrix} \delta\hat{\mathcal{X}}'_{in} \\ \delta\hat{\mathcal{P}}'_{in} \end{pmatrix} - 2\sqrt{\eta(1-\eta)}\mathbf{M_c} \begin{pmatrix} \delta\hat{\mathcal{X}}'_{loss} \\ \delta\hat{\mathcal{P}}'_{loss} - \frac{g_c}{\sqrt{\kappa_c}}\delta\hat{\chi} \end{pmatrix} , \tag{3.12}$$

where $\mathbf{I_2}$ is the identity matrix of dimension 2. Here the input and output field quadratures are defined in the reference frame of the intracavity field, but it is more relevant to express the field quadratures in their own frame in order to account for the phase shift

induced by the cavity under a non-zero detuning Δ, such that

$$\begin{pmatrix} \delta\hat{\mathcal{X}}'_{out} \\ \delta\hat{\mathcal{P}}'_{out} \end{pmatrix} = \mathbf{R}(\phi_{out}) \begin{pmatrix} \delta\hat{\mathcal{X}}_{out} \\ \delta\hat{\mathcal{P}}_{out} \end{pmatrix} = \frac{1}{\sqrt{(1-2\eta)^2 + \bar{\Delta}^2}} \begin{pmatrix} 1-2\eta & \bar{\Delta} \\ -\bar{\Delta} & 1-2\eta \end{pmatrix} \begin{pmatrix} \delta\hat{\mathcal{X}}_{out} \\ \delta\hat{\mathcal{P}}_{out} \end{pmatrix} , \tag{3.13}$$

$$\begin{pmatrix} \delta\hat{\mathcal{X}}'_{in} \\ \delta\hat{\mathcal{P}}'_{in} \end{pmatrix} = \mathbf{R}(\phi_{in}) \begin{pmatrix} \delta\hat{\mathcal{X}}_{in} \\ \delta\hat{\mathcal{P}}_{in} \end{pmatrix} = \frac{1}{\sqrt{1+\bar{\Delta}^2}} \begin{pmatrix} 1 & \bar{\Delta} \\ -\bar{\Delta} & 1 \end{pmatrix} \begin{pmatrix} \delta\hat{\mathcal{X}}_{in} \\ \delta\hat{\mathcal{P}}_{in} \end{pmatrix} , \tag{3.14}$$

where the phases of the input and output field are defined by $\phi_{in,out} = \arg(\bar{s}_{in,out})$. The last equality in the above equations are derived from the classical input output relation of the mean field amplitudes (cf. Equations (2.5) and (2.6)). In the absence of detuning of the probe field from the cavity resonance, the phases of the output and output fields are equal to the phase of the intracavity field, and the rotation matrix $\mathbf{R}(\phi_{out})$ and $\mathbf{R}(\phi_{in})$ are equal to the identity matrix. Note that at critical coupling, $\eta = 1/2$, and for zero-detuning, $\bar{\Delta} = 0$, the phase of the output field is ill defined as the output field amplitude is null, $\bar{s}_{out} = 0$. In this case however, we chose the convention $\phi_{out} = 0$ for simplicity.

Arbitrary quadrature measurement

Continuous measurement of an arbitrary quadrature of the output field fluctuations can be performed with a balanced homodyne detector (cf. 1.3.3). The phase of the measured quadrature is given by the phase of the local oscillator relative to the output field, $\theta = \phi_{lo} - \phi_{out}$, such that the measured output quadrature reads,

$$\delta\hat{\mathcal{X}}^{\theta}_{out} = \cos(\theta)\delta\hat{\mathcal{X}}_{out} + \sin(\theta)\delta\hat{\mathcal{P}}_{out} . \tag{3.15}$$

For a real homodyne measurement of the output field fluctuations, information on the mechanical displacement fluctuations of a microresonator is best retrieved from the PSD of the homodyne difference current, whose relation with the PSD of the measured output quadrature fluctuations is given in Equation (1.94). In general the derivation of the PSD of the measured output quadrature is rather cumbersome as the optomechanical interaction generates correlations between the intracavity field fluctuations and the mechanical displacement fluctuations. However the calculations simplify considerably when considering zero-detuning between the input field and the cavity resonance. This situation is particularly relevant when considering the measurement of mechanical displacements as it corresponds to a maximum intracavity circulating power for a given input power, leading to a maximum transduction of the mechanical motion onto the intracavity field. By combining Equations (3.5) and (3.6) into Equation (3.10), and projecting the amplitude and phase quadratures of the output field onto the measured

quadrature, we obtain

$$\begin{aligned}\delta\hat{\mathcal{X}}^{\theta}_{out} = &\left[\cos(\theta) - \frac{2\eta}{1-i\bar{\Omega}}G(\theta)\right]\delta\hat{\mathcal{X}}_{in} + \left[1 - \frac{2\eta}{1-i\bar{\Omega}}\right]\sin(\theta)\delta\hat{\mathcal{P}}_{in} \\ &- \frac{2\sqrt{\eta(1-\eta)}}{1-i\bar{\Omega}}G(\theta)\delta\hat{\mathcal{X}}'_{loss} - \frac{2\sqrt{\eta(1-\eta)}}{1-i\bar{\Omega}}\sin(\theta)\delta\hat{\mathcal{P}}'_{loss} \\ &+ \frac{2\sqrt{\eta(1-\eta)}}{1-i\bar{\Omega}}\frac{g_c\chi_m}{\sqrt{\kappa_c}}\sin(\theta)\delta\hat{\mathcal{F}}_{ex}\ , \end{aligned} \tag{3.16}$$

where we introduced the function

$$G(\theta) = \cos(\theta) + \frac{2(1-\eta)}{1-i\bar{\Omega}}\frac{\hbar g_c^2}{\kappa_c}\chi_m\sin(\theta)\ , \tag{3.17}$$

which accounts for the correlated input noise driving the mechanical motion and the cavity mode.

Assuming that the noise sources are independent, the variance of the measured output field quadrature fluctuations are given by,

$$\begin{aligned}\langle|\delta\hat{\mathcal{X}}^{\theta}_{out}|^2\rangle = &\ Z_{in}(\theta)\langle|\delta\hat{\mathcal{X}}_{in}|^2\rangle + (1-Z_c)\sin^2(\theta)\langle|\delta\hat{\mathcal{P}}_{in}|^2\rangle \\ &+ Z_{loss}\langle|\delta\hat{\mathcal{X}}'_{loss}|^2\rangle + Z_c\sin^2(\theta)\langle|\delta\hat{\mathcal{P}}'_{loss}|^2\rangle \\ &+ Z_cZ_{rp}\frac{|\chi_m|^2}{\hbar}\sin^2(\theta)\langle|\delta\hat{\mathcal{F}}_{ex}|^2\rangle \\ &+ (1-Z_c)\cos(\theta)\sin(\theta)\langle\delta\hat{\mathcal{X}}_{in}\delta\hat{\mathcal{P}}_{in} + \delta\hat{\mathcal{P}}_{in}\delta\hat{\mathcal{X}}_{in}\rangle \\ &+ (1-\mathrm{Re}[\bar{\chi}_o\chi_m])\,Z_cZ_{rp}\sin^2(\theta)\langle\delta\hat{\mathcal{X}}_{in}\delta\hat{\mathcal{P}}_{in} + \delta\hat{\mathcal{P}}_{in}\delta\hat{\mathcal{X}}_{in}\rangle \\ &+ Z_c\cos(\theta)\sin(\theta)\langle\delta\hat{\mathcal{X}}'_{loss}\delta\hat{\mathcal{P}}'_{loss} + \delta\hat{\mathcal{P}}'_{loss}\delta\hat{\mathcal{X}}'_{loss}\rangle \\ &+ \mathrm{Re}[\bar{\chi}_o\chi_m]Z_cZ_{rp}\sin^2(\theta)\langle\delta\hat{\mathcal{X}}'_{loss}\delta\hat{\mathcal{P}}'_{loss} + \delta\hat{\mathcal{P}}'_{loss}\delta\hat{\mathcal{X}}'_{loss}\rangle\ , \end{aligned} \tag{3.18}$$

where we have introduced the following notations for simplifying the expression,

$$\begin{aligned}&Z_{in} = (1-Z_c)\cos^2(\theta) + Z_c^2Z_{rp}^2|\chi_m|^2\sin^2(\theta) + 2Z_cZ_{rp}\,\mathrm{Re}\left[(1-\bar{\chi}_o)\chi_m\right]\sin(\theta)\cos(\theta)\ , \\ &Z_{loss} = Z_c\cos^2(\theta) + Z_cZ_{rp}^2|\bar{\chi}_o\chi_m|^2\sin^2(\theta) + 2Z_cZ_{rp}\,\mathrm{Re}\left[\bar{\chi}_o\chi_m\right]\sin(\theta)\cos(\theta)\ , \\ &Z_c = \frac{4\eta(1-\eta)}{1+\bar{\Omega}^2}\ , \qquad Z_{rp} = \frac{\hbar g_c^2}{\kappa_c}\ , \qquad \bar{\chi}_o = \frac{2(1-\eta)}{1-i\bar{\Omega}} \end{aligned} \tag{3.19}$$

The last four lines in Equation (3.18) contains the possible correlations between conjugate quadrature fluctuations of the fields entering the cavity from the input and loss ports. For optical fields in a coherent or vacuum state, all quadrature fluctuations are uncorrelated and the four terms vanishes, but this is not the case with a squeezed state.

As expected from the nature of the optomechanical coupling, the output quadrature receiving the highest contribution from mechanical noise (3^{rd} line in Equation (3.18)) is the output phase quadrature, i.e. $\theta = \pi/2$. However this does not necessarily imply that

measurements of mechanical noise performed on the output phase quadrature are the most sensitive as noise contributions from the input and loss port may cover mechanically induced phase fluctuations. In the next section we will determine the limits in sensitivity of mechanical displacement fluctuation measurements.

Note that in the absence of optomechanical coupling, the constant Z_{rp} equals zero, and all mechanical contributions to the output fluctuations vanish. As a result, Equation (3.18) reduces to the description of a linear cavity connected to an input, output, and loss channels.

3.2 Theoretical limits on continuous displacement sensing

In experimental optomechanics, the optical degree of freedom of the optomechanical system is commonly employed as a meter for measuring mechanical displacements. As we saw in Section 2.2, mechanical displacements are represented by variations in the scalar position of a harmonic oscillator subjected to damping and forces from its environment. Therefore optical measurements of mechanical motion also provide information about physical systems that are dynamically coupled to the mechanical degree of freedom of the optomechanical system. Thanks to advances in micro- and nanofabrication techniques, mechanical resonators can be engineered to achieve efficient coupling with a broad range of physical systems, thereby allowing measurements on a wide variety of physical quantities, such as electron and nuclear spins [84, 96, 97], radio wave signals [34], attonewton-scale forces [98, 99], and atomic-scale masses [100]. The fundamental sensitivity limit of a measurement of the aforementioned physical quantities via mechanical displacement sensing is imposed by the zero-point energy of the mechanical oscillator. If the variance of the mechanical displacement induced by the environment is smaller than the zero-point motion of the mechanical oscillator, then the effect of the environment on the oscillator will be buried under mechanical quantum noise. That being said, the optical measurement of mechanical displacements is itself limited by optical quantum noise which has prevented the observation of the zero-point motion in real experiments so far. In this section we investigate the limit of mechanical displacement sensing imposed by fluctuations in the fields coupled to the optomechanical system.

3.2.1 The standard quantum limit in interferometric measurements

The fluctuations in an arbitrary quadrature of the output field defined by Equation (3.15) can be observed via an interferometric measurement, with an homodyne detector for example. A canonical example of interferometric measurement consists of measuring a relative phase difference between the two arms of a Mach-Zehnder interferometer, as depicted on Figure 3.1. A single optical mode is split in two at a beam splitter, and

later recombined at a second beam splitter after a phase shift ϕ has been applied in one of the arms. A simple analysis of the fluctuations in the photon number measured at one output of the second beam splitter reveals the nature of the sensitivity limits of the interferometric phase measurement [20]. The mean number of photon measured at one output of the second beam splitter during a time τ, with a photodetector depends on the relative phase between the two arms of the interferometer, and is given by

$$\bar{n}_2 = \langle \hat{n}_2 \rangle = \langle \hat{s}_2^\dagger \hat{s}_2 \rangle \tau = \bar{n}_{in} \sin^2(\phi/2) \ , \tag{3.20}$$

with $\bar{n}_{in} = \langle \hat{s}_{in}^\dagger \hat{s}_{in} \rangle \tau$ the mean number of photon sent at the input of the interferometer during a time τ. Here we have arbitrarily chosen to look at the second output of the beam splitter but the analysis is analog for the first output. As we are investigating limits in measurement sensitivity it is reasonable to consider the measured quantity as a small deviation of the phase, $\delta\phi \ll \pi$. It induces a change in the measured number of photons at the photodetector given by

$$\delta\bar{n}_2 = \delta\phi \frac{\partial \bar{n}_2}{\partial \phi} \approx \frac{\delta\phi}{2} \sin(\phi) \bar{n}_{in} \ , \tag{3.21}$$

The signal measured by the photodetector must be compared to the noise of the measurement in the form of the *signal to noise ratio* (SNR),

$$\mathrm{SNR} = \frac{(\delta\bar{n}_2)^2}{\mathrm{Var}(\hat{n}_2)} = \frac{\sin^2(\phi)}{\sin^2(\phi/2)} \frac{\delta\phi^2}{4} \bar{n}_{in} \ . \tag{3.22}$$

Here we considered only the optical quantum noise, i.e. the variance of the photon number fluctuations at the photodetector, which we further assume to follow a Poisson distribution, i.e $\mathrm{Var}(\hat{n}_2) = \bar{n}_2$, corresponding to a coherent state of light. In this case the minimum detectable phase variation, obtained for $\mathrm{SNR} = 1$, is given by

$$\delta\phi_{imp} = \frac{1}{\sqrt{\bar{n}_{in}}} \ , \tag{3.23}$$

and is referred to as the *imprecision noise limit*.

It appears that the imprecision noise can be arbitrarily reduced by increasing the input number of photon, either by increasing the power in the input beam or by lengthening the measurement time. That is obviously not a complete description of the interferometer noise limit, or otherwise the Heisenberg uncertainty principle would be violated. Indeed we must consider the noise induced by fluctuations in the position of the interferometer mirrors [7]. Due to the radiation pressure force exerted by the light beam reflected off a mirror, the mirror position fluctuates on a length scale proportional to the power fluctuations in the reflected beam. The uncertainty in the mirrors' position translates into an additional noise limit in the interferometric phase measurement, which

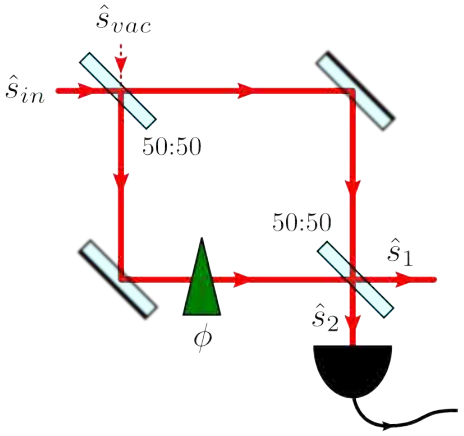

FIGURE 3.1: Quantum model of a balanced interferometer. An optical input beam, $\hat{s}_{in}$, is split equally into the two arms of a Mach-Zehnder interferometer by a 50:50 beam splitter. Vacuum noise enters the interferometer through the unused port of the beam splitter. A phase shift ϕ is applied to the optical beam in one arm of the interferometer. After propagating through the arms of the interferometer, the split beams are recombined on a 50:50 beam splitter. Due to interferences between the two beams, the powers at the outputs of the second beam splitter are dependent on the relative phase between the two arms of the interferometer, thereby enabling the detection of phase variations by recording one output of the beam splitter with a photodetector.

increases with the square-root of the input photon number variance for a measurement time τ, resulting in

$$\delta\phi_{qba} \propto \sqrt{\bar{n}_{in}} \, . \tag{3.24}$$

This radiation pressure noise is referred to as the *quantum backaction* (QBA) *noise limit*, and it counterbalances the imprecision noise at high photon number. The sum of the QBA noise and the imprecision noise reaches a minimum for a specific input number of photon which depends on the characteristic of the interferometer and the signal to be measured. This minimum is the so-called *standard quantum limit* (SQL),

$$\delta\phi_{sql} = \min_{\bar{n}_{in}}(\delta\phi_{imp} + \delta\phi_{qba}) \tag{3.25}$$

3.2.2 Imprecision and backaction noise in cavity optomechanics

Expanding on the preceding definitions of the fundamental quantum noise limits for an interferometric phase measurement, we may define the imprecision noise as the fundamental quantum noise introduced by the meter in the measurement, and the QBA noise as the noise imparted onto the measured quantity via the interaction with the meter. Applying these definitions to the measurement of mechanical displacements represented

by Equation (3.18), the imprecision noise corresponds to the spectral variance

$$\langle|\delta\hat{\chi}_{imp}|^2\rangle = \frac{\hbar(1-Z_c)}{Z_cZ_{rp}}\left[\cot^2(\theta)\langle|\delta\hat{\mathcal{X}}_{in}|^2\rangle + \langle|\delta\hat{\mathcal{P}}_{in}|^2\rangle + \cot(\theta)\langle\delta\hat{\mathcal{X}}_{in}\delta\hat{\mathcal{P}}_{in} + \delta\hat{\mathcal{P}}_{in}\delta\hat{\mathcal{X}}_{in}\rangle\right] + \frac{\hbar}{Z_{rp}}\left[\cot^2(\theta)\langle|\delta\hat{\mathcal{X}}'_{loss}|^2\rangle + \langle|\delta\hat{\mathcal{P}}'_{loss}|^2\rangle + \cot(\theta)\langle\delta\hat{\mathcal{X}}'_{loss}\delta\hat{\mathcal{P}}'_{loss} + \delta\hat{\mathcal{P}}'_{loss}\delta\hat{\mathcal{X}}'_{loss}\rangle\right] . \tag{3.26}$$

As the measured quadrature tends to the amplitude quadrature of the output field ($\theta \to 0$) the imprecision noise diverges to infinity, what can be explained by the fact that the amplitude quadrature carries no information on the mechanical displacement fluctuations, and consists only of quadrature noise from the optical fields entering the cavity. On the other hand, in the case of uncorrelated amplitude and phase quadratures, the minimum imprecision noise is achieved for a measurement of the output phase quadrature ($\theta = \pi/2$), which is the most sensitive to mechanical displacement fluctuations.

Now considering the mechanical displacement fluctuations driven by the optical field fluctuations entering the cavity, we can separate the remaining terms in Equation (3.18) into two contributions to the spectral variance. One which is purely due to the QBA noise, and will be referred as such,

$$\langle|\delta\hat{\chi}_{qba}|^2\rangle = \hbar Z_cZ_{rp}|\chi_m|^2\langle|\delta\hat{\mathcal{X}}_{in}|^2\rangle + \hbar Z_{rp}|\bar{\chi}_o\chi_m|^2\langle|\delta\hat{\mathcal{X}}'_{loss}|^2\rangle , \tag{3.27}$$

and another which results from correlations between the optical field quadrature fluctuations and the transduced mechanical displacement fluctuations driven by radiation-pressure noise,

$$\begin{aligned}\langle|\delta\hat{\chi}_{corr}|^2\rangle = {} & 2\hbar\,\mathrm{Re}\left[(1-\bar{\chi}_o)\chi_m\right]\cot(\theta)\langle|\delta\hat{\mathcal{X}}_{in}|^2\rangle + 2\hbar\,\mathrm{Re}\left[\bar{\chi}_o\chi_m\right]\cot(\theta)\langle|\delta\hat{\mathcal{X}}'_{loss}|^2\rangle \\ & + \hbar\left(1-\mathrm{Re}[\bar{\chi}_o\chi_m]\right)\langle\delta\hat{\mathcal{X}}_{in}\delta\hat{\mathcal{P}}_{in} + \delta\hat{\mathcal{P}}_{in}\delta\hat{\mathcal{X}}_{in}\rangle \\ & + \hbar\,\mathrm{Re}[\bar{\chi}_o\chi_m]\langle\delta\hat{\mathcal{X}}'_{loss}\delta\hat{\mathcal{P}}'_{loss} + \delta\hat{\mathcal{P}}'_{loss}\delta\hat{\mathcal{X}}'_{loss}\rangle .\end{aligned} \tag{3.28}$$

As expected the QBA noise scales proportionally with the radiation-pressure transduction strength $\hbar Z_{rp} = 8\eta(1-\eta)(\hbar g/\kappa_c)^2\bar{s}_{in}^2$. while the imprecision noise scales inversely.

3.2.3 The standard quantum limit in cavity optomechanics

The strongest signal induced by mechanical oscillations is observed for a measurement of the phase quadrature fluctuations of the output field ($\theta = \pi/2$), therefore it is reasonable to first consider the sensitivity of mechanical displacement sensing for such a measurement. We further assume that the amplitude and phase quadratures of the fields entering the input and loss ports of the cavity are uncorrelated. Under these conditions,

the imprecision and QBA noise simplify to

$$\langle|\delta\hat{\chi}_{imp}|^2\rangle = \frac{\hbar|\chi_m|}{\sqrt{\eta}\mathcal{P}}\left[\langle|\delta\hat{\mathcal{P}}_{in}|^2\rangle + Z_c\left(\langle|\delta\hat{\mathcal{P}}'_{loss}|^2\rangle - \langle|\delta\hat{\mathcal{P}}_{in}|^2\rangle\right)\right] , \tag{3.29}$$

$$\langle|\delta\hat{\chi}_{qba}|^2\rangle = \frac{\hbar|\chi_m|\mathcal{P}}{\sqrt{\eta}}\left[\langle|\delta\hat{\mathcal{X}}_{in}|^2\rangle + (1-\eta)\left(\langle|\delta\hat{\mathcal{X}}'_{loss}|^2\rangle - \langle|\delta\hat{\mathcal{X}}_{in}|^2\rangle\right)\right] , \tag{3.30}$$

while the contribution from the output quadrature correlated noise vanishes, $\langle|\delta\hat{\chi}_{corr}|^2\rangle = 0$. In the equations above we have introduce a dimensionless parameter, refereed to as the normalized power,

$$\mathcal{P}(\Omega) = \frac{Z_c Z_{rp}|\chi_m|}{\sqrt{\eta}} = 64\frac{\eta^{3/2}(1-\eta)^2}{1+\bar{\Omega}^2}\frac{g_0^2}{\kappa_c^2}\frac{P_{in}}{\hbar\omega_d}\sqrt{\frac{\Omega_m^2}{(\Omega_m^2-\Omega^2)^2+\Omega^2\Gamma_m^2}} , \tag{3.31}$$

which highlights the inverse scaling of imprecision and QBA noise, and follows a linear dependence on the input power P_{in} and a quadratic dependence on the vacuum optomechanical coupling parameter g_0.

The SQL corresponds to the minimum measurement noise achievable with quantum noise limited resources, which means that the field fluctuations entering the system are equivalent to vacuum noise. In addition, the linearization of the QLE governing the cavity optomechanical system dynamics (cf. 2.3.5) requires the cavity to be driven by a bright field, thus the input field must be in a bright coherent state while the loss port can be filled with a vacuum state, with the respective spectral variances, $\langle|\delta\hat{\mathcal{X}}_{in}|^2\rangle = \langle|\delta\hat{\mathcal{P}}_{in}|^2\rangle = 1/2$, and $\langle|\delta\hat{\mathcal{X}}'_{loss}|^2\rangle = \langle|\delta\hat{\mathcal{P}}'_{loss}|^2\rangle = 1/2$. After substitution of the spectral variances of the field fluctuations in Equations (3.29) and (3.30), the sum of imprecision and QBA noise at a given measurement frequency Ω_{meas} reaches a minimum for a value of the dimensionless parameter $\mathcal{P}(\Omega_{meas}) = 1$. Therefore the SQL for a measurement of the mechanical oscillations, at a frequency $\Omega_{meas} = \Omega_m$, reads

$$\langle|\delta\hat{\chi}_{sql}(\Omega_m)|^2\rangle = \frac{2x_{zpf}^2}{\sqrt{\eta}\Gamma_m} . \tag{3.32}$$

The SQL is minimum in the limit of high overcoupling, $\eta \to 1$, because, in this regime, almost all of the intracavity field sensing the mechanical oscillations is coupled to the output field of the cavity and thereby increases the measurement signal. Recalling Equation 2.26 we notice that the SQL is then equal to the spectral variance of the mechanical oscillator in its ground state,

$$\lim_{T\to 0}\langle|\delta\hat{\chi}(\Omega_m)|^2\rangle = 2x_{zpf}^2\Gamma_m . \tag{3.33}$$

The SQL is equivalent to the Heisenberg uncertainty principle for continuous linear

measurements [8]. Indeed the non-commutativity of the amplitude and phase quadratures of the input field imposes the following inequality on the imprecision noise and the radiation-pressure backation force fluctuations,

$$\langle|\delta\hat{\chi}_{imp}|^2\rangle\langle|\delta\hat{\mathcal{F}}_{qba}|^2\rangle = |\chi_m|^{-2}\langle|\delta\hat{\chi}_{imp}|^2\rangle\langle|\delta\hat{\chi}_{qba}|^2\rangle = \frac{\hbar^2}{4\eta} \geq \frac{\hbar^2}{4} \ , \tag{3.34}$$

which saturates in the limit of high overcoupling.

The input optical power required to achieve a measurement sensitivity at the SQL is obtained from Equation (3.31) by setting $\mathcal{P}(\Omega_m) = 1$, resulting in

$$P_{sql} = \eta^{-3/2}\frac{1+\bar{\Omega}_m^2}{\bar{\Omega}_m^2}P_{min} \ , \tag{3.35}$$

where $\bar{\Omega}_m = 2\Omega_m/\kappa = 2(1-\eta)\Omega_m/\kappa_c$ is the sideband resolution parameter, comparing the mechanical resonance frequency with the cavity width. Furthermore, we have introduced the minimum input power at which a sensitivity at the SQL can be achieved with quantum noise limited resources, defined by

$$\frac{P_{min}}{\hbar\omega_d} = \frac{\Gamma_m\Omega_m^2}{16g_0^2} \ . \tag{3.36}$$

Reaching the SQL at this input power requires a highly overcoupled cavity optomechanical system in the resolved sideband regime, i.e. $\eta \to 1$ and $\bar{\Omega}_m \gg 1$. However there exists a trade-off between these requirements as the width of the cavity increases with the coupling parameter, thereby reducing the sideband resolution. Figure 3.2 illustrates the ratio of the power required to reach the SQL with the minimum theoretical power, as a function of the optical coupling parameter η and the intrinsic sideband resolution parameter Ω_m/κ_c.

In order to get a clear idea of the nature of the imprecision noise and the QBA noise it is interesting to look at the total uncertainty on the displacement measurement as a function of optical input power and sideband frequency, which is given by

$$\begin{aligned}\langle|\delta\hat{\chi}_{tot}(\Omega)|^2\rangle &= \frac{\langle|\delta\hat{\chi}_{sql}(\Omega_m)|^2\rangle}{2}\left[\frac{1+\bar{\Omega}^2}{1+\bar{\Omega}_m^2}\frac{P_{sql}}{P_{in}} + \frac{|\chi_m(\Omega)|^2}{|\chi_m(\Omega_m)|^2}\frac{1+\bar{\Omega}_m^2}{1+\bar{\Omega}^2}\frac{P_{in}}{P_{sql}}\right] \ , \\ &\approx \frac{\langle|\delta\hat{\chi}_{sql}(\Omega_m)|^2\rangle}{2}\left[\frac{P_{sql}}{P_{in}} + \frac{(\Gamma_m/2)^2}{(\Omega_m-\Omega)^2+(\Gamma_m/2)^2}\frac{P_{in}}{P_{sql}}\right] \ ,\end{aligned} \tag{3.37}$$

and shown on Figure 3.3. To simplify the expression we assumed $\kappa^2 \gg \Omega_m\Gamma_m$, which is a less stringent condition than the resolved sideband regime, usually fulfilled by cavity optomechanical systems. Imprecision noise clearly dominates over QBA noise for low input optical power, $P_{in} < P_{sql}$. Inversely the QBA noise surpasses the imprecision noise at high optical power, $P_{in} > P_{sql}$, but only within the resonance of the mechanical

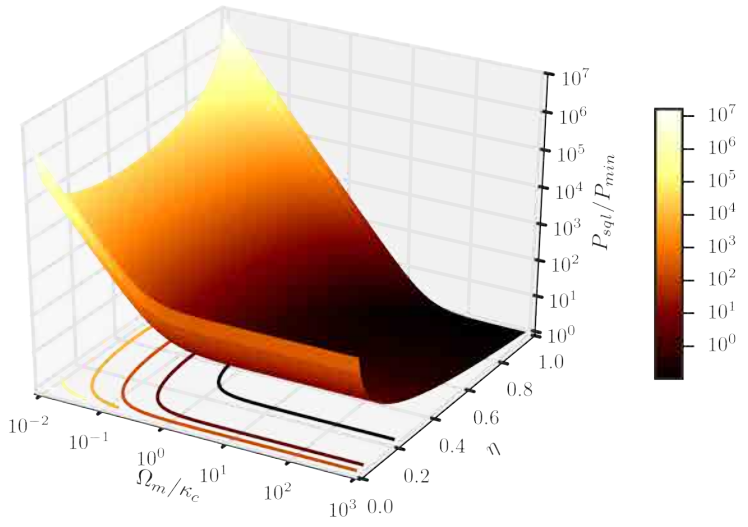

FIGURE 3.2: Optical input power required to achieve sensitivities of mechanical displacement measurements at the SQL, normalized to the minimum required power $P_{min} = \Gamma_m \Omega_m^2 / 32 g_0^2$. For an optomechanical system in the bad cavity regime, $\Omega_m/\kappa_c \ll 1$, the required input power is several order of magnitudes higher than for a system in the resolved sideband regime, $\Omega_m/\kappa_c \gg 1$.

oscillator. Away from the mechanical resonance the noise level remains limited by shot noise from the optical probe field.

Considerations over the optical power necessary to achieve high-sensitivity in mechanical displacement measurements are essentials in experiments where the use of high optical power is limited by technical reasons, e.g. the maximum output power of existing lasers, or practical reasons, e.g. the damage threshold of biological samples. For a continuous measurement with a coherent probe, high-sensitivities with low probe powers are better achieved with an optomechanical system in the resolved sideband regime. The optimization of an optomechanical system with the view to achieve high-sensitivity displacement sensing requires a reduction of optical and mechanical loss, as well as a strengthening of the optomechanical interaction. Table 3.1 lists the experimental parameters of a few cavity optomechanical systems, and compares the optical probe power required for a measurement at the SQL.

3.2.4 Squeezing-enhanced measurements

With a growing interest in high-sensitivity measurements of mechanical displacement motivated by the quest for the detection of gravitational waves in large-scale interferometers, it was soon recognized that the use of squeezed light as a quantum sensing resource could improve the sensitivity of interferometric phase measurements beyond

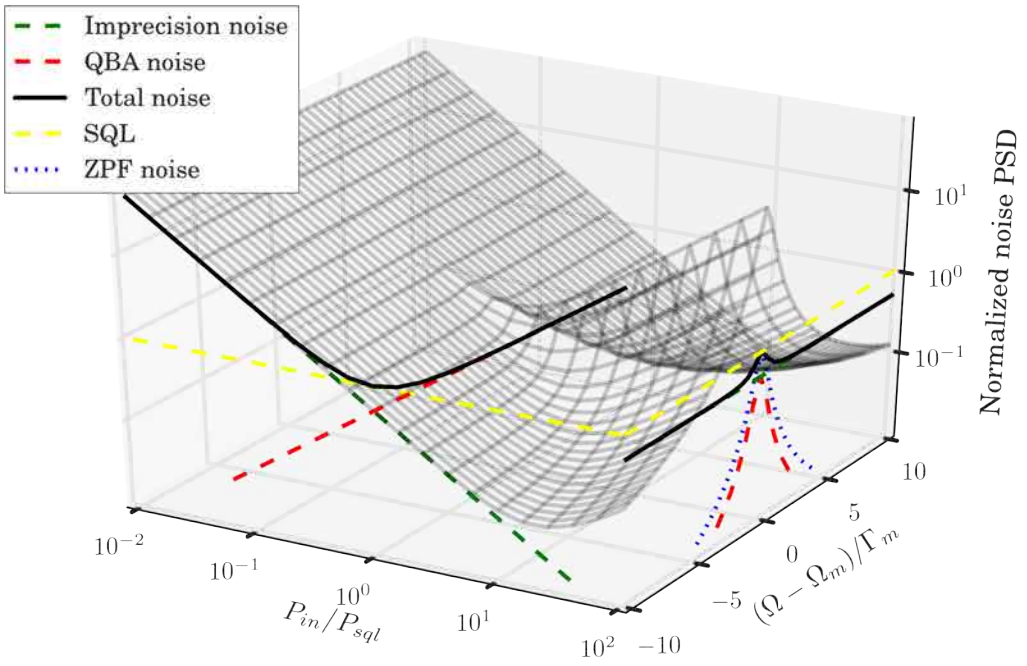

FIGURE 3.3: Noise PSD normalized to the SQL. The black wireframe indicates the total noise PSD, which is the sum of the imprecision noise and the QBA noise, as a function of the normalized input power P_{in}/P_{sql} and the normalized frequency detuning from the mechanical resonance $(\Omega - \Omega_m)/\Gamma_m$. The total noise PSD at the mechanical resonance frequency Ω_m is plotted as a function of normalized input power (black), along with the imprecision noise (dashed green), the QBA noise (dashed red), and the SQL (dashed yellow). Similarly the total noise PSD at $P_{in} = P_{sql}$ is shown on the frequency axis. The blue dotted curve represents the PSD of the zero-point fluctuations of the mechanical oscillator in its ground state. All PSD are normalized to the SQL.

the shot noise limit set by optical powers of available continuous-wave lasers [83]. Experimental demonstrations of squeezing-enhanced interferometric measurements were later performed with Mach-Zehnder [90], Michelson [91–93], Sagnac [94], and large-scale gravitational-wave interferometers [95], followed by applications to displacement measurements [101] of particles in biological samples [86].

The use of squeezed light in optical interferometric measurements enables an improvement of the measurement sensitivity in the form of a reduction of the measured optical field fluctuations. By an appropriate choice of the squeezed quadrature of the optical field, the imprecision noise limit of the measurement can be lowered, thereby increasing the signal-to-noise ratio. The reduction of the imprecision noise can be understood by recalling the sideband model of Subsection 1.2.5, where quantum noise arises upon detection, from the beating of randomly fluctuating sidebands with a bright carrier. From Equation (1.55) the spectral variance of a phase quadrature measurement ($\phi_\alpha = \pi/2$) in terms of upper and lower sideband quadrature fluctuations, and excluding

References	This thesis	[37]	[39]	[33]	[89]
λ_d [nm]	1064	1537	780	1064	1540
$\kappa/2\pi$ [Hz]	1.84e+08	5.00e+08	7.10e+06	8.90e+05	3.42e+09
$\Omega_m/2\pi$ [Hz]	5.48e+06	3.68e+09	7.80e+07	1.55e+06	2.80e+07
$\Gamma_m/2\pi$ [Hz]	1.00e+04	3.50e+04	8.10e+03	1.43e+03	1.72e+02
$g_0/2\pi$ [Hz]	3.00e+01	9.10e+05	3.40e+03	1.61e+01	7.50e+05
Ω_m/κ	3.0e-02	7.4e+00	1.1e+01	1.7e+00	8.2e-03
P_{min} [W]	2.4e-05	2.9e-08	4.3e-07	9.7e-07	1.2e-14
P_{sql} ($\eta = 1/2$) [W]	7.8e-02	8.4e-08	1.2e-06	3.7e-06	5.1e-10

TABLE 3.1: Experimental parameters and calculated optical probe power for measurements at the SQL in various optomechanical systems. As the coupling parameter is not always clearly stated in the references, we assumed the system to be in the critical coupling regime ($\eta = 1/2$) for the calculation of P_{sql}.

all classical noise from the detection apparatus, is given by

$$\langle|\delta\hat{\mathcal{P}}(\Omega)|^2\rangle = \frac{1}{4}\left[\langle\delta\hat{P}_+^2\rangle + \langle\delta\hat{P}_-^2\rangle + \langle\delta\hat{X}_+^2\rangle + \langle\delta\hat{X}_-^2\rangle + 2\langle\delta\hat{P}_+\delta\hat{P}_-\rangle - 2\langle\delta\hat{X}_+\delta\hat{X}_-\rangle\right] . \tag{3.38}$$

For a coherent optical field, the sidebands are uncorrelated and in vacuum states with quadrature variances equal to 1/2. Therefore the phase quadrature measurement is quantum noise limited with a noise spectral variance at the shot noise level, i.e. $\langle|\delta\hat{\mathcal{P}}(\Omega)|^2\rangle = 1/2$. The effect of squeezed light on the detection noise lies in the covariance terms of Equation (3.38). Correlations between upper and lower sideband quadrature fluctuations can be introduced such that both covariance terms subtract to the total sum, thereby bringing the measurement imprecision noise below the shot noise level, i.e. $\langle|\delta\hat{\mathcal{P}}(\Omega)|^2\rangle < 1/2$. In the case of a phase measurement, the maximum noise reduction is achieved when the sidebands are in a phase squeezed vacuum state, which implies that the phase quadrature fluctuations of the upper and lower sidebands are correlated, $\langle\delta\hat{P}_+\delta\hat{P}_-\rangle < 0$, while their amplitude quadrature fluctuations are anti-correlated, $\langle\delta\hat{X}_+\delta\hat{X}_-\rangle > 0$.

Phase quadrature squeezed input field

From 1.2.7 we recall the amplitude and phase quadrature variances of a pure phase squeezed state,

$$\langle|\delta\hat{\mathcal{X}}(\Omega)|^2\rangle = \frac{1}{2}e^{2r} , \qquad \langle|\delta\hat{\mathcal{P}}(\Omega)|^2\rangle = \frac{1}{2}e^{-2r} , \tag{3.39}$$

where $r \geq 0$ is the squeezing parameter. Injecting a bright phase squeezed state at the input port of the cavity leads to an overall reduction of the imprecision noise (cf. Equation (3.29)), to the detriment of an increase in QBA noise due to the anti-squeezed

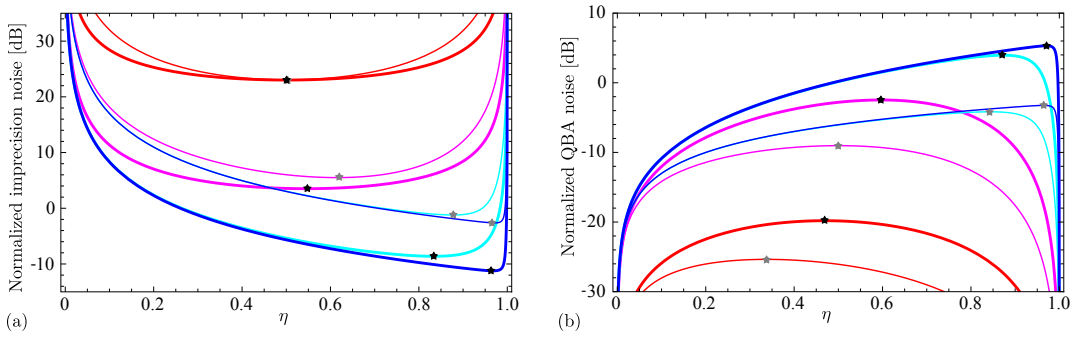

FIGURE 3.4: Imprecision noise (a) and QBA noise (b) at the mechanical sideband as a function of the cavity coupling parameter $\eta = \kappa_{ex}/\kappa$. Noise levels are normalized to the SQL. Thin and thick traces indicate noise levels for measurements with a coherent and phase squeezed input field, respectively, with input power P_{min}, and at various degrees of intrinsic sideband resolution, $\Omega_m/\kappa_c = 0.1$(red), 1 (magenta), 10 (cyan), and 100 (blue). Phase squeezed vacuum states with 8.7 dB reduced variance at the mechanical sidebands are used as a quantum-enhanced sensing resources. Gray and black stars indicate the extrema of the thin and thick traces, respectively, which correspond to the minimum of the imprecision noise in (a), and the maximum of the QBA noise in (b).

amplitude quadrature of the input field (cf. Equation (3.30)). The imprecision noise and the QBA noise at the mechanical sideband frequency Ω_m are shown on Figures 3.4(a) and 3.4(b) for both a bright coherent and phase squeezed input field with power P_{min}. The noise PSD is normalized to the SQL, and plotted as a function of the cavity coupling parameter, $\eta = \kappa_{ex}\kappa$, for various degrees of intrinsic sideband resolution, Ω_m/κ_c. The squeezing parameter is arbitrarily chosen equal to unity, which yields a reduction of the input phase quadrature fluctuations of 8.7 dB compared to a coherent state, well within reach of current technology [94]. As indicated by the gray and black stars on Figure 3.4(a), the minimum achievable imprecision noise at a fixed input power with both a coherent and phase squeezed input field decreases when the resolution of the mechanical sideband increases. The inverse trend is observed for the maximum QBA noise on Figure 3.4(b). This behavior can be explained by an increase of the power circulating in the cavity induced by a reduction of the intrinsic cavity loss, and leading to an improvement of the mechanical noise transduction.

Figure 3.4 highlights the difference between the resolved sideband regime ($\Omega_m/\kappa_c > 1$) and the unresolved sideband regime ($\Omega_m/\kappa_c < 1$). In the later case phase squeezing of the input field fluctuations yields a limited improvement in measurement sensitivity as intrinsic cavity loss damages squeezed states at sideband frequencies within the cavity width. In particular when the cavity is critically coupled ($\eta = 1/2$) and in the limit $\Omega_m \ll \kappa$, all input field fluctuations entering the cavity pass through the cavity and leave through the loss port, while fluctuations that enter the cavity via the loss port couple through the cavity to the output field. Therefore squeezing the input field fluctuations

yields no improvement of the measurement sensitivity in this regime.

Optimum squeezing-enhanced imprecision noise reduction is achieved in the regime of negligible intrinsic cavity loss rate compared to both the optical cavity coupling rate and mechanical resonance frequency, i.e. $\kappa_c \ll \kappa_{ex},\ \Omega_m$, where the squeezed mechanical sidebands lie far out of the cavity resonance and are therefore little affected by the cavity loss. Unfortunately, this regime also corresponds to a maximum QBA noise that compensates the reduction of imprecision noise, thereby preventing the measurement sensitivity to beat the SQL.

Figure 3.5 shows the total displacement measurement uncertainty at the mechanical sideband frequency Ω_m as a function of the optical input power and degree of phase squeezing. The cavity optomechanical system is set in the overcoupled regime with $\eta = 0.8$, and in the resolved sideband regime with $\Omega_m/\kappa_c = 22$ [39], which are favorable and experimentally reasonable conditions for the enhancement of measurement sensitivity with squeezed light. Strong squeezing of the input phase quadrature fluctuations gives access to measurement sensitivities close to the SQL at low powers with minimum noise levels achieved near the line parametrized by, $P_{in} = 2P_{sql}\langle|\delta\hat{\mathcal{P}}_{in}|^2\rangle$, as expected from Equations (3.29) and (3.30). However, due to non-zero intrinsic cavity loss, the QBA noise and imprecision noise are unbalanced for high degrees of squeezing, what degrades the measurement sensitivity. As a result squeezing enhances the measurement sensitivity at a given power, but the optimum measurement sensitivity achievable is lower than one at a higher power.

Considerations for experimental implementations

The primary requirement on the experimental implementation of squeezing-enhanced measurements is the availability of squeezed vacuum states at the mechanical sideband frequency. Indeed the observation of squeezed states is currently technically limited to sideband frequencies from kilohertz to gigahertz [102, 103], with the strongest squeezing typically obtained in the megahertz to tens of megahertz range [94, 104], where the sidebands are little affected by low frequency classical noise modulating the amplitude and phase of the carrier, but still satisfying the mode matching conditions imposed by squeezing source devices. These restrictions on the squeezing bandwidth limit the choice of mechanical resonator with which to perform quantum-enhanced displacement measurements. For example, optomechanical crystals [36, 37] sustain mechanical modes at gigahertz frequencies that lie outside of the bandwidth of current squeezing sources, and are therefore not suitable although they operate far into the resolved sideband regime. On the other hand, WGM resonators [39, 105] display mechanical resonances at lower frequencies (1-100 MHz) that can be probed with significant quantum noise reduction ($\sim$5 dB at 100 MHz [103, 104]), while being sideband resolved.

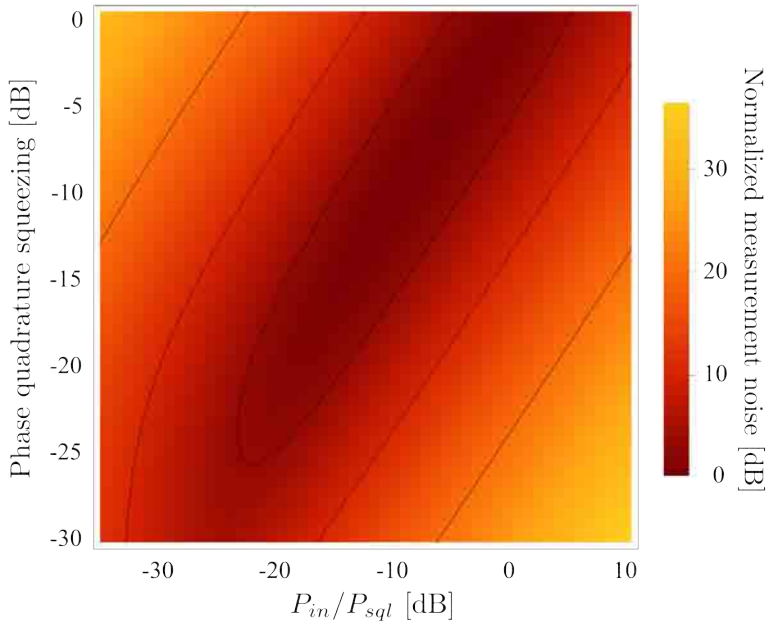

FIGURE 3.5: Total quantum noise for a displacement measurement in the overcoupled and resolved sideband regime ($\eta = 0.8$ and $\Omega_m/\kappa_c = 22$) as a function of input power and squeezing degree. The measurement noise is normalized to the SQL. Black contours indicate 3 dB, 10 dB and 20 dB of quantum noise above the SQL.

Considering the cavity optomechanical system in [39] (cf. Table 3.1), its mechanical resonance at 78 MHz, corresponding to the radial breathing mode of a WGM resonator, can be probed by a bright phase squeezed input field with a phase noise reduction of 6 dB at the mechanical sideband, provided by the squeezing source in [104]. Figure 3.6 shows the sum of the imprecision and QB noise for displacement measurements with both a

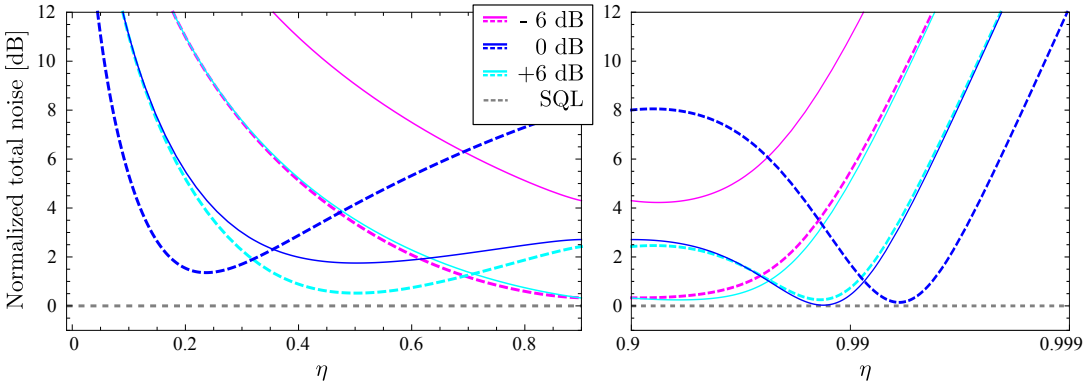

FIGURE 3.6: Total quantum noise for a displacement measurement using coherent (solid lines) and phase squeezed (dashed lines) input fields at powers -6 dB (magenta), 0 dB (cyan), and +6 dB (blue) over P_{min}. Phase squeezed vacuum states at the mechanical sidebands display a 6 dB reduction of noise variance, and are assumed to be pure. The cavity optomechanical system is in the resolved sideband regime with $\Omega_m/\kappa_c = 22$. The measurement noise is normalized to the SQL which is indicated by the gray dashed line.

coherent input field and a phase squeezed intput field, and for various probe powers below and above P_{min}. The minimum optical power required to reach displacement measurement sensitivities at the SQL with a coherent input field at a carrier wavelength of 1064 nm is $P_{min} = 590$ nW. In the case of a squeezing-enhanced measurement, the degree of anti-squeezing is assumed equal to the degree of squeezing for simplicity. For impure phase squeezed vacuum states at the mechanical sideband, the excess QBA noise prevents reaching sensitivities at the SQL.

We see from Figure 3.6 that the measurement sensitivity increases with the input power until the SQL is approached for $P_{in} = P_{min}$. This behavior is expected since the QBA noise is negligible compared to the imprecision noise for low input powers below P_{min}, therefore the total noise variance follows the $1/P_{in}$ dependence of the imprecision noise (cf. Equation 3.29).

For measurements at input powers above P_{min}, the QBA noise is no longer negligible and overcomes the imprecision noise, which leads to an increase in the noise variance proportional to the input power. However, due to the the near zero transduction of mechanical displacements onto the output phase quadrature in the limit of under- and overcoupling, i.e. $\eta \to 0,\ 1$, there exists two values of the cavity coupling parameter at which the imprecision noise and the QBA noise are balanced, thus the total measurement noise is minimum and near the SQL. One value corresponds to the limit of the overcoupled regime ($\eta \to 1$) and provides the best measurement sensitivity, but it is challenging to reach experimentally [61]. The second value yields a slightly lower measurement sensitivity but corresponds to less demanding experimental conditions.

With a cavity optomechanical system in the resolved sideband regime, probing mechanical displacements with a phase squeezed field provides an improvement of the sensitivity comparable to an increase of input power with a coherent field. For example, the measurement noise level achieved with a 6 dB reduction of the input phase noise is equivalent to the noise level reached with an increase of the input power by 6 dB. This statement holds particularly true when comparing measurement sensitivities at input power lower than P_{min}, and in the limit of strong overcoupling. However, it is more advantageous to employ a phase squeezed-input state for probing mechanical displacements in the undercoupled regime with an input power larger than P_{min}, as it gives access to measurement sensitivities near the SQL, which cannot be reached by using a coherent input field, regardless of its power.

Squeezing of the loss

So far we have considered the squeezing of the input field fluctuations, that best improves displacement measurement sensitivities in sideband resolved cavity optomechanical systems. In analogy to the interferometric phase measurement of 3.2.1, we may also consider

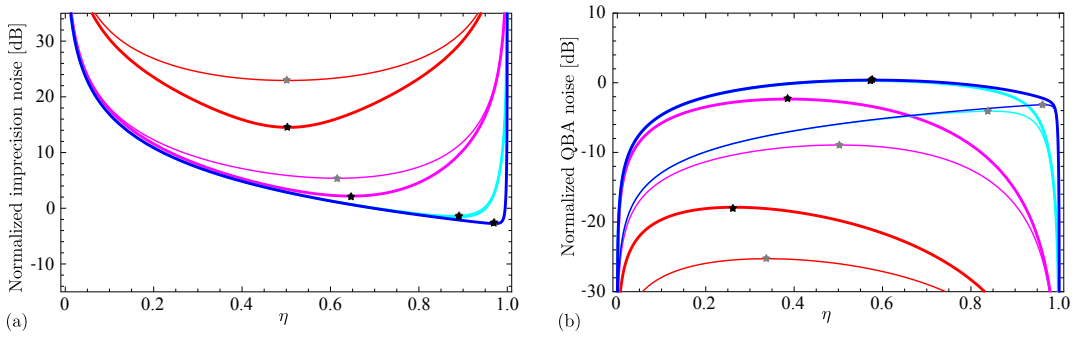

FIGURE 3.7: Imprecision noise (a) and QBA noise (b) at the mechanical sideband as a function of the cavity coupling parameter $\eta = \kappa_{ex}/\kappa$. Noise levels are normalized to the SQL. Thick and thin traces indicate noise levels for measurements with and without squeezing of the vacuum fluctuations entering the loss port, respectively. Phase squeezed vacuum states with 8.7 dB reduced variance at the mechanical sidebands are coupled to the loss port of the cavity. The mechanical displacements are probed with a coherent input field at power P_{min}, and various degrees of intrinsic sideband resolution are considered: $\Omega_m/\kappa_c = 0.1$(red), 1 (magenta), 10 (cyan), and 100 (blue). Gray and black stars indicate the extrema of the thin and thick traces, respectively, which correspond to the minimum of the imprecision noise in (a), and the maximum of the QBA noise in (b).

injecting vacuum squeezed states at sideband frequencies into the dark port rather than the bright port [83], which in the case of a cavity optomechanical system corresponds to squeezing the field fluctuations entering the cavity from the loss port.

Figure 3.7 shows the imprecision and QBA noise of a displacement measurement performed with a bright coherent input field while injecting phase squeezed vacuum states at sideband frequencies into the cavity via the loss port. Compared to displacement measurements performed with quantum noise limited resources, such a measurement provides an enhancement of sensitivity in the unresolved sideband regime, but no improvement in the resolved sideband regime. This is because the fluctuations entering through the loss port can only couple to the output field at sideband frequencies within the cavity bandwidth.

In practice it is usually not feasible to squeeze the vacuum field fluctuations coupled to the cavity via the loss port, as optical loss may be due to absorption or scattering into radiative modes that cannot be accessed. However in some particular design of optomechanical systems it is possible to control the coupling rate to an controllable optical mode such that it dominates other loss rate. In the case of a Fabry-Pérot cavity with a movable mirror (Figure 3.8(a)) the optical loss associated to the mirror's transmission can be shaped into a single propagating mode by an appropriate design and alignment of the cavity. The transmission of the mirror can then be selected such that coupling to the propagating mode dominates over other loss rates. By squeezing a matching counter-propagating field, vacuum squeezed states can be injected into the

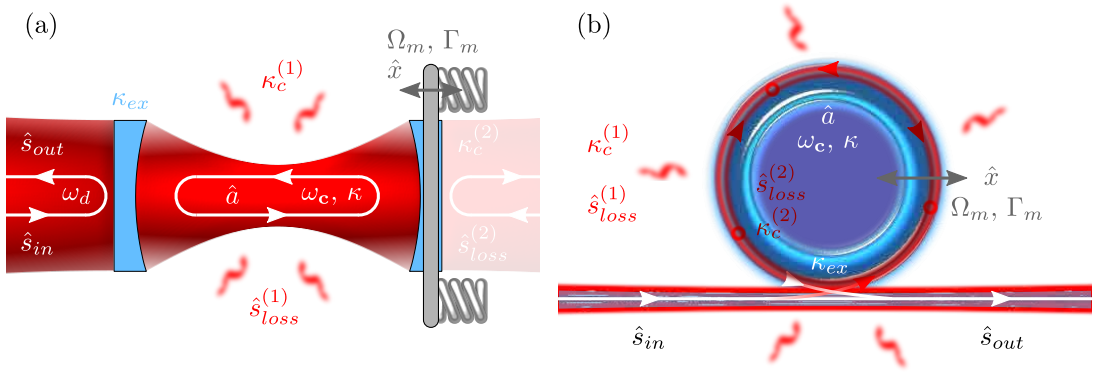

FIGURE 3.8: Fabry-Pérot (a) and WGM (b) optomechanical systems coupled to a single mode field $\hat{s}_{loss}^{(2)}$ via the loss port with decay rate $\kappa_c^{(2)}$. The coupling to remaining loss channels is represented by the coupling of the cavity field to the external field $\hat{s}_{loss}^{(1)}$ with rate $\kappa_c^{(1)}$.

cavity through the movable mirror. Similarly it is possible to couple vacuum squeezed states via the loss port in a WGM cavity by scattering of a counter-propagating mode into the forward-propagating WGM [106–108], as shown on Figure 3.8(b). By optimizing the modal coupling of the WGM cavity such that it dominates intrinsic loss rates, squeezed vacuum states can be efficiently transfered from the counter-propagating mode to the forward-propagating mode, thus enabling squeezing-enhanced displacement measurements with cavity optomechanical systems in the unresolved sideband regime.

Chapter 4

Electrical feedback cooling

In the previous chapter we have seen that optomechanical interactions give us a mean to indirectly observe the displacement of a microresonator from the mechanically-induced alteration of the noise properties of an optical probe field. Here the mechanical oscillations shape the amplitude and phase fluctuations of the light, but the optomechanical interaction also authorize the light to affect the phase and amplitude of the mechanical oscillations. This backaction has been shown to limit the sensitivity of position measurements but it may also be used to control the displacement of the microresonator. In particular, a lot of effort from the optomechanical community is being directed towards the cooling of a microresonator vibrational mode into its quantum ground state. Such an achievement would enable the study of the quantum behavior of a massive oscillator and allow experimental test of major scientific theories such as quantum gravity [3, 109]. However radiation pressure forces are inherently weak, thus a high optical power is required to achieve a significant control, what leads to detrimental heating by absorption [110, 111]. Another actuation method, extensively used with nanoelectromechanical systems [42, 112, 113], is based on electrical forces that can be orders of magnitude stronger while producing far less heat.

In this chapter we investigate the actuation and control of the mechanical mode of a microtoroid resonator with dielectric gradient forces [14, 17, 18]. We start by studying theoretically and experimentally the generation of dielectric gradient forces, and their effect on the dynamics of the microresonator. Then we include the electrical actuation scheme within a feedback loop to cool the mechanical mode.

4.1 Actuation of a microtoroid resonator

4.1.1 Dielectric gradient forces

Any dielectric body experiences a force when placed in a nonuniform electric field . Due to the presence of the electric field, electric charges within the body are slightly displaced what generates electric dipoles oriented in the direction of the electric field. In a nonuniform electric field, each pole of an electric dipole is subjected to a Coulomb force with different magnitude, thus the dipole experiences a net force directed towards higher electric field strength. Additionally, any dipole in an electric field experiences a torque which tends to bring it in alignment with the electric field.

An electrical dipole consists of two equal and opposite electrical charges $+q$ and $-q$ at positions $\vec{r}_+$ and $\vec{r}_-$, respectively, and is represented by a dipole moment $\vec{p} = q\vec{d}$, where $\vec{d} = (\vec{r}_+ - \vec{r}_-)$. The net force experienced by the dipole in the presence of a nonuniform electric field is given by [114],

$$\vec{F}_{diel} = q\vec{E}\left(\vec{r}_+\right) - q\vec{E}\left(\vec{r}_-\right), \tag{4.1}$$

which can be approximated, in the limit of small distance $|\vec{d}|$ compared to the characteristic dimension of the electric field nonuniformity, by

$$\vec{F}_{diel} = \left(\vec{p}\cdot\vec{\nabla}\right)\vec{E}. \tag{4.2}$$

In a uniform electric field, the gradient of the electric field is null, therefore no net force moves the dipole, however both charges still experience a Coulomb force that generates a torque on the dipole, given by

$$\vec{T}_{diel} = \frac{\vec{d}}{2}\times q\vec{E} + \frac{-\vec{d}}{2}\times\left(-q\vec{E}\right) = \vec{p}\times\vec{E}. \tag{4.3}$$

The above equation holds in the presence of a nonuniform electric field if the distance $\left|\vec{d}\right|$ remains small compared to the characteristic dimension of the electric field nonuniformity. The torque exists only when the electric dipole is not parallel to the electric field.

4.1.2 Dielectric gradient force actuation of a mechanical resonator

The actuation of a microresonator via dielectric forces can be achieved by placing the microresonator in an electric field gradient generated by two charged electrodes [14, 17]. The charging of the electrodes can be controlled by applying a voltage V to the electrodes such that the electrodes act as the two sides of a capacitor with capacitance C_e. We model the charging of each electrode as a point charge $q_\pm = \pm C_e V$. Gauss's law yields

the electric field generated by each point charges, at a position $\vec{r}$ in the vicinity of the electrodes,

$$\vec{E}_{\pm}(\vec{r}) = \frac{q_{\pm}}{4\pi\varepsilon_0}\frac{\vec{r}-\vec{r}_{\pm}}{|\vec{r}-\vec{r}_{\pm}|^3} = \frac{\pm C_e V}{4\pi\varepsilon_0}\vec{e}_{\pm}(\vec{r}) \ , \tag{4.4}$$

where we have introduced the vectors $\vec{e}_{\pm}(\vec{r}) = (\vec{r}-\vec{r}_{\pm}) \,/\, |\vec{r}-\vec{r}_{\pm}|^3$ which accounts for the spatial dependence of the electric field generated by each point charge. Due to the linearity of Maxwell's equation, the total electric field generated by the electrodes is given by the sum

$$\vec{E}(\vec{r}) = \vec{E}_{+}(\vec{r}) + \vec{E}_{-}(\vec{r}) \ , \tag{4.5}$$

$$= \frac{C_e V}{4\pi\varepsilon_0}\left(\vec{e}_{+}(\vec{r}) - \vec{e}_{-}(\vec{r})\right) \ . \tag{4.6}$$

We note here that the electric field diverges to infinity when the distance to the point charge shrinks to zero, what is not physical. However the formal treatment of this singularity is only relevant at scales way smaller than the scale of actual electromechanical devices.

The electric field generated by the charged electrodes polarizes the dielectric medium constituting the microresonator. The polarization of an homogeneous and isotropic dielectric medium induced by a constant electric field $\vec{E}$ is given by

$$\vec{P}_{induced} = \chi_e \varepsilon_0 \vec{E} \ , \tag{4.7}$$

where ε_0 is the vacuum permittivity and χ_e is the electric susceptibility of the medium. On top of the induced polarization the dielectric medium may present an intrinsic polarization due to trapped charges, so that the total polarization of the medium reads,

$$\vec{P}_{total} = \vec{P}_{intrinsic} + \vec{P}_{induced} \ . \tag{4.8}$$

The induced polarization is parallel to the electric field so it is not subjected to a torque (cf. Equation (4.3)). Only the trapped dipoles contributing to the intrinsic polarization of the medium experience a torque, leading to mechanical stress in the dielectric material.

Combining Equations (4.2) and (4.8), the dielectric gradient force experienced by an elementary volume of the dielectric body in a constant inhomogeneous electric field

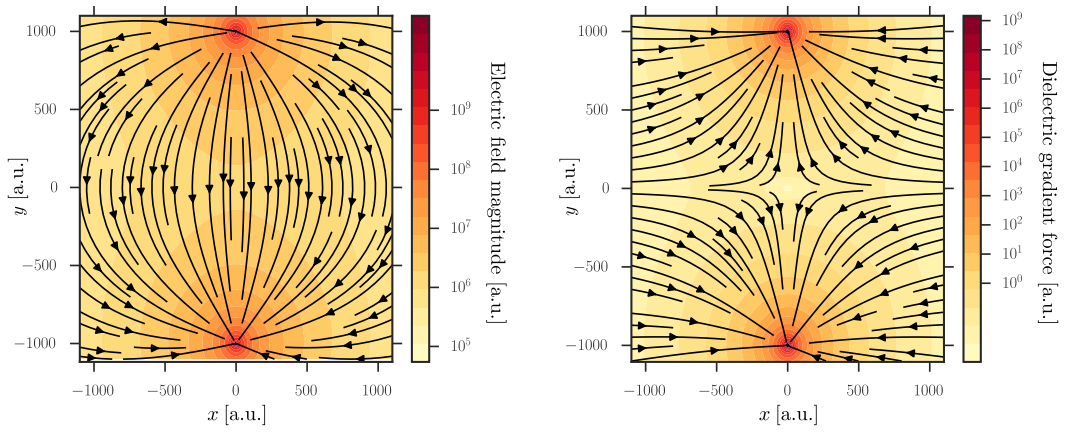

FIGURE 4.1: Electric field $\vec{E}(\vec{r})$ (left) and dielectric gradient force $\vec{\mathcal{F}}_{diel}(\vec{r})$ (right) generated by a pair of electrodes with opposite charges. The streamlines indicate the vector fields of the electric field (left) and dielectric gradient force (right). The colored contours show the magnitude of the electric field $|\vec{E}(\vec{r})|$ (left) and the magnitude of the dielectric gradient force $|\vec{\mathcal{F}}_{diel}(\vec{r})|$ (right). Here the intrinsic polarization is not taken into account in the calculation of the dielectric gradient force.

reads,

$$\vec{\mathcal{F}}_{diel}(\vec{r}) = \left(\vec{P}_{total}(\vec{r}) \cdot \vec{\nabla}\right) \vec{E}(\vec{r}) \ , \tag{4.9}$$

$$= \frac{C_e V}{4\pi\varepsilon_0} \left(\vec{P}_{intrinsic}(\vec{r}) \cdot \vec{\nabla}\right) \left(\vec{e}_+(\vec{r}) - \vec{e}_-(\vec{r})\right) + \frac{\chi_e C_e^2 V^2}{32\pi^2\varepsilon_0} \vec{\nabla} \left|\vec{e}_+(\vec{r}) - \vec{e}_-(\vec{r})\right|^2 \ , \tag{4.10}$$

where we derived the last term by using Maxwell-Faraday equation in the absence of a magnetic field, i.e. $\vec{\nabla} \times \vec{E} = \vec{0}$. Figure 4.1 shows both the electric field and the dielectric gradient force generated between two electrodes with opposite charges. Both the electric field and its gradient are more intense in the direct vicinity of the electrode point charges, and decays exponentially as the distance to the electrodes increases. This indicates that an efficient actuation scheme employing dielectric gradient forces to control the motion of a mechanical resonator requires the electrodes to be placed as close as possible to the resonator. Further tuning of the position of the electrodes may also lead to the targeted actuation of specific oscillatory modes of the mechanical resonator by matching the orientation of the dielectric gradient force with the direction of the mechanical spatial mode motion.

We note F_{diel} the scalar projection of the dielectric gradient force according to Equation (2.40). It has a linear and quadratic dependence on the voltage applied to the electrodes due to the intrinsic and induced polarization of the mechanical resonator,

respectively, and can be written,

$$F_{diel} = c_{intrinsic} V + c_{induced} V^2 \ , \tag{4.11}$$

where $c_{intrinsic}$ and $c_{induced}$ are constants.

In order to drive the oscillations of the microresonator the dielectric force is modulated by applying a weak voltage modulation on top of a constant DC voltage, resulting in the time dependent force

$$\begin{aligned} F_{diel}(t) &= F_{diel}(V_{dc} + V_{ac}(t)) \ , \\ &= F_{diel}(V_{dc}) + (c_{intrinsic} + 2c_{induced} V_{dc})\, V_{ac}(t) + c_{induced} V_{ac}(t)^2 \ . \end{aligned} \tag{4.12}$$

The first term is a time-independent force that causes a steady-state displacement of the microresonator, and does not affect the time evolution of the microresonator. The second and third terms are time dependent forces that drive the oscillations of the microresonator.

Assuming a periodic modulation of the drive voltage $V_{ac}(t)$, the dynamics of a single mechanical mode of the microresonator is best described in the frequency domain where it obeys

$$\mathcal{X}(\Omega) = \chi_m(\Omega) \mathcal{F}_{diel}(\Omega) \ , \tag{4.13}$$

with $\chi_m(\Omega)$ the mechanical susceptibility of the mode oscillator. Here we consider the dielectric force only, excluding all other forces that may drive the oscillator's motion, for simplicity. The Fourier transform of the dielectric force applied to the microresonator is given by

$$\begin{aligned} \mathcal{F}_{diel}(\Omega) = \sqrt{2\pi} F_{diel}(V_{dc}) \delta(\Omega) + (c_{intrinsic} + 2c_{induced} V_{dc})\, \mathcal{V}_{ac}(\Omega) \\ + \frac{c_{induced}}{\sqrt{2\pi}} \left(\mathcal{V}_{ac} * \mathcal{V}_{ac} \right)(\Omega) \ , \end{aligned} \tag{4.14}$$

where the first term on the right hand side is proportional to a Dirac delta function $\delta(\Omega)$, the second is proportional to the Fourier transform of the modulated drive voltage $\mathcal{V}_{ac}(\Omega)$, and the third contains the autoconvolution of the modulated drive voltage in the frequency domain.

Considering a monochromatic voltage modulation such as $V_{ac}(t) = V_{mod}\sin(\Omega_{mod}t)$, the dielectric force in the Fourier domain reads,

$$\begin{aligned}\mathcal{F}_{diel}(\Omega) = \sqrt{2\pi}\left(F_{diel}(V_{dc}) - \frac{c_{induced}V_{mod}^2}{2}\right)\delta(\Omega) \\ - i\sqrt{\frac{\pi}{2}}\left(c_{intrinsic} + 2c_{induced}V_{dc}\right)V_{mod}\left[\delta(\Omega-\Omega_{mod}) - \delta(\Omega+\Omega_{mod})\right] \\ - \frac{1}{2}\sqrt{\frac{\pi}{2}}c_{induced}V_{mod}^2\left(\delta(\Omega-2\Omega_{mod}) + \delta(\Omega+2\Omega_{mod})\right)\ ,\end{aligned} \tag{4.15}$$

and presents three frequency components. One at zero frequency, also called the DC component, consists of the constant force generated by the DC voltage (first line in Equation (4.14)) plus the mean of the dielectric force induced by the voltage modulation. The second at $\pm\Omega_{mod}$ scales linearly with both the DC voltage and the modulation voltage amplitude. The third at $\pm2\Omega_{mod}$ is independent of the DC voltage applied at the electrodes and scales quadratically with the modulation voltage amplitude, and represents the modulated voltage both affecting the dielectric polarization and actuation of the microresonator.

Driving the mechanical resonator at its resonance frequency (i.e. $\Omega_{mod} = \Omega_m$) yields a maximum mechanical displacement amplitude

$$\varkappa(\Omega_m) = \sqrt{\frac{\pi}{2}}\frac{\left(c_{intrinsic} + 2c_{induced}V_{dc}\right)V_{mod}}{m_{eff}\Omega_m\Gamma_m}\ , \tag{4.16}$$

and measuring this displacement provides a mean to estimate the magnitude of the dielectric gradient forces experienced by the resonator.

4.1.3 Dielectric gradient force actuation setup

Our generic setup for dielectric gradient force actuation of microtoroids, depicted in Figure 4.2, is inspired from an antecedent dielectric gradient force actuation scheme [17]. The actuation of a microtoroid resonator is achieved by generating a nonuniform electric field inducing dielectric gradient forces to drive the mechanical motion. The electric field is produced by applying a voltage to a sharp electrode positioned above the microtoroid while an aluminum plate placed underneath the silicon chip supporting the silica microtoroids is grounded. The static dielectric polarization of the microtoroid consists of its intrinsic polarization and an induced polarization controlled by a constant DC voltage from a high voltage source[1]. An AC voltage modulation provided by a function generator[2] is combined to the DC voltage on a bias tee[3] in order to modulate

[1] Piezomechanik SVR 1000-3 High power analog amplifier.
[2] Agilent 33120A Function Generator.
[3] Mini-Circuits ZFBT-4R2GW+ Bias-Tee, modified to accept up to 300V at its DC input.

the electric field, thereby producing periodic dielectric forces at radio-frequencies. Both DC and AC voltages can be tuned independently.

We use sharp stainless steel needles with tip diameters around 2-5 μm as the top electrode. Alternatively one may use very sharp tungsten tips made by electromechanical etching, such as in scanning tunneling microscopes. The needle is affixed to a conductive copper holder which enables easy connection to the electrode with a BNC cable. The holder is placed on a 3-axis translation stage[4] with manual and piezo actuators providing control over the position of the electrode tip in the vicinity of the microtoroid resonator. Piezo actuation allows a fine tuning of the stage position over a 20 μm range by using a 3-channel piezo controller[5].

Observation of the mechanical displacement of the microtoroid is achieved by homodyne spectroscopy. The microtoroid WGM cavity is probed by an optical field which acquires phase fluctuations due to the transduction of mechanical displacements via the optomechanical interaction. The optical phase noise is then measured by a balanced homodyne detector and the PSD of the difference photocurrent is recorded by an electronic spectrum analyzer (ESA).

4.1.4 Characterization of the actuation setup

We characterize our dielectric gradient force actuation setup by varying the DC and AC voltage independently. Calibration of the homodyne noise power spectrum by adding a known phase modulation onto the optical probe allows the calibration of the amplitude of mechanical displacements as well as the calibration of the magnitude of dielectric gradient forces experienced by the microresonator.

In order to confirm that the phase noise measured at the AC drive frequency is due to the actuation of mechanical motion and not any electro-optic effect, we scan a mechanical resonance with an electrical network analyzer[6] (ENA), which consists of a combined signal generator and spectrum analyzer, replacing the individual signal generator and ESA in Figure 4.2. An ENA provides an electrical signal which serves both as a probe to an electrical network and as a reference to the measured frequency response of the electrical network. In this way both the gain and phase response of the electrical network is obtained. In our setup the probe signal from the ENA drives the AC modulation at the sharp electrode, then the ENA receives the homodyne difference signal from the optical phase quadrature measurement. We test the actuation setup for various DC voltage and we clearly observe a resonant amplification of the measured signal matching the response of a mechanical mode of our microtoroid to a driving force. Results are

[4]Thorlabs MAX311D 3-axis NanoMax stage with closed-loop piezos.
[5]Thorlabs BPC303 3-channel benchtop piezo controller with USB.
[6]Find reference for the network analyzer

shown in Figure 4.3 for the scan of the FFM with an AC drive voltage amplitude set to $V_{mod} = 220$ mV. We also observe the effect of the intrinsic polarization as the mechanical resonance is excited even at zero DC voltage, but the driving forces are canceled for a DC voltage around -30 V. Furthermore the scan of the FFM shows that the width of the mechanical resonance is not affected by the magnitude of the DC bias voltage.

Scaling with DC voltage

We investigated the scaling of the driven mechanical displacement with DC voltage by recording with the ESA the peak displacement amplitude of the FFM driven by a

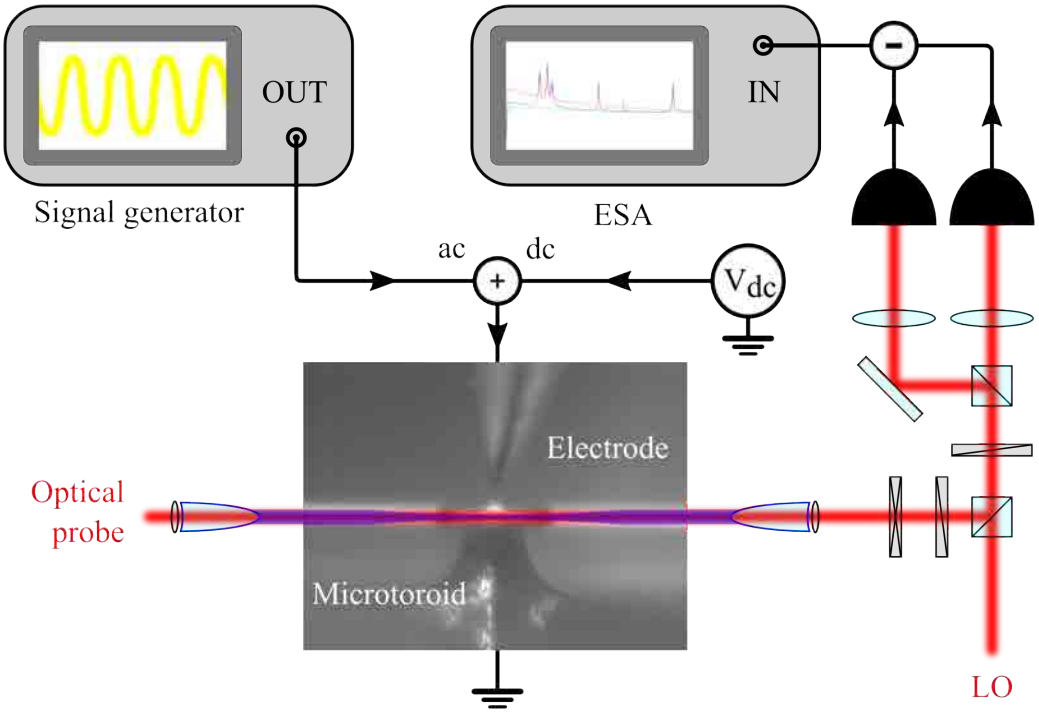

FIGURE 4.2: Experimental setup for dielectric gradient force actuation of a microtoroid resonator. The mechanical displacement of the microtoroid resonator is transduced via the optomechanical interaction onto the optical phase quadrature fluctuations of a probe beam. Subsequent measurement of the probe phase fluctuations is performed with a balanced homodyne detector and the power spectrum of the homodyne difference current is recorded by an electronic spectrum analyzer (ESA). Actuation of the microtoroid motion is achieved by generating a time-varying nonuniform electric field which subjects the microtoroid to dielectric gradient forces. A sharp electrode is positioned above the microtoroid while an aluminum plate placed underneath the chip supporting the microtoroid is grounded. Applying a voltage difference between the sharp electrode and the aluminum plate leads to the accumulation of opposite electric charges, thereby generating an electric field across the microtoroid resonator. The voltage is composed of a constant DC part from a tunable voltage supply combined to a weak modulation from a function generator. Alternatively, the signal generator and ESA are replaced by an electrical network analyzer (ENA).

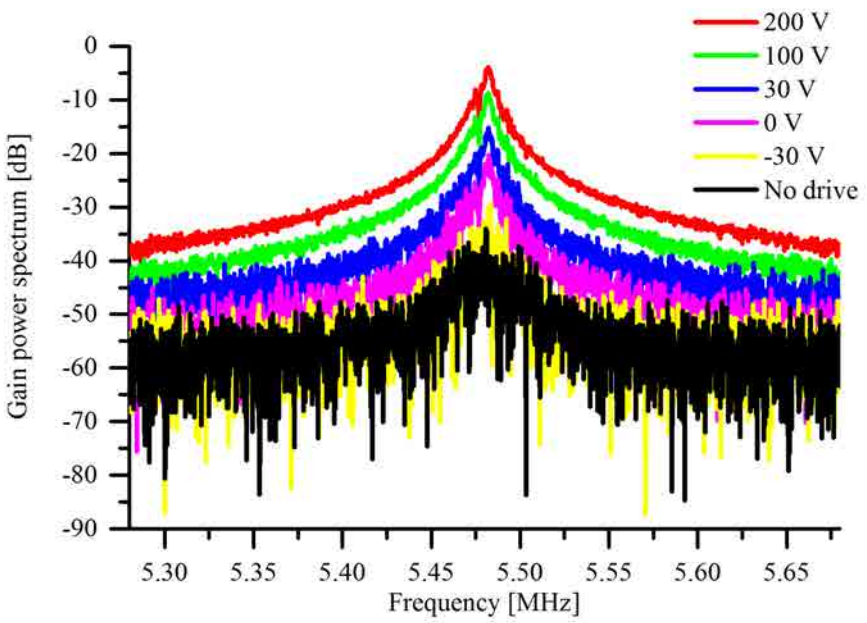

FIGURE 4.3: Gain power spectrum of the dielectric gradient force setup. A probe signal from an electrical network analyzer (ENA) is applied to the sharp electrode to drive the motion of a microtoroid via dielectric gradient forces. The displacement of the microtoroid is transduced onto an optical field whose phase noise is measured by balanced homodyne detection. The recorded homodyne signal is then compared to the electrical probe signal, and shows that the increase in phase noise is due to the excitation of the mechanical resonances by dielectric gradient forces. For this measurement the probe signal has an amplitude $V_{mod} = 220$ mV.

monochromatic voltage modulation at its resonance frequency from the function generator. The results in Figure 4.4(a) show a linear dependence of the peak displacement amplitude at the drive frequency with DC bias voltage applied to the electrodes, as expected from Equation (4.16). Furthermore the presence of an intrinsic polarization is confirmed by the nonzero driving of the oscillator at zero DC bias voltage. However the intrinsic polarization can be canceled by applying an appropriate DC bias voltage, here corresponding to -24.4 volts, thereby inhibiting the actuation of mechanical motion.

Besides varying the strength of the dielectric gradient force on the microtoroid, changing the DC bias voltage displaces the resonator in a new equilibrium position due to the time independent component of the dielectric gradient force, i.e. $F_{diel}(V_{dc})$ in Equation (4.12). Therefore we observed an alteration of the optical coupling between the tapered fiber and the WGM cavity, which required a repositioning of the tapered fiber relative to the microtoroid.

Scaling with AC voltage

Following the same method as for measuring the scaling of the driven mechanical displacement with DC voltage, we observe a linear scaling with AC voltage amplitude as expected from Equation (4.16), and shown in Figure 4.4(b).

4.2 Feedback cooling of a microtoroid resonator

A long standing interrogation touching the foundations of quantum mechanics has been the ability to prepare and observe macroscopic objects in a purely quantum mechanical state, such as the famous dead-and-alive cat imagined by Schrödinger. Indeed the quantum behavior of microscopic piece of matter such as atoms or molecules has been well studied and documented, but scaling up to larger massive systems, such as mechanical oscillators with dimensions in the order of micrometers, and weights in the order of micrograms, proves difficult. A prior requirement to the observation of the quantum behavior of a macroscopic oscillator is the ability to prepare the oscillator in or near its ground state. Ground state operation imposes a strict condition on the temperature T of the oscillator, which must satisfy $k_B T \ll \hbar\Omega_m$ in order to prevent the thermalization of the oscillator's state. Unless the mechanical frequency of the oscillator is in the gigahertz range, a domain almost exclusively restricted to optomechanical crystals [36, 37, 115], even dilution refrigerator temperatures of a few tens of millikelvins are not sufficient to reach ground state temperatures, thus additional cooling is required.

Cooling techniques can be divided into two categories, namely *feedback cooling* , also known as *cold damping*, and *cavity-assisted backaction cooling*, also known as *sideband cooling*. Cavity cooling schemes derive from the long known laser-cooling schemes applied to atoms and ions [9, 116, 117], and are based on the parametric coupling of a mechanical mode to a high-frequency bosonic resonator acting as a low temperature reservoir. In optomechanical systems the mechanical mode gets coupled to an optical cavity mode via radiation pressure interaction. Driving the cavity with a negative detuning results in a retarded radiation pressure backaction force which is anti-correlated with the Brownian motion of the oscillator, thereby leading to cooling of the mechanical mode [118] (cf. Figure 4.5(a)). In order to understand the conditions and limits of cavity-assisted backaction cooling it is interesting to represent the optomechanical interaction in terms of Raman scattering. Via the radiation pressure interaction of the optical drive at frequency ω_d, with the mechanical oscillator with resonance frequency Ω_m, drive photons scatters into anti-stokes (stokes) sidebands at frequency $\omega_d + \Omega_m$ ($\omega_d - \Omega_m$) by absorbing a phonon. Cooling of the mechanical oscillator is enhanced when the anti-stokes sidebands matches the cavity resonance, i.e. for a drive field red detuned from the cavity resonance by $\Delta = -\Omega_m$, as shown on Figure 4.5(b). It can be

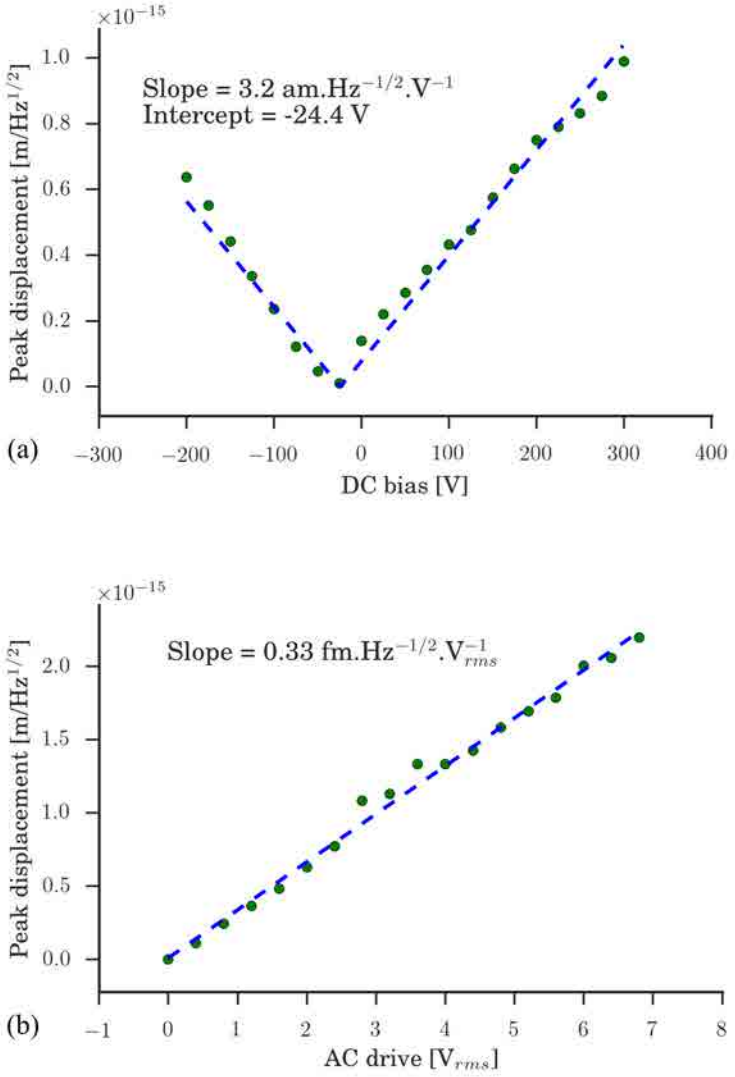

FIGURE 4.4: (a) Scaling of the mechanical actuation with DC bias voltage. The microtoroid motion is driven by a monochromatic AC voltage modulation with $\Omega_{mod}/2\pi = 5.48$ MHz and $V_{mod} = 500$ mV. The DC bias voltage is varied from 300 V to -200 V. Measured peak displacement amplitudes are fitted to a function $V_{dc} \mapsto Slope \times |V_{dc} - Intercept|$, giving $Slope = 3.2$ am.Hz$^{-1/2}$.V^{-1} and $Intercept = -24.4$ V. (b) Scaling of the mechanical actuation with DC bias voltage. The microtoroid motion is driven by a monochromatic AC voltage modulation at frequency $\Omega_{mod}/2\pi = 5.48$ MHz. The DC bias voltage is fixed to $V_{dc} = 50$ V and the amplitude of the AC modulation is varied from 6.8 V$_{rms}$ to 0 V$_{rms}$. Measured peak displacement amplitudes are fitted to a function $V_{mod} \mapsto Slope \times V_{mod}$, giving $Slope = 0.33$ fm.Hz$^{-1/2}$.V$_{rms}^{-1}$. Thermal noise was subtracted in all measurements of the mechanical peak displacement amplitude.

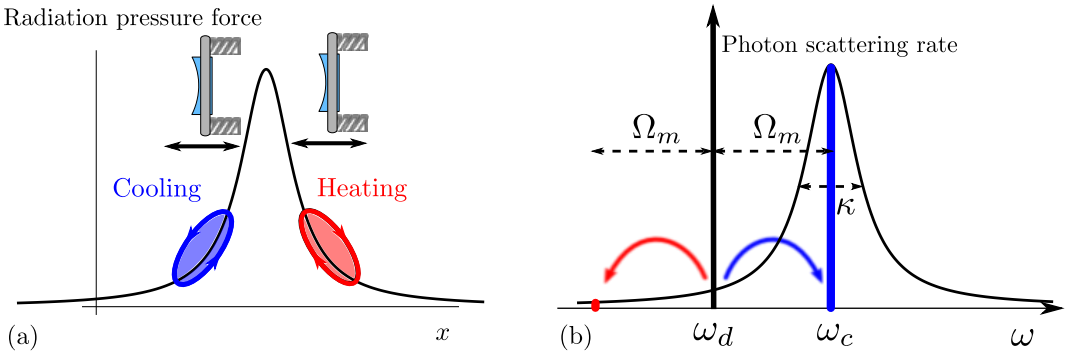

FIGURE 4.5: (a) Due to the finite cavity lifetime the radiation pressure force exerted by the intracavity field onto the mechanical oscillator evolves nonadiabatically thereby adding or removing work from the mechanical oscillator as the cavity driving field is respectively blue or red detuned from the cavity resonance. This gives rise to heating or cooling of the mechanical oscillator. (b) Raman scattering picture of cavity-assisted backaction cooling. The probability of a drive photon being scattered by a mechanical phonon is dictated by the cavity bandwidth. Therefore when the cavity driving field is red detuned by one mechanical resonance frequency from the cavity resonance, anti-stokes scattering is enhanced over stokes scattering what leads to a depletion of the phonon population, and cooling of the mechanical oscillator.

shown [119, 120] that ground state cooling can only be achieved when the cavity width is much larger than the heating rate induced by stokes scattering, but much smaller than the mechanical oscillation ($\Omega_m \gg \kappa$). So far, resolved sideband cooling has proven to be the most successful cooling technique for bringing a mechanical oscillator in its quantum ground state, both with microwave cavity electromechanical systems [42] and cavity optomechanical systems [37], reaching phonon occupations of respectively $n_m \sim 0.34$ and $n_m \sim 0.85$.

The study presented in this thesis is focusing on cavity optomechanical systems in the unresolved sideband regime which are not suited for the application of sideband cooling techniques. However as we will see in the following, cold damping is preferable and works best for systems in the unresolved sideband regime, and can in theory bring a mechanical oscillator in its quantum ground-state [120].

4.2.1 Cold damping

Cold damping relies on the sensitive measurement of mechanical motion to apply an active negative feedback, which increases the damping of the mechanical oscillator [121]. The optimal cooling that can be achieved with a feedback cooling scheme is usually limited by the measurement noise and the feedback gain. Cavity optomechanical systems allow ultrahigh-sensitivity measurements of mechanical motion due to the high frequencies of optical fields and the cavity-enhanced optomechanical interaction. Cooling can then be achieved by feeding back the measured low noise signal to a control force

actuating the mechanical oscillator. The radiation pressure force can be used for this purpose [29, 122, 123], but it remains inherently weak and the optical powers required to significantly actuate the mechanical motion may actually lead to heating, especially for cryogenically precooled systems. Alternative actuation schemes involve piezzo-driven cantilevers [112], coil actuators [124, 125], and optical tweezers [126]. In this thesis we investigate feedback cooling capabilities of a cavity optomechanical system with dielectric gradient force actuation of a mechanical mode [18].

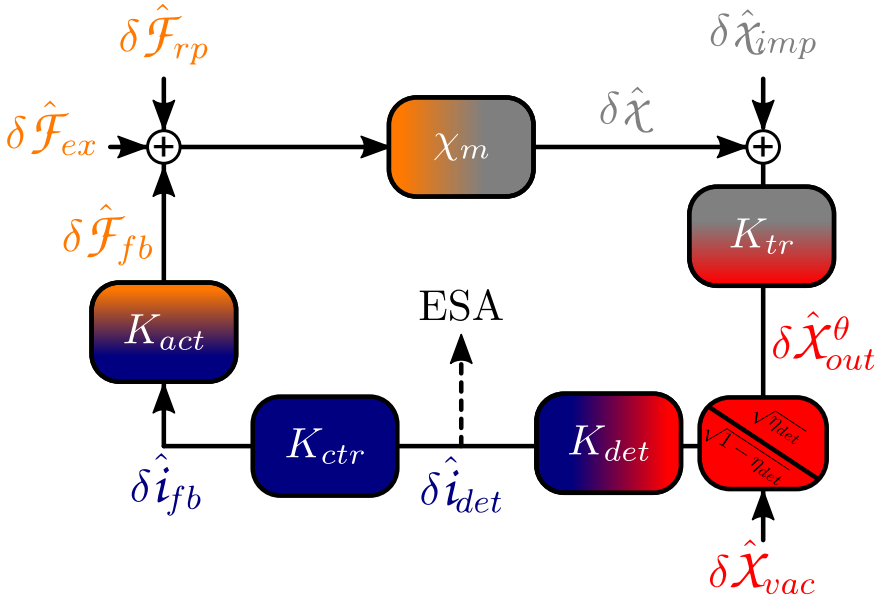

FIGURE 4.6: Block diagram of a feedback control scheme for a cavity optomechanical system. The response of a mechanical oscillator to applied forces is described by the mechanical susceptibility χ_m. The mechanical motion $\delta\hat{\mathcal{X}}$ is driven by external forces $\delta\hat{\mathcal{F}}_{ex}$, a radiation pressure force $\delta\hat{\mathcal{F}}_{rp} = -\hbar g_c \delta\hat{\mathcal{X}}_a$, and a feedback force $\delta\hat{\mathcal{F}}_{fb}$. The transduction of mechanical displacements onto an optical output field quadrature $\delta\hat{\mathcal{X}}^{\theta}_{out}$ is represented by the transfer function K_{tr}. Optical quantum noise is modeled as an uncertainty on the mechanical oscillator's position $\delta\hat{\mathcal{X}}_{imp}$. A nonunity detection efficiency η_{det} induces a mixing of the measured output field quadrature with vacuum fluctuations $\delta\hat{\mathcal{X}}_{vac}$. The measurement of the output field quadrature K_{det} produces a photocurrent $\delta\hat{i}_{det}$ which can be sent to an electronic spectrum analyzer (ESA) for data acquisition. The detection current is processed through an electrical circuit represented by the transfer function K_{ctr} in order to generate a current $\delta\hat{i}_{fb}$ controlling the feedback force applied to the mechanical oscillator.

We consider the continuous measurement of mechanical displacement presented in Chapter 3, and feedback the measurement signal to actuate the mechanical motion, as shown on Figure 4.6. We assume the feedback force to depend linearly on the measurement signal amplitude, what is consistent with the generation of dielectric gradient forces from the homodyne difference current of the displacement measurement. Among the forces actuating the mechanical oscillator, we distinguish the feedback force, $\delta\hat{\mathcal{F}}_{fb}(\Omega)$, from other external forces in Equation 3.6, such that the mechanical position operator

reads,

$$\delta\hat{\chi}(\Omega) = \chi_m(\Omega)\left[-\hbar g_c \delta\hat{\mathcal{X}}_a(\Omega) + \delta\hat{\mathcal{F}}_{ex}(\Omega) + \delta\hat{\mathcal{F}}_{fb}(\Omega)\right] . \tag{4.17}$$

Without loss of generality within the frame of optomechanics, we may consider that the mechanical motion is transduced onto an output optical field, and a subsequent measurement is performed on an arbitrary quadrature given by

$$\delta\hat{\chi}^{\theta}_{out}(\Omega) = K_{tr}(\Omega)\left[\delta\hat{\chi}(\Omega) + \delta\hat{\chi}_{imp}(\Omega)\right] , \tag{4.18}$$

where $\delta\hat{\chi}_{imp}(\Omega)$ indicates the imprecision noise corresponding to the optical quantum noise of the output field.

Considering the general case of a nonunit detection efficiency η_{det}, the signal obtained from the measurement of the arbitrary output quadrature is given by

$$\delta\hat{i}_{det}(\Omega) = K_{det}(\Omega)\left[\sqrt{\eta_{det}}\delta\hat{\chi}^{\theta}_{out}(\Omega) + \sqrt{1-\eta_{det}}\delta\hat{\chi}_{vac}(\Omega)\right] , \tag{4.19}$$

where $K_{det}(\Omega)$ is the transfer function of the detector. We have modeled the nonunit detection efficiency of the detector by introducing loss in the form of an uncorrelated vacuum field $\delta\hat{\chi}_{vac}(\Omega)$ mixing with the output field on a beam splitter with transmittivity η_{det}. The measurement signal is represented as an electrical current in order to be consistent with photodetection techniques relevant to this thesis. Equation (4.19) is analog to Equation (1.94), and so can represent the homodyne difference current obtained from the balanced homodyne detection of an arbitrary output phase quadrature.

The signal obtained from the measurement of the arbitrary output quadrature is subsequently processed through a control feedback loop, resulting in the feedback signal

$$\delta\hat{i}_{fb}(\Omega) = K_{ctr}(\Omega)\delta\hat{i}_{det}(\Omega) , \tag{4.20}$$

where K_{ctr} is a transfer function describing the processing of the measurement signal, e.g. electronic filtering and amplification of the homodyne difference current. The feedback signal is then used to generate a force that controls the mechanical motion, and can be written

$$\delta\hat{\mathcal{F}}_{fb}(\Omega) = K_{act}(\Omega)\delta\hat{i}_{fb}(\Omega) , \tag{4.21}$$

where K_{act} translate the feedback signal into a mechanical actuation force, e.g. the dielectric gradient force produced by the alternative charging of electrodes. For simplicity of the calculations, we assume that detection and feedback do not add classical noise to the signal. In reality, active electronic components such as amplifiers would add some electronic noise to the feedback signal, but under appropriate choice of quality components and strength of the measurement signal, it is reasonable to neglect this electronic

noise.

Finally combining the above equations (4.17, 4.18, 4.19, 4.21), the mechanical position operator can be recast into

$$\delta\hat{\chi}(\Omega) = \chi_{fb}(\Omega)\Big[-\hbar g_c \delta\hat{\mathcal{X}}_a(\Omega) + \delta\hat{\mathcal{F}}_{ex}(\Omega) \\ + K_{act}K_{ctr}K_{det}\left(\sqrt{\eta_{det}}K_{tr}\delta\hat{\chi}_{imp}(\Omega) + \sqrt{1-\eta_{det}}\delta\hat{\chi}_{vac}(\Omega)\right)\Big] \ , \quad (4.22)$$

with the effective feedback-induced mechanical susceptibility given by

$$\chi_{fb}(\Omega) = \left[\chi_m^{-1}(\Omega) - \sqrt{\eta_{det}}K_{act}(\Omega)K_{ctr}(\Omega)K_{det}(\Omega)K_{tr}(\Omega)\right]^{-1} \ . \quad (4.23)$$

The feedback modifies the dynamical response of the mechanical oscillator to applied external forces, by altering its susceptibility. Combining the transfer functions of the processes involved in the feedback loop into a single feedback transfer function,

$$K_{fb}(\Omega) = m_{eff}^{-1}\sqrt{\eta_{det}}K_{act}(\Omega)K_{ctr}(\Omega)K_{det}(\Omega)K_{tr}(\Omega) \ , \quad (4.24)$$

then writing the effective susceptibility of the mechanical oscillator as

$$\chi_{fb}^{-1}(\Omega) = m_{eff}\left(\Omega_m^2 - \mathrm{Re}[K_{fb}(\Omega)] - \Omega^2 - i\Omega\Gamma_m - i\,\mathrm{Im}[K_{fb}(\Omega)]\right) \ , \quad (4.25)$$

shows that the real part of the feedback gain contributes to the spring constant of the mechanical oscillator while its imaginary part contributes to the damping of the mechanical oscillator. In more physical terms this means that the stiffening or softening of the mechanical oscillator, as well as its dissipative coupling to the environment, can be controlled by designing an appropriate feedback transfer function.

In order to cool the mechanical mode, the optimum choice of feedback transfer function is the differentiation with negative feedback, i.e. $K_{fb}(\Omega) = -i\Omega G_{fb}$ with $G_{fb} \in \mathbb{R}^-$ the feedback gain, such that the feedback generates a purely dissipative force that damps the motion of the mechanical oscillator. In practice however, such a feedback transfer function is hardly feasible due to the available technologies for transduction, detection and actuation of mechanical displacements, that limits the bandwidth of the feedback loop. Moreover the unavoidable delays introduced by the feedback loop prevents the design of an arbitrary feedback transfer function.

A key requirement for the implementation of a cold damping scheme is the stability of the feedback transfer function. A feedback loop is stable if every bounded input produces a bounded output, which in our case translates into the requirement that all the poles of the Laplace transform of the time-dependent effective mechanical susceptibility, $\chi_{fb}(s)$, lie in the left-hand side of the complex half-plane [27, 127]. This stability

condition imposes restrictions over the choice of the feedback transfer function that can be used for feedback cooling of a mechanical oscillator.

4.2.2 Feedback transfer function of a cavity optomechanical system

Apart from the radiation pressure force entering Equations (4.17) and (4.22), the model of feedback developed so far can be transposed to any scheme involving the detection and feedback actuation of mechanical motion. We now turn to cavity optomechanical systems specifically in which the radiation pressure interaction between a mechanical oscillator and a cavity field allows indirect optical measurements of mechanical displacements.

For a cavity optomechanical system probed on resonance, the transfer function describing the transduction of mechanical motion onto the output field can be found from Equation (3.16) to be

$$K_{tr}(\Omega) = \frac{2\sqrt{\eta(1-\eta)}}{1-i\bar{\Omega}} \frac{g_c}{\sqrt{\kappa_c}} \sin(\theta) \ . \tag{4.26}$$

The transduction acts as a low pass filter with cutoff frequency $\kappa/2$, because the optical cavity filters signals that lie outside of its resonance, i.e. frequencies larger than its half-width.

The detection transfer function depends on the detection technique employed but consists essentially of a linear gain, and filtering from photodetectors. Photodetectors have a limited bandwidth that prevents the detection of high-frequency signals in the gigahertz range and higher. However they can in principle be tuned for particular purposes within a reasonable frequency range, such that the detection transfer function is flat in the frequency band occupied by the signal of interest, and can be approximated by a frequency-independent constant gain, $K_{det}(\Omega)$.

The control transfer function, $K_{ctr}(\Omega)$, describes the shaping of the feedback signal that is necessary to control the system and achieve cooling of the mechanical motion. Practically, the design of the feedback signal is performed by electronic filtering and amplification of the current provided by the photodetection. This is the most controllable part of the feedback loop because of the wide variety of electronic components commercially available (e.g. filters and amplifiers), and their ease of use. For convenience we may write the control transfer function in terms of a frequency-dependent gain and phase response,

$$K_{ctr}(\Omega) = g_{ctr}(\Omega) e^{i\Theta(\Omega)} \ , \tag{4.27}$$

with $g_{ctr}(\Omega)$, $\Theta(\Omega) \in \mathbb{R}$.

The actuation transfer function, $K_{act}(\Omega)$, describes the process transforming the signal, usually in the form of a current, into a mechanical actuation force driving the

mechanical oscillator. It is determined by the nature of the force, e.g. dielectric gradient force [18], piezoelectric effect [112], radiation pressure force [29, 122, 123]. The transfer function of a dielectric gradient force actuation scheme, such as discussed in Section 4.1, is given by (cf. Equation (4.14)),

$$K_{act}(\Omega) = \left(c_{intrinsic} + 2c_{induced}(\Omega)V_{dc}\right) Z_{fb}(\Omega) \ , \tag{4.28}$$

where $Z_{fb}(\Omega)$ is the electrical impedance of the feedback circuit, and we assume that the bias voltage is much larger than the signal voltage so that we can neglect quadratic terms in the signal voltage. The characterization of our actuation setup shows that the dielectric gradient force is frequency-independent over the frequency band occupied by the mechanical oscillator's resonance, therefore we may consider the transfer function to be constant, $K_{act}(\Omega) \approx K_{act}$.

Finally we may model the feedback transfer function as

$$K_{fb}(\Omega) = g_{fb} e^{i\Omega\tau_{fb}} \frac{g_{ctr}(\Omega) e^{i\Theta(\Omega)}}{1 - i\bar{\Omega}} \ , \tag{4.29}$$

where $g_{fb} \in \mathbb{R}^+$ is a frequency-independent gain which depends on the transduction, detection and actuation efficiencies, and τ_{fb} is the time delay of the feedback loop which introduces a frequency-dependent phase shift on the feedback signal. Considering the simple case where the control transfer function consists of a real frequency-independent gain $g_{ctr}(\Omega) \approx g_{ctr}$, with $\Theta = 0$, the feedback-induced effective susceptibility of Equation (4.23) can be read as the susceptibility of an oscillator with effective resonance frequency and damping rate given by

$$\Omega_{fb}^2 = \Omega_m^2 - \frac{g_{fb} g_{ctr}}{1 + \bar{\Omega}^2} \left[\cos(\Omega\tau_{fb}) - \bar{\Omega}\sin(\Omega\tau_{fb})\right] \ , \tag{4.30}$$

$$\Gamma_{fb} = \Gamma_m + \frac{g_{fb} g_{ctr}}{1 + \bar{\Omega}^2} \frac{1}{\Omega} \left[\sin(\Omega\tau_{fb}) + \bar{\Omega}\cos(\Omega\tau_{fb})\right] \ . \tag{4.31}$$

Due to the filtering of the feedback signal by the optical cavity, the feedback is most effective in altering the dynamics of the mechanical oscillator when the cavity optomechanical system is in the unresolved sideband regime, i.e. $\bar{\Omega} \sim \bar{\Omega}_m \ll 1$. In this regime the phase quadrature field fluctuation from the cavity output is adiabatically following the oscillator position, thus it retains the full magnitude of the mechanical oscillations. On the other hand, in the resolved sideband regime, the longer lifetime of the cavity averages the oscillator position over time, thus reducing the magnitude of the signal transduced onto the output phase quadrature field fluctuation. Now focusing on cold damping in the unresolved sideband regime, we observe that the mechanical oscillator can be alternatively softened, dampened, stiffened, or freed by tuning the feedback delay time, such that $\Omega\tau_{fb} \sim \Omega_m\tau_{fb} = 0$, $\pi/2$, π, and $3\pi/2 \mod 2\pi$, respectively, for $g_{ctr} > 0$.

Note however that for keeping the effective resonance frequency and damping rate approximately constant over the mechanical resonance, we need the time delay of the feedback to be much shorter than the effective decay time of the mechanical oscillations, i.e. $\tau_{fb} \ll \Gamma_{fb}^{-1}$.

Stability of the feedback

As stated previously the stability of the feedback requires that all the poles of the Laplace transform of the time-dependent effective mechanical susceptibility, $\chi_{fb}(s)$, lie in the left-hand side of the complex half-plane [27, 127]. The poles are the solutions s of the equation

$$\left(s^2 + s\Gamma_m + \Omega_m^2\right)\left(s + \frac{\kappa}{2}\right) D_{ctr}(s) = g_{fb} e^{-s\tau_{fb}} \frac{\kappa}{2} N_{ctr}(s) \ , \tag{4.32}$$

where $N_{ctr}(s)$ and $D_{ctr}(s)$ are respectively the numerator and the denominator of the Laplace transform of the control transfer function, i.e. $K_{ctr}(s) = N_{ctr}(s)/D_{ctr}(s)$. To some extent the Laplace transform is obtained from the Fourier transform by substituting the frequency Ω by the complex variable $i \cdot s$ ($s \in \mathbb{C}$). The stability criterion imposes constraints over the maximum gain and bandwidth of the feedback loop [27]. For a high Q mechanical oscillator in the unresolved sideband regime, a sufficient (but not necessary) condition for stability is given by $|g_{fb} g_{ctr}/\Omega_m| < \Gamma_m$. This condition prevents the effective mechanical damping to become negative, cf. Equation (4.31).

4.2.3 Displacement spectrum of the feedback actuated resonator

The PSD of the mechanical position can be derived from Equation (4.22), however correlations between the radiation pressure force and the imprecision noise renders a full analytical expression rather cumbersome in the case of an arbitrary quadrature measurement of the output field fluctuations. Therefore, for simplicity and in accordance with Section 3.2.3 as well as with the experimental work presented in this thesis, we restrict ourselves to a measurement of the phase quadrature fluctuations of the output field, which carry the strongest modulation induced by mechanical oscillations, and whose shot noise is uncorrelated with the amplitude quadrature fluctuations of the intracavity field. The PSD of the oscillator position then reads,

$$\begin{aligned}\langle|\delta\hat{\chi}(\Omega)|^2\rangle =& m_{eff}^2 |\chi_{fb}(\Omega)|^2 |K_{fb}(\Omega)|^2 \left[\langle|\delta\hat{\chi}_{imp}(\Omega)|^2\rangle + \frac{1-\eta_{det}}{\eta_{det}|K_{tr}(\Omega)|^2}\langle|\delta\hat{\chi}_{vac}(\Omega)|^2\rangle\right] \\ &+ |\chi_{fb}(\Omega)|^2 \left[\langle|\delta\hat{\mathcal{F}}_{ex}(\Omega)|^2\rangle + \langle|\delta\hat{\mathcal{F}}_{rp}(\Omega)|^2\rangle\right] \ . \end{aligned} \tag{4.33}$$

The first term in Equation (4.33) represents the mechanical displacement driven by the quantum noise of the probe field and the detection noise from imperfect detectors that

is injected into the feedback loop. We group the noise contributions to the feedback signal under the position noise operator,

$$\delta\hat{\chi}^{(fb)}_{noise}(\Omega) = \delta\hat{\chi}_{imp}(\Omega) + \frac{\sqrt{1-\eta_{det}}}{\sqrt{\eta_{det}}K_{tr}(\Omega)}\delta\hat{\chi}_{vac}(\Omega) \ , \tag{4.34}$$

to which we may also add classical noise from the non-ideality of the the measurement and feedback (e.g. phase noise from deviations in the locking of the LO and signal phases, or electrical noise from electronic components). The second term in Equation (4.33) arises from the driving of the mechanical oscillator by external forces (e.g. thermal Brownian force) and radiation pressure force from the quantum fluctuations of the probe field, i.e. the quantum backaction force. However the QBA force is usually much weaker than the thermal Brownian force and remains hidden below the measurement noise in most experiments of mechanical displacement measurements, having been observed only recently in state of the art experiments on macroscopic oscillators [33, 89]. Therefore we neglect the effect of QBA in our treatment of the feedback cooling scheme.

4.2.4 Effective temperature of the feedback actuated resonator

Following 2.2.3 we may attribute an effective temperature to a mechanical oscillator, which is proportional to the area under the PSD of the mechanical position fluctuations (cf. Equation (2.27)). The effective temperature T_{fb} of a mechanical oscillator subjected to a feedback actuation force can be calibrated relative to the effective temperature T of the same oscillator in the absence of feedback actuation, which is the temperature of the oscillator's environment, assuming thermal equilibrium. For a cavity optomechanical system in the unresolved sideband regime, the spectral response of the optical cavity over a sideband frequency range within the resonance of the mechanical oscillator is flat, and so is the noise term in Equation (4.33). If we further assume that the external force fluctuations driving the mechanical oscillator consists essentially of white noise in the same sideband frequency range, and that the feedback-induced effective susceptibility of the oscillator retains a Lorentzian profile with effective resonance frequency and damping rate, Ω_{fb} and Γ_{fb}, respectively, then the temperature of the feedback actuated oscillator is given by

$$\frac{T_{fb}}{T} = \frac{\int_{-\infty}^{\infty}\langle|\delta\hat{\chi}(\Omega)|^2\rangle d\Omega}{\int_{-\infty}^{\infty}\langle|\delta\hat{\chi}(\Omega)|^2\rangle_{K_{fb}=0}d\Omega} = \frac{\Gamma_{fb}\langle|\delta\hat{\chi}(\Omega_{fb})|^2\rangle}{\Gamma_m\langle|\delta\hat{\chi}(\Omega_m)|^2\rangle_{K_{fb}=0}} \ . \tag{4.35}$$

For a feedback transfer function consisting of a frequency-independent proportional gain, $g_{fb}g_{ctr} = \Omega_m\Gamma_m G_{fb} \geq 0$, and time delay τ_{fb} over the sideband frequency range covering the mechanical resonance, a pure dissipative cooling of the mechanical oscillator requires $\Omega_m\tau_{fb} = \pi/2 \mod 2\pi$, such that $\Omega_{fb} \approx \Omega_m$ and $\Gamma_{fb} \approx \Gamma_m(1+G_{fb})$. The condition $\Gamma_{fb} \ll \tau_{fb}^{-1}$ is also needed for the phase response of the feedback to remain

approximately constant over the mechanical resonance, thus retaining the Lorentzian profile of the mechanical susceptibility. Then substituting Equation (4.33) into Equation (4.35) yields,

$$\frac{T_{fb}}{T} = \left(1 + \frac{G_{fb}^2}{\mathrm{SNR}}\right) \frac{1}{1 + G_{fb}} \ , \tag{4.36}$$

where we introduced the signal-to-noise ratio (SNR) of the peak of the mechanical position noise to the optical measurement noise without feedback,

$$\mathrm{SNR} = \frac{\langle |\delta\hat{\chi}(\Omega_m)|^2 \rangle_{K_{fb}=0}}{\langle |\delta\hat{\chi}_{noise}^{(fb)}(\Omega_m)|^2 \rangle} \ , \tag{4.37}$$

which can be directly determined from the PSD of the detected cavity output field fluctuations. For fixed detection conditions, the minimum temperature that can be achieved by cold damping is limited to

$$T_{min} = 2T \frac{\sqrt{1 + \mathrm{SNR}} - 1}{SNR} \ , \tag{4.38}$$

for a feedback gain $G_{fb} = \sqrt{1 + \mathrm{SNR}} - 1$. At larger gain, $G_{fb} > \sqrt{1 + \mathrm{SNR}} - 1$, the driving of the mechanical oscillator by the measurement noise injected into the feedback loop overcomes the damping of the oscillations, and the temperature increases with the feedback gain. Therefore it is essential to maximize the SNR in order to reach high levels of cooling, and ultimately cool the mechanical oscillator into its quantum ground state.

4.2.5 In-loop and out-of-loop position measurements

The effective temperature of the mechanical oscillator can in principle be extracted from the cavity output fluctuation measurement by subtracting the transduction and detection noise. However, the feedback introduces correlations between the mechanical motion and the measurement noise injected into the feedback loop, what leads to a *squashing* of the measurement noise [18, 27, 112, 113, 128]. One must then distinguish in-loop and out out-of-loop measurements of the feedback actuated mechanical motion to infer the effective temperature of the oscillator. In the first case the measurement signal is used both for the feedback and for the determination of the effective temperature such that the mechanical motion is correlated with the measurement noise. In the second case the temperature is inferred from a displacement measurement independent of the feedback loop, such that the measurement noise is uncorrelated with the mechanical motion.

The measured oscillator position $\delta\hat{\mathfrak{X}}_{meas}$ consists of the real position given by Equation (4.22), plus an uncertainty due to the measurement noise $\delta\hat{\mathfrak{X}}^{(ms)}_{noise}$, and reads

$$\delta\hat{\mathfrak{X}}_{ms}(\Omega) = \delta\hat{\mathfrak{X}}(\Omega) + \delta\hat{\mathfrak{X}}^{(ms)}_{noise}(\Omega) \ , \tag{4.39}$$

$$= \chi_{fb}(\Omega)\left[\delta\hat{\mathcal{F}}_{ex}(\Omega) + m_{eff}K_{fb}(\Omega)\delta\hat{\mathfrak{X}}^{(fb)}_{noise}(\Omega)\right] + \delta\hat{\mathfrak{X}}^{(ms)}_{noise}(\Omega) \ . \tag{4.40}$$

The PSD of the measured oscillator position is therefore given by

$$\langle|\delta\hat{\mathfrak{X}}_{ms}(\Omega)|^2\rangle = \langle|\delta\hat{\mathfrak{X}}^{(ms)}_{noise}(\Omega)|^2\rangle + 2m_{eff}\mathrm{Re}[\chi_{fb}(\Omega)K_{fb}(\Omega)]\langle\delta\hat{\mathfrak{X}}^{(fb)}_{noise}(\Omega)\delta\hat{\mathfrak{X}}^{(ms)}_{noise}(-\Omega)\rangle$$
$$+ |\chi_{fb}(\Omega)|^2\left[\langle|\delta\hat{\mathcal{F}}_{ex}(\Omega)|^2\rangle + m^2_{eff}|K_{fb}(\Omega)|^2\langle|\delta\hat{\mathfrak{X}}^{(fb)}_{noise}(\Omega)|^2\rangle\right] \ . \tag{4.41}$$

For an out-of-loop measurement the measured noise is uncorrelated with the feedback noise thus the second term in Equation (4.41) cancels, but for an in-loop measurement the noise correlation term must be kept.

From Equation (4.41) we derive the in-loop measured PSD for an arbitrary feedback transfer function,

$$\langle|\delta\hat{\mathfrak{X}}^{(in)}_{ms}(\Omega)|^2\rangle \ = \ |\chi_{fb}(\Omega)|^2\langle|\delta\hat{\mathcal{F}}_{ex}(\Omega)|^2\rangle \ + \ |\chi_{fb}(\Omega)|^2|\chi^{-1}_m(\Omega)|^2\langle|\delta\hat{\mathfrak{X}}^{(ms)}_{noise}(\Omega)|^2\rangle \ , \tag{4.42}$$

where we assumed that the feedback and measurement noise are identical. The second term clearly shows the squashing of the measurement noise within the resonance of the mechanical oscillator. For a cavity optomechanical system in the unresolved sideband regime with the aforementioned cold damping transfer function, $K_{fb}(\Omega) = i\Omega_m\Gamma_m G_{fb}$, the PSD of the measured oscillator position obtained from an in-loop measurement can be written,

$$\langle|\delta\hat{\mathfrak{X}}^{(in)}_{ms}(\Omega)|^2\rangle = |\chi_{fb}(\Omega)|^2\langle|\delta\hat{\mathcal{F}}_{ex}(\Omega)|^2\rangle + \langle|\delta\hat{\mathfrak{X}}^{(ms)}_{noise}(\Omega)|^2\rangle$$
$$+ |\chi_{fb}(\Omega)|^2|\chi^{-1}_m(\Omega_m)|^2G^2_{fb}\left(1 - \frac{2}{G_{fb}} - \frac{2\Omega}{\Omega_m}\right)\langle|\delta\hat{\mathfrak{X}}^{(ms)}_{noise}(\Omega)|^2\rangle \ . \tag{4.43}$$

From Equation (4.35) we derive the effective temperature that can be inferred from an in-loop measurement by subtracting the measurement noise,

$$\frac{T^{(in)}_{fb}}{T} = \frac{\Gamma_{fb}(\langle|\delta\hat{\mathfrak{X}}^{(in)}_{ms}(\Omega_m)|^2\rangle - \langle|\delta\hat{\mathfrak{X}}^{(ms)}_{noise}(\Omega_m)|^2\rangle)}{\Gamma_m|\chi_m(\Omega_m)|^2\langle|\delta\hat{\mathcal{F}}_{ex}(\Omega_m)|^2\rangle} \tag{4.44}$$

$$= \left(1 - \frac{(2+G_{fb})G_{fb}}{\mathrm{SNR}}\right)\frac{1}{1+G_{fb}} \ . \tag{4.45}$$

The inferred temperature match approximately the actual temperature of the mechanical oscillator given in Equation (4.36) only for low feedback gain $G_{fb} \ll \sqrt{\mathrm{SNR}}$. At the optimum feedback cooling gain, $G_{fb} = \sqrt{1+\mathrm{SNR}} - 1$, the inferred temperature reads

zero, then becomes negative for higher gains. This behavior is clearly unphysical and can be explained by the squashing of the measurement noise resulting from the correlations introduced by the feedback. The noise correlations are restricted to the bandwidth of the feedback which is usually determined by the effective width of the mechanical resonance, thus at high gains the measured PSD shows an inverted Lorentzian with width Γ_{fb}, centered at the mechanical resonance frequency Ω_m [18, 112, 113, 122, 123]. Despite the inaccuracy of the in-loop temperature inference due to measurement noise correlations, the effective temperature of the mechanical oscillator can still be obtained indirectly by using the formula

$$\frac{T_{fb}}{T_{fb}^{(in)}} = \frac{\mathrm{SNR} + G_{fb}^2}{\mathrm{SNR} - (2 + G_{fb})G_{fb}} \ , \tag{4.46}$$

given that the feedback gain and the SNR are calibrated and determined accurately.

Direct inference of the mechanical oscillator temperature is possible from the out-of-loop measurement the oscillator position, which gives the following PSD

$$\begin{aligned}\langle|\delta\hat{\chi}_{ms}^{(out)}(\Omega)|^2\rangle = |\chi_{fb}(\Omega)|^2\langle|\delta\hat{\mathcal{F}}_{ex}(\Omega)|^2\rangle + \langle|\delta\hat{\chi}_{noise}^{(ms)}(\Omega)|^2\rangle \\ + |\chi_{fb}(\Omega)|^2|\chi_m^{-1}(\Omega_m)|^2 G_{fb}^2\langle|\delta\hat{\chi}_{noise}^{(fb)}(\Omega)|^2\rangle \ ,\end{aligned} \tag{4.47}$$

where the noise correlation term in Equation (4.41) cancels. The out-of-loop inferred temperature, after subtracting the measurement noise, then reads

$$\frac{T_{fb}^{(out)}}{T} = \frac{\Gamma_{fb}(\langle|\delta\hat{\chi}_{ms}^{(out)}(\Omega_m)|^2\rangle - \langle|\delta\hat{\chi}_{noise}^{(ms)}(\Omega_m)|^2\rangle)}{\Gamma_m|\chi_m(\Omega_m)|^2\langle|\delta\hat{\mathcal{F}}_{ex}(\Omega_m)|^2\rangle} \tag{4.48}$$

$$= \left(1 + \frac{G_{fb}^2}{\mathrm{SNR}}\right)\frac{1}{1 + G_{fb}} \ , \tag{4.49}$$

and is equal to the effective temperature of the mechanical oscillator given by Equation (4.36). The out-of-loop measurement provides a direct mean to infer the effective temperature, that does not require prior determination of the feedback gain or the SNR. The relative cooling or heating of the oscillator is directly given by the ratio of the oscillator position variance measured with and without feedback gain. On the other hand, performing an out-of-loop measurement involves an additional optical probe to transduce mechanical displacements independently of the feedback loop, thus it imposes further demands on the experimental resources (e.g. laser sources, optical components, optical detectors). For example, making use of the squeezing-enhanced detection scheme presented in Chapter 3 to increase the SNR in the feedback loop and consequently decrease the minimum achievable effective temperature, would only be relevant if the quadrature noise of the out-of-loop probe is also squeezed, therefore an additional squeezing source

is needed (on top of an additional homodyne detector, etc.) what considerably increases the complexity of the experimental setup. Moreover the optical power of the out-of-loop probe adds to the optical power of the in-loop probe, thereby increasing the thermal and nonlinear effects in the optical cavity, as wells as the radiation pressure backaction force driving the mechanical motion.

4.2.6 Feedback cooling experiment

The cold damping scheme employed in this thesis work combines high-sensitivity measurements of mechanical motion with strong electrical actuation [17, 18] of vibrational modes of a cavity optomechanical system. The motion of a microtoroid resonator is transduced onto an optical probe whose phase quadrature fluctuations are subsequently measured with a homodyne detector (cf. Chapter 3). The homodyne photocurrent is used as a feedback signal to generate dielectric gradient forces actuating the mechanical oscillator motion. Compared to the method described in [18], where the feedback signal is acquired by intensity detection of the probe field, our method reaches similar sensitivities with a probe power reduced by two orders of magnitude, making it less prone to thermal and nonlinear effects. Also by driving the optical cavity on resonance, our scheme is safe from dynamical backaction heating [129]. Furthermore, with shot noise limited balanced homodyne detection, the feedback noise is independent of the intensity noise of the optical probe, so it is uncorrelated with the radiation pressure backaction. This is of particular importance for reaching ground state cooling of the mechanical motion, as the high SNR required in the feedback comes with the expense of non-negligible quantum backaction noise.

Dielectric force feedback actuation setup

The experimental setup employed for the feedback actuation of microtoroid resonators is based on the dielectric gradient force actuation setup presented in 4.1.3. As shown on Figure 4.7, half of the electrical signal obtained via the homodyne detection of the cavity output field fluctuations is tapped of by a power splitter[7] to allow for acquisition of its PSD with an ESA. The remaining half is directed to the AC input of the bias tee in order to modulate the electric field generated at the sharp electrode, and consequently drive the dielectric gradient force actuating the microtoroid resonator.

The feedback control transfer function is designed by a combination of phase delays, amplifiers and frequency filters. The phase delays simply consist of a series of switch-controlled coaxial delay[8] allowing for a full 2π phase delay at the mechanical resonance frequency, with a resolution around $3 \cdot 10^{-3}$ rad. The gain of the feedback signal

[7] Mini-Circuits ZSC-2-1 Coaxial Power Splitter/Combiner, 2 Way-0°, 0.1 to 400 MHz
[8] Stanford Research Systems DB64 Coax Delay, 63.5 ns delay with 0.5 ns resolution.

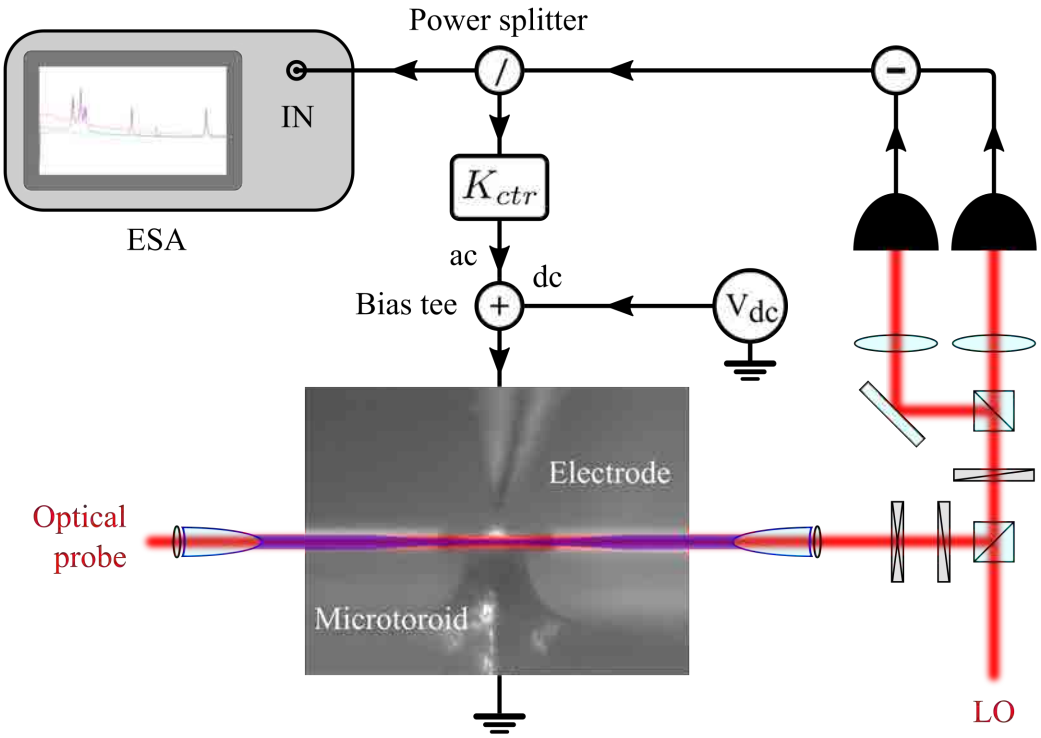

FIGURE 4.7: Experimental setup for dielectric gradient force feedback actuation of a microtoroid resonator. Measurement and actuation of the mechanical resonator motion is operated in the same way as with the dielectric gradient force actuation setup of Figure 4.2. The electrical signal provided by the homodyne detector is injected into the feedback loop and controls the dielectric gradient force actuating the mechanical resonator. The feedback signal is shaped by electrical filters and amplifiers represented by the control transfer function K_{ctr}. Half of the feedback signal is tapped of by a power splitter and directed to an ESA for acquisition of its PSD.

is enhanced by linear, low-noise, large-bandwidth amplifiers[9,10] within the limit where the feedback signal do not saturate the amplifiers themselves. Saturation of electrical components at the detection or feedback stage sets a technical boundary on the maximum gain that can be employed in the feedback loop. When cooling a single mechanical mode, saturation may result from the amplification of the transduced mechanical resonance signal itself, or from parasitic signals measured from neighboring mechanical modes. Frequency filters can be used to suppress these parasitic signals but care must be taken as they introduce additional phase delays in the feedback loop. As the amplifiers provide a fixed gain, we use a series of large-bandwidth tunable attenuators[11,12,13] for adjusting the feedback gain.

[9] Stanford Research Systems SR445A 350 MHz Preamplifier, 4 channels with gain 5
[10] Mini-Circuits ZFL-500LN Low Noise Amplifier, 0.1 to 500 MHz, 28 dB gain.
[11] JFW Industries 50R-043 Single Rotary Attenuator, 100 dB attenuation by 10 dB step
[12] JFW Industries 50R-019 Single Rotary Attenuator, 10 dB attenuation by 1 dB step
[13] JFW Industries 50R-028 Single Rotary Attenuator, 1 dB attenuation by 0.1 dB step

Phase delay characterization of the feedback

We first characterized the response of the optomechanical system to the feedback by varying the phase delay of the feedback loop. For this characterization we used the FFM of a microtoroid with a resonance frequency $\Omega_m/2\pi = 5.48$ MHz, such that a series of three coaxial delays with a maximum delay time of 63.5 ns each allowed us to shift the feedback signal by a full mechanical oscillation period. The resonator motion was probed by a coherent field with a power of 10 μW whose phase quadrature fluctuations were subsequently measured on a balanced homodyne detector with a LO power of 10 mW, providing a high clearance to the electronic noise (15 dB). The proper balancing and shot noise limited behavior of the homodyne detector over a sideband frequency range covering the mechanical resonance was verified by the linear scaling of the optical noise spectral variance with optical power, in the absence of optomechanical coupling. The visibility of the interferences at the homodyne detector reached 98%, introducing 4% of detection loss. The optical cavity was driven on resonance, and in the undercoupled regime with $\eta = 0.14$. No electrical frequency filters were used in addition to the frequency filters included in the electronics of the optical detectors, such that the electrical bandwidth of the feedback loop was limited by the homodyne detector bandwidth. The feedback gain was adjusted in order to prevent saturation of the electrical amplifiers by unfiltered parasitic signals from mechanical resonances within the detection bandwidth. The DC bias voltage applied to the electrodes was 300 V, and the tip of the sharp electrode was placed approximately 10 μm above the center of the microtoroid.

Figure 4.8 shows the PSD of the in-loop position measurement as a function of feedback delay time. The feedback gain is set to $G_{fb} = 9.5$, except for feedback delay phase from $\Omega_m\tau_{fb}/2\pi = 0.58$ to $\Omega_m\tau_{fb}/2\pi = 0.97$ (modulo 2π) where it is reduced to avoid saturation of the feedback. The behavior of the feedback actuated resonator with increasing feedback delay time follows the expected behavior described by Equations (4.30) and (4.31). At $\Omega_m\tau_{fb} = 0$ the feedback force drives the mechanical oscillator in phase with its oscillations, what softens its effective spring constant and reduces its resonance frequency. The opposite behavior is observed when $\Omega_m\tau_{fb} = \pi$, as the feedback force is applied in opposite phase, and consequently stiffens the effective spring constant of the resonator and increases its resonance frequency. Damping or amplification of the mechanical motion is respectively achieved by delaying or advancing the phase of the feedback force by one quarter of the oscillation period, i.e. $\Omega_m\tau_{fb} = \pm\pi/2 \pmod{2\pi}$.

Frequency tuning of a microtoroid FFM

We investigated the frequency tuning capability of our feedback actuation scheme by varying the feedback gain while keeping a constant feedback phase delay around $\Omega_m\tau_{fb} \sim$

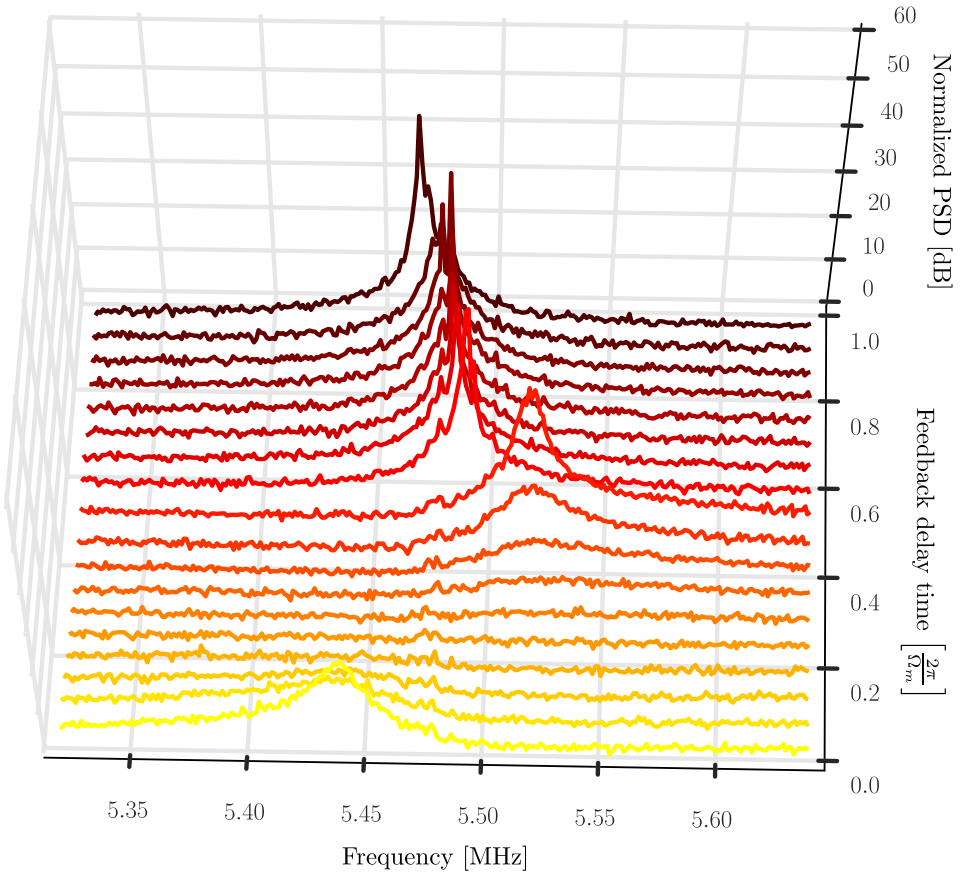

FIGURE 4.8: PSD of the in-loop position measurement as a function of feedback delay time. The PSD are normalized to the shot noise level. With increasing feedback delay times the FFM of the microtoroid is successively spring-softened ($\Omega_m\tau_{fb} = 0$), damped ($\Omega_m\tau_{fb} = \pi/2$), spring-hardened ($\Omega_m\tau_{fb} = \pi$), and amplified ($\Omega_m\tau_{fb} = 3\pi/2$). From $\Omega_m\tau_{fb}/2\pi = 0.58$ to $\Omega_m\tau_{fb}/2\pi = 0.97$, the feedback gain is reduced to prevent saturation within the feedback loop.

π. Figure 4.9(a) shows the PSD of the in-loop position measurements fitted with curves described by Equation (4.42). The correlations between the measurement noise and the feedback noise cause a squashing of the measurement noise below the shot noise level. The fitted curves overestimate the noise reduction due to the assumption in Equation (4.42) that measurement noise and feedback noise are completely correlated. In practice however, amplifiers in the feedback loop add electronic noise which is not correlated with the measurement noise. Furthermore, long feedback delay times may degrade the noise correlations. Note that the electronic noise generated within the feedback loop is not the electronic noise plotted on Figure 4.9(a), which comes from the measurement only and is too weak to cause the observed deviation between the measured PSD and the fitted curves.

From the fit, we extracted the effective resonance frequency and damping rate of the FFM, which are plotted on Figures 4.9(b) and 4.9(c) as a function of feedback gain.

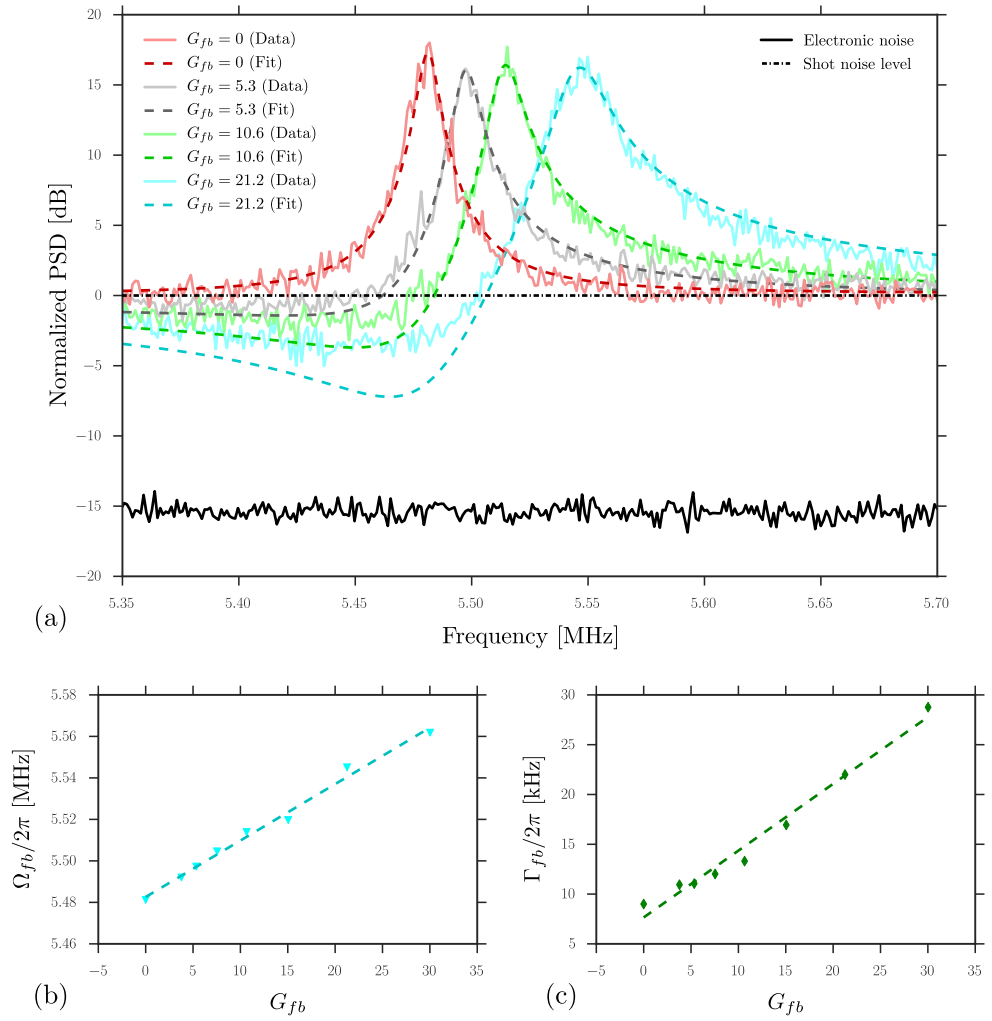

FIGURE 4.9: (a) PSD of the in-loop position measurement at various feedback gains for a fixed feedback phase delay $\Omega_m \tau_f b = 0.96\pi$. The PSD are normalized to the shot noise level. The electronic noise from the detection and acquisition of the PSD lies 15 dB below the shot noise level, and is therefore negligible. Measurement data are fitted by curves described by Equation (4.42) (dashed lines). The effective resonance frequency (b) and the effective mechanical damping (c) of the FFM as a function of feedback gain are extracted from the fitted curves. A linear regression on both sets of extracted values provide an accurate calibration of the feedback delay time.

For the analysis of our data we assumed a feedback transfer function in the form,

$$K_{fb}(\Omega) = \Gamma_m \Omega_m G_{fb} e^{i\Omega\tau_{fb}} \ . \tag{4.50}$$

For low feedback gain relative to the Q factor of the mechanical mode ($G_{fb} \ll Q_m$), the deviation of the effective resonance frequency from the natural resonance frequency of the mechanical resonator is approximately proportional to the feedback gain, i.e. $\Omega_{fb} - \Omega_m \propto G_{fb}$ (cf. Equation 4.30). We applied a linear regression to the effective resonance frequency and damping rate as a function of feedback gain in order to evaluate

the phase delay of the feedback. A value of $\Omega_m \tau_{fb}/2\pi = 0.48$ is obtained, what matches well the expected value of $\Omega_m \tau_{fb}/2\pi \sim 0.5$, thereby confirming the validity of our model and allowing a fine calibration of the feedback delay time.

Our feedback actuation setup allows the tuning of the effective mechanical resonance frequency within ±1.4% of the natural resonance frequency. For the FFM at 5.48 MHz, the tuning range covers ±80 kHz, what is one order of magnitude higher than the width of the mechanical resonance ($\Gamma_m \approx 9$ kHz).

Cold damping of a microtoroid FFM

By setting the feedback phase delay to $\pi/2$, we were able to damp the motion of the mechanical oscillator, and thereby to cool its effective temperature. In-loop measurements of the resonator displacement resulted in the power spectra shown on Figure 4.10(a). A reduction of the peak amplitude of the FFM oscillations is observed for increasing feedback gains. For feedback gains larger than the SNR ($G_{fb} > \text{SNR}$) the measurement noise is squashed below the shot noise level, leading to the expected inverse Lorentzian spectrum. The mean resonance frequency of the FFM, extracted from Lorentzian fits to the PSD, is $\Omega_m = 5.480 \pm 0.002$ MHz, and the effective damping rate is plotted on Figure 4.10(b) as a function of the feedback power gain. In practice we controlled the gain of the feedback loop with a series of electrical power attenuators that does not provided us with a direct calibration of the feedback gain G_{fb}. The calibration was obtained by a fit to the effective damping rates (dashed line in Figure 4.10(b)), assuming $\Gamma_{fb} = \Gamma_m(1 + G_{fb})$.

We inferred the in-loop temperatures by plugging the Lorentzian fit parameters into Equation (4.44), and compared with the theoretical in-loop temperatures given by Equation 4.45 (red dots and dashed line in Figure 4.10(c), respectively). The out-of-loop temperatures were derived from both the inferred and theoretical in-loop temperatures by using Equation 4.46 (blue squares and dashed line in Figure 4.10(c)). The inferred in-loop temperatures are in good agreement with the calculated ones, what suggests that a minimum effective temperature around $T_{min} = 58.8$ K (corresponding to SNR = 82.3 in the absence of feedback actuation) was reached for a feedback gain $G_{fb} = 8.1$. Further characterization of the feedback transfer function, with an alternative calibration of the feedback gain from the SNR of the measured PSD, may improve the accuracy of the estimate of the effective cooling temperature from in-loop measurements.

With an available feedback gain $G_{fb} = 30$, our feedback actuation setup could in principle cool the FFM from room temperature to a temperature of 18.6 K, given an SNR without feedback in the order of a thousand. The later can easily be achieved by a tenfold increase of the probe power while keeping the same experimental conditions. Other ways of increasing the SNR have been discussed in the previous chapters, e.g.

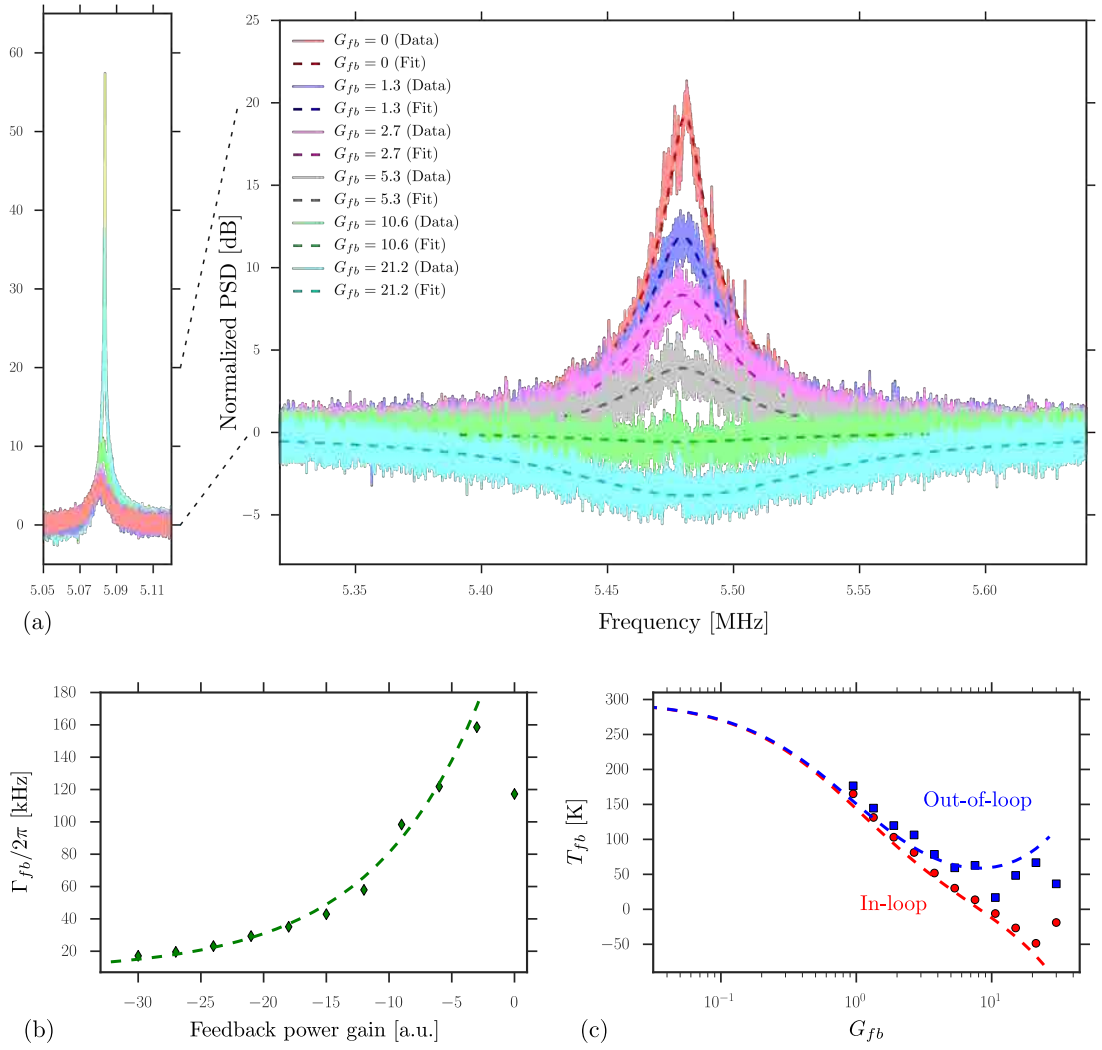

FIGURE 4.10: (a) PSD of the in-loop position measurement at various feedback gains for a fixed feedback phase delay $\Omega_m \tau_f b = \pi/2$. The PSD are normalized to the shot noise level. Measurement data are fitted with Lorentzian functions (dashed lines). (b) Effective mechanical damping of the FFM as a function of feedback power gain, obtained from the Lorentzian fits. A fit to the effective damping rates, $\Gamma_{fb} = \Gamma_m(1 + G_{fb})$, provides a calibration of the feedback gain G_{fb}. (c) Inferred (markers) and calculated (dashed lines) in-loop (red) and out-of-loop (blue) temperature of the FFM as a function of feedback gain G_{fb}. The inferred temperatures follow the evolution of the theoretical calculations until a high feedback gain $G_{fb} = 30$ is reached. From there the feedback loop is saturated by the signal measured from the nearby first crown mode of the microtoroid (yellow line on the left panel in (a)), which is amplified rather than cooled.

squeezing the probe field. However, the amplification of the nearby first crown mode of the microtoroid, shown on the left panel of Figure 4.10(a) provokes the saturation of the feedback loop at high gains, what prevents further cooling of the FFM.

Filtering of parasitic modes

In order to prevent the saturation of the feedback loop due to the feedback heating of neighboring mechanical modes of our microtoroid, we placed a narrow home-built bandpass filter[14] after the detection stage of the feedback loop. We chose to use a Bessel filter to maintain a constant time delay of the feedback signal in the passband. The passband was restricted to the signal produced by the FFM motion such that parasitic signals from neighboring modes are strongly attenuated. In this way we succeeded in suppressing the influence of the feedback on neighboring modes, but we also affected the feedback actuation of the FFM. In fact, as the mode is cooled by increasing the effective damping rate, its resonance width spreads and reaches the limits of the filter passband resulting in the behavior shown on Figure 4.11. Beyond the cutoff frequencies of the bandpass filter the signal is attenuated therefore the feedback actuation force does not follow the complete motion of the resonator and cannot damp it further. Additionally the large phase shift introduced by the filter near the cutoff frequencies alters the synchronization of the feedback force with the mechanical oscillations. Interestingly, attempting to cool the mechanical oscillator seems to bring it into an unstable state where small variations of the feedback delay time (< 1 ns) causes large variations of its oscillation frequency, on the order of 3% of the resonance frequency. Further investigation is required to characterize completely this behavior, with e.g. a simulation of the feedback using the transfer function of the bandpass filter. The ingenious design of the feedback control transfer function may provide a greater control over the motion of the microresonator.

4.3 Conclusion and outlook

In this chapter we have investigated theoretically and experimentally the use of dielectric gradient forces to control the motion of a micromechanical resonator. This work was sparked by the great interest in cooling the motion of a macroscopic oscillator into its quantum ground state, but also explored the capability provided by strong actuation forces in tuning the frequency and amplitude of mechanical oscillations.

In the first part of this chapter we described theoretically the physical mechanism giving rise to electrical forces within dielectric materials. We modeled the generation of dielectric gradient forces by applying an electric field across a dielectric body. In our work we considered the electric field to be produced between two point electrodes with opposite charges, what resembles the configuration of our experimental setup. It would be interesting to study more advanced design that could allow a precise control over the spatial distribution of the dielectric gradient forces, such as to address vibrational modes individually. By this mean, strongly driving a specific mechanical mode would require

[14] 5^{th} order Bessel filter with a 100 kHz bandwidth centered at 5.5 MHz.

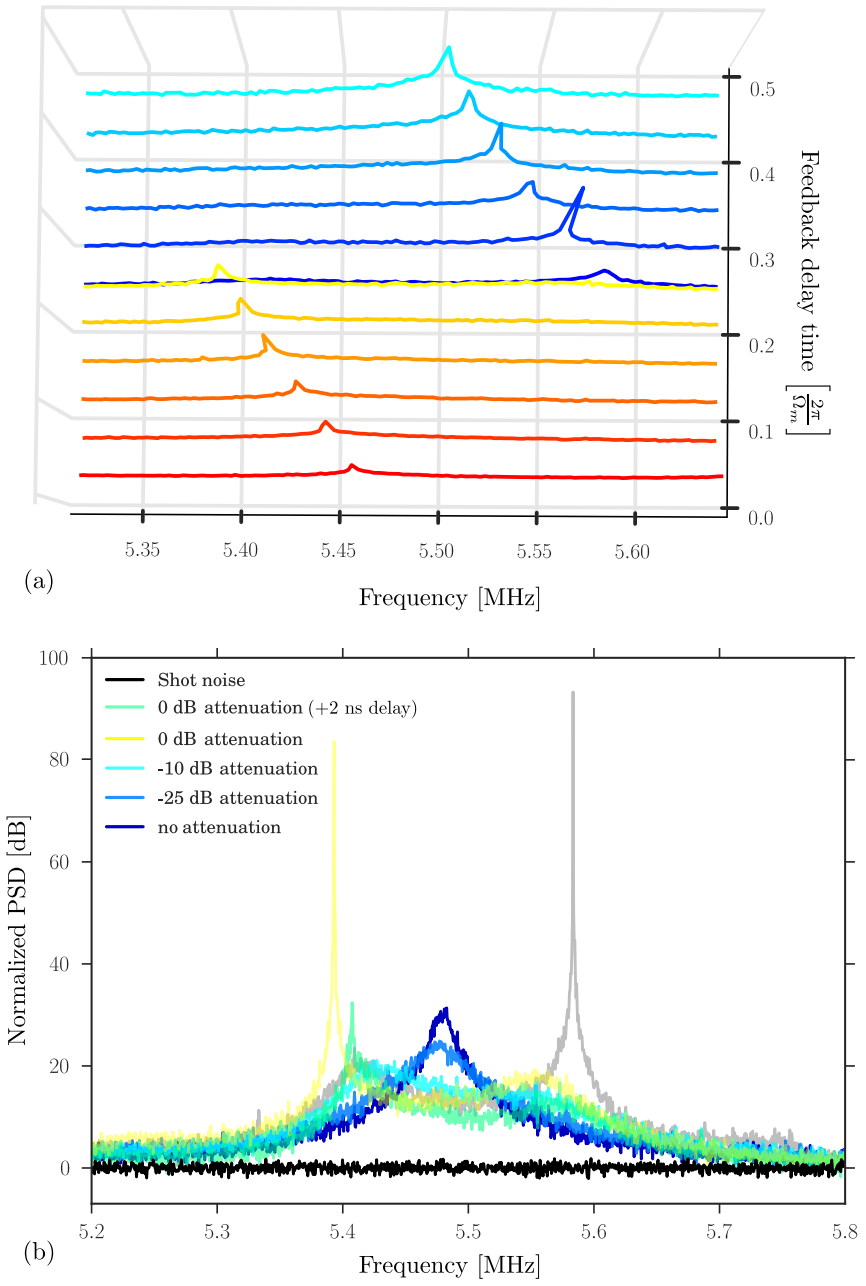

FIGURE 4.11: PSD of in-loop position measurements at a fixed gain and various feedback delay times (a), and at various feedback gains with a fixed feedback phase delay $\Omega_m \tau_f b = \pi/2$ (b). All PSD are normalized to the shot noise level. The feedback signal is filtered by a sharp 5^{th} order Bessel filter with a 100 kHz bandwidth centered at 5.5 MHz in order to suppress the actuation of mechanical modes other than the FFM. Due to the narrowness and sharpness of the filter, the feedback actuation force does not follow linearly the motion of the oscillator for effective damping rates larger than the filter bandwidth. Consequently the power spectrum the oscillator position looses its Lorentzian shape.

less electrical power, which means a lower DC bias voltage or AC drive voltage. High gains could thus be achieved in a feedback actuation setup with the use of less electrical amplifier stages, which are prone to saturation. Additionally the selective actuation of specific vibrational mode prevents other modes to be amplified and to saturate the feedback loop. The spatial profile of the dielectric gradient force field for different design of the electrode configuration, or alternative electric field generation schemes, can be investigated with FEM simulations, if not analytically.

In the second part of the chapter we presented the theoretical framework of feedback actuation control of mechanical resonators. We modeled the feedback loop as a succession of processes such as optomechanical transduction and optical quadrature detection. We investigated the contribution of each process to the feedback in terms of bandwidth, gain and phase response, in order to combine and describe the action of the feedback with a simplified transfer function. We confronted our theoretical model to the reality of experiments and showed a good agreement between our expectations and the behavior of a single feedback-actuated FFM of a microtoroid resonator. By controlling the phase delay and the gain of the feedback loop, we were able to either spring-soften, spring-harden, damp or amplify the mechanical oscillations. We demonstrated electrical feedback cooling of the FFM down to 58.8 K from room temperature. The cooling was limited by the SNR of our in-loop displacement measurement as we observed the distinctive squashing of the measurement noise caused by correlations with the feedback noise. The gain of the feedback loop was ultimately limited by the saturation of electrical amplifiers caused by the feedback-induced amplification of mechanical modes in close spectral proximity to the FFM. We prevented the undesired amplification of mechanical oscillations by limiting the feedback bandwidth with sharp electrical frequency filters. However the spectral broadening of the damped FFM became also limited by the filter bandwidth, and the large phase shift introduced near the cutoff frequency gave rise to an unstable behavior of the feedback loop.

We propose a few lines of investigation to overcome the limitations of our electrical feedback actuation scheme. The feedback actuation scheme should be applied to a mechanical mode well separated in frequency from other mechanical resonances of the microresonator, such that the latter could be filtered out of the feedback while preserving the full resonance of the actuated mode. This solution requires the proper design and fabrication of a microresonator, and seems realizable with current technologies. Alternatively the spectral separation between mechanical modes could also be such that tuning the phase delay to damp one mode does not provoke the amplification of another mode. This solution involves less the design and fabrication of the microresonator, than the design and building of the feedback transfer function. We must also point out a major limitation to cold damping of a mechanical oscillator from room temperature.

Given a mechanical mode with resonance frequency $\Omega_m/2\pi = 5.48$ MHz, reaching a ground state probability of 50% (i.e. an average occupancy of one phonon) corresponds to cooling the mechanical mode to an effective temperature $T_{50\%} = \ln(2)\hbar\Omega_m/k_B \approx 0.18$ mK. Accessing such a low temperature from room temperature ($T_{rm} = 300$ K) requires a feedback gain $G_{fb} \approx 2T_{rm}/T_{50\%} \approx 3.3 \cdot 10^6$ which is five orders of magnitude larger than what we achieved in our experiments. The sensitivity of the displacement measurement must also be improved to provide a sufficient SNR. Eventually, the main limitation to ground state cooling from room temperature comes from the feedback-induced spectral broadening of the damped mechanical mode. Assuming a modest damping rate $\Gamma_m = 1$ kHz at room temperature, the width of the mechanical resonance should broaden over several gigahertz to achieve ground state cooling, thus the feedback gain and phase delay should be uniform over a large bandwidth. An alternative solution to a high feedback bandwidth would be to improve the intrinsic quality factor of the mechanical mode to values higher than the required feedback gain, but such high values, over a million, have never been observed with microresonators. In regards of the technical challenges listed above we believe that feedback cooling to the ground state from room temperature is not realizable with current technologies as it imposes extreme requirements on the microresonator properties and feedback design. Therefore it appears essential to combine cold damping with another cooling scheme, such as cryogenic cooling in an Helium bath [123], in order to reach ground state temperatures.

Bibliography

[1] M. Bahrami, M. Paternostro, A. Bassi, and H. Ulbricht. Proposal for a noninterferometric test of collapse models in optomechanical systems. *Physical Review Letters*, 112:210404, 2014. URL **http://dx.doi.org/10.1103/PhysRevLett.112.210404**.

[2] Stefan Nimmrichter, Klaus Hornberger, and Klemens Hammerer. Optomechanical sensing of spontaneous wave-function collapse. *Phys. Rev. Lett.*, 113:020405, 2014. URL **http://dx.doi.org/10.1103/PhysRevLett.113.020405**.

[3] V. Pikovski, M. R. Vanner, M. Aspelmeyer, M. S. Kim, and C. Brukner. Probing planck-scale physics with quantum optics. *Nature Physics*, 8:393 –397, 2012. URL **http://dx.doi.org/10.1038/nphys2262**.

[4] K. Stannigel, P. Rabl, A. S. Sørensen, P. Zoller, and M. D. Lukin. Optomechanical transducers for long-distance quantum communication. *Phys. Rev. Lett.*, 105: 220501, 2010. URL **http://dx.doi.org/10.1103/PhysRevLett.105.220501**.

[5] V. B. Braginsky. Classical and quantum restrictions on the detection of weak disturbances of a macroscopic oscillator. *Soviet Physics Journal of Experimental and Theoretical Physics*, 53:1434 –1441, 1967.

[6] V. B. Braginsky and A. B. Manukin. Ponderomotive effects of electromagnetic radiation. *Soviet Physics Journal of Experimental and Theoretical Physics*, 52:986 –989, 1967.

[7] C. Caves. Quantum-mechanical radiation-pressure fluctuations in an interferometer. *Physical Review Letters*, 45:75 –78, 1980. URL **http://dx.doi.org/10.1103/PhysRevLett.45.75**.

[8] V. B. Braginsky and F. Ya. Khalili. *Quantum Measurement*. Cambridge University Press, 1992.

[9] D. Leibfried, R. Blatt, C. Monroe, and D. J. Wineland. Quantum dynamics of single trapped ions. *Reviews of Modern Physics*, 75:281 –324, 2003. URL **http://dx.doi.org/10.1103/RevModPhys.75.281**.

[10] V. B. Braginsky, M. L. Gorodetsky, and V. S. Ilchenko. Quality-factor and nonlinear properties of optical whispering-gallery modes. *Physics Letters A*, 137(7, 8): 393 –397, 1989. URL **http://dx.doi.org/10.1016/0375-9601(89)90912-2**.

[11] V. S. Ilchenko and M. L. Gorodetsky. Thermal nonlinear effects in optical whispering gallery microresonators. *Laser Physics*, 2(6):1004 –1009, 1999.

[12] T. Carmon, L. Yang, and K. J. Vahala. Dynamical thermal behavior and thermal self-stability of microcavities. *Optics Express*, 12(20):4742 –4750, 2004. URL **http://dx.doi.org/10.1364/OPEX.12.004742**.

[13] T. J. Kippenberg, S. M. Spillane, and K. J. Vahala. Kerr-nonlinearity optical parametric oscillation in an ultrahigh-q toroid microcavity. *Physics Review Letters*, 93(8):083904, 2004. URL **http://dx.doi.org/10.1103/PhysRevLett.93.083904**.

[14] Q. P. Unterreithmeier, E. M. Weig, and J. P. Kotthaus. Universal transduction scheme for nanomechanical systems based on dielectric forces. *Nature*, 458:1001 –1004, 2009. URL **http://dx.doi.org/10.1038/nature07932**.

[15] U. B. Hoff, G. I. Harris, L. S. Madsen, H. Kerdoncuff, M. Lassen, B. M. Nielsen, W. P. Bowen, and U. L. Andersen. Quantum-enhanced micromechanical displacement sensitivity. *Optics Letters*, 38(9):1413 –1415, 2013. URL **http://dx.doi.org/10.1364/OL.38.001413**.

[16] H. Kerdoncuff, U. B. Hoff, G. I. Harris, W. P. Bowen, and U. L. Andersen. Squeezing-enhanced measurement sensitivity in a cavity optomechanical system. *Annalen der Physik*, 527:107 –114, 2015. URL **http://dx.doi.org/10.1002/andp.201400171**.

[17] T. G. McRae, K. H. Lee, G. I. Harris, J. Knittel, and W. P. Bowen. Cavity optoelectromechanical system combining strong electrical actuation with ultrasensitive transduction. *Physical Review A*, 82:023825, 2010. URL **http://dx.doi.org/10.1103/PhysRevA.82.023825**.

[18] K. H. Lee, T. G. McRae, G. I. Harris, J. Knittel, and W. P. Bowen. Cooling and control of a cavity optoelectromechanical system. *Physical Review Letters*, 104: 123604, 2010. URL **http://dx.doi.org/10.1103/PhysRevLett.104.123604**.

[19] L. Mandel and E. Wolf. *Optical coherence and quantum optics*. Cambridge University Press, 1995.

[20] H.-A. Bachor and T. C. Ralph. *A Guide to Experiments in Quantum Optics*. Wiley-VCH, 2004.

[21] C. Gerry and P. Knight. *Introductory Quantum Optics*. Cambridge University Press, 2005.

[22] D. F. Walls and G. J. Milburn. *Quantum Optics, Second Edition*. Springer-Verlag Berlin Heidelberg, 2008.

[23] B. E. A. Saleh and M. C. Teich. *Fundamentals of Photonics, Second Edition*. John Wiley & Sons, Inc, 2007.

[24] R. W. Boyd. *Nonlinear Optics, Third Edition*. Academic Press, 2008.

[25] M. Abramowitz and I. A. Stegun. *Handbook of Mathematical Functions with Formulas, Graphs, and Mathematical Tables*. Dover Publications, 1964.

[26] P. A. M. Dirac. *The Principles of Quantum Mechanics*. Oxford University Press, 1930.

[27] H. M. Wiseman and G. J. Milburn. *Quantum Measurement and Control*. Cambridge University Press, 2010.

[28] M. Aspelmeyer, T. J. Kippenberg, and F. Marquardt. Cavity optomechanics. *Reviews of Modern Physics*, 86:1391 –1452, 2014. URL **http://dx.doi.org/10.1103/RevModPhys.86.1391**.

[29] D. Kleckner and D. Bouwmeester. Sub-kelvin optical cooling of a micromechanical resonator. *Nature*, 444:75 –78, 2006. URL **http://dx.doi.org/10.1038/nature05231**.

[30] O. Arcizet, P.-F. Cohadon, T. Briant, M. Pinard, A. Heidmann, J.-M. Mackowski, C. Michel, L. Pinard, O. Français, and L. Rousseau. High-sensitivity optical monitoring of a micromechanical resonator with a quantum-limited optomechanical sensor. *Physical Review Letters*, 97:133601, 2006. URL **http://dx.doi.org/10.1103/PhysRevLett.97.133601**.

[31] S. Gröblacher, K. Hammerer, M. R. Vanner, and M. Aspelmeyer. Observation of strong coupling between a micromechanical resonator and an optical cavity field. *Nature*, 460:724 –727, 2009. URL **http://dx.doi.org/10.1038/nature08171**.

[32] J. D. Thompson, B. M. Zwick, A. M. Jayich, F. Marquardt, S. M. Girvin, and J. G. E. Harris. Strong dispersive coupling of a high-finesse cavity to a micromechanical membrane. *Nature*, 452:72 –75, 2008. URL **http://dx.doi.org/10.1038/nature06715**.

[33] T. P. Purdy, R. W. Peterson, and C. A. Regal. Observation of radiation pressure shot noise on a macroscopic object. *Science*, 339:801 –804, 2013. URL **http://dx.doi.org/10.1126/science.1231282**.

[34] T. Bagci, A. Simonsen, S. Schmid, L. G. Villanueva, E. Zeuthen, J. Appel, J. M. Taylor, A. Sørensen, K. Usami, A. Schliesser, and E. S. Polzik. Optical detection of radio waves through a nanomechanical transducer. *Nature*, 507:81 –85, 2014. URL **http://dx.doi.org/10.1038/nature13029**.

[35] A. Sawadsky, H. Kaufer, R. M. Nia, S. P. Tarabrin, F. Ya. Khalili, K. Hammerer, and R. Schnabel. Observation of generalized optomechanical coupling and cooling on cavity resonance. *Physical Review Letters*, 114:043601, 2015. URL **http://dx.doi.org/10.1103/PhysRevLett.114.043601**.

[36] M. Eichenfield, J. Chan, R. M. Camacho, K. J. Vahala, and O. Painter. Optomechanical crystals. *Nature*, 462:78 –82, 2009. URL **http://dx.doi.org/10.1038/nature08524**.

[37] J. Chan, T. P. M. Alegre, A. H. Safavi-Naeini, J. T. Hill, A. Krause, S. Gröblacher, M. Aspelmeyer, and O. Painter. Laser cooling of a nanomechanical oscillator into its quantum ground state. *Nature*, 478:89 –92, 2013. URL **http://dx.doi.org/10.1038/nature10461**.

[38] G. Anetsberger, O. Arcizet, Q. P. Unterreithmeier, R. Rivière, A. Schliesser, E. M. Weig, J. P. Kotthaus, and T. J. Kippenberg. Near-field cavity optomechanics with nanomechanical oscillators. *Nature Physics*, 5:909 –914, 2009. URL **http://dx.doi.org/10.1038/nphys1425**.

[39] E. Verhagen, S. Deléglise, S. Weis, A. Schliesser, and T. J. Kippenberg. Quantum-coherent coupling of a mechanical oscillator to an optical cavity mode. *Nature*, 482:63 –67, 2012. URL **http://dx.doi.org/10.1038/nature10787**.

[40] J. D. Teufel, T. Donner, M. A. Castellanos-Beltran, J. W. Harlows, and K. W. Lehnert. Nanomechanical motion measured with an imprecision below that at the standard quantum limit. *Nature Nanotechnology*, 4:820 –823, 2009. URL **http://dx.doi.org/10.1038/nnano.2009.343**.

[41] A. D. O'Connell, M. Hofheinz, M. Ansmann, R. D. Bialczak, M. Lenander, E. Lucero, M. Neeley, D. Sank, H. Wang, M. Weides, J. Wenner, J. M. Martinis, and A. N. Cleland. Quantum ground state and single-phonon control of a mechanical resonator. *Nature*, 464:697 –703, 2010. URL **http://dx.doi.org/10.1038/nature08967**.

[42] J. D. Teufel, T. Donner, D. Li, J. W. Harlows, M. S. Allman, K. Cicak, A. J. Sirois, J. D. Whittaker, K. W. Lehnert, and R. W. Simmonds. Sideband cooling of micromechanical motion to the quantum ground state. *Nature*, 475:359 –363, 2011. URL **http://dx.doi.org/10.1038/nature10261**.

[43] H. A. Haus. *Waves and Fields in Optoelectronics*. Prentice-Hall, 1984.

[44] S. M. Spillane, T. J. Kippenberg, and K. J. Vahala. Ultralow-threshold raman laser using a spherical dielectric microcavity. *Nature*, 415:621 –623, 2002. URL **http://dx.doi.org/10.1038/415621a**.

[45] F. Treussart, V. S. Ilchenko, J.-F. Roch, J. Hare, V. Lefèvre-Seguin, J.-M. Raimond, and S. Haroche. Evidence for intrinsic kerr bistability of high-q microsphere resonators in superfluid helium. *European Physical Journal D*, 1:235 –238, 1998. URL **http://dx.doi.org/10.1007/s100530050087**.

[46] R. W. P. Drever, J. L. Hall, F. V. Kowalski, J. Hough, G. M. Ford, A. J. Munley, and H. Ward. Laser phase and frequency stabilization using an optical resonator. *Applied Physics B*, 31(2):97 –105, 1983. URL **http://dx.doi.org/10.1007/BF00702605**.

[47] E. D. Black. An introduction to pound–drever-hall laser frequency stabilization. *American Journal of Physics*, 69(1):79 –87, 2001. URL **http://dx.doi.org/10.1119/1.1286663**.

[48] A. N. Oraevsky. Whispering-gallery waves. *Quantum Electronics*, 32:377, 2002. URL **http://dx.doi.org/10.1070/QE2002v032n05ABEH002205**.

[49] F. Cap and R. Deutsch. Toroidal resonators for electromagnetic waves. *IEEE Transactions on Microwave Theory and Techniques*, 26:478 – 486, 1978. URL **http://dx.doi.org/10.1109/TMTT.1978.1129419**.

[50] F. Cap and R. Deutsch. Toroidal resonators for electromagnetic waves–ii. *IEEE Transactions on Microwave Theory and Techniques*, 28:700 – 703, 1980. URL **http://dx.doi.org/10.1109/TMTT.1980.1130151**.

[51] M. S. Janaki and B. Dasgupta. Eigenmodes for electromagnetic waves propagating in a toroidal cavity. *IEEE Transactions on Plasma Science*, 18:78 –85, 1990. URL **http://dx.doi.org/10.1109/27.45509**.

[52] M. L. Gorodetsky and A. E. Fomin. Geometrical theory of whispering-gallery modes. *IEEE Journal of Selected Topics in Quantum Electronics*, 12:33 – 39, 2006. URL **http://dx.doi.org/10.1109/JSTQE.2005.862954**.

[53] Vladimir S. Ilchenko, Michael L. Gorodetsky, X. Steve Yao, and Lute Maleki. Microtorus: a high-finesse microcavity with whispering-gallery modes. *Optics Letters*, 26(5):256 –258, 2001. URL **http://dx.doi.org/10.1364/OL.26.000256**.

[54] M. Oxborrow. Traceable 2-d finite-element simulation of the whispering-gallery modes of axisymmetric electromagnetic resonators. *IEEE Transactions on Microwave Theory and Techniques*, 55:1209 –1218, 2007. URL **http://dx.doi.org/10.1109/TMTT.2007.897850**.

[55] M. J. Weber. *Handbook of optical materials*. CRC Press, 2003.

[56] A. Serpengüzel, S. Arnold, , and G. Griffel. Excitation of resonances of microspheres on an optical fiber. *Optics letters*, 20(7):654 –656, 1995. URL **http://dx.doi.org/10.1364/OL.20.000654**.

[57] N. Dubreuil, J. C. Knight, D. K. Leventhal, V. Sandoghar, J. Hare, and V. Lefèvre. Eroded monomode optical fiber for whispering-gallery mode excitation in fused-silica microspheres. *Optics letters*, 20(8):813 –815, 1995. URL **http://dx.doi.org/10.1364/OL.20.000813**.

[58] G. Griffel, S. Arnold, D. Taskent, A. Serpengüzel, J. Connolly, and N. Morris. Morphology-dependent resonances of a microsphere–optical fiber system. *Optics letters*, 21(10):695 –697, 1996. URL **http://dx.doi.org/10.1364/OL.21.000695**.

[59] J. C. Knight, G. Cheung, F. Jacques, and T. A. Birks. Phase-matched excitation of whispering-gallery-mode resonances by a fiber taper. *Optics letters*, 22(15):1129 –1131, 1997. URL **http://dx.doi.org/10.1364/OL.22.001129**.

[60] M. L. Gorodetsky and V. S. Ilchenko. Optical microsphere resonators: optimal coupling to high-q whispering-gallery modes. *Journal of the Optical Society of America B*, 16(1):147 –154, 1999. URL **http://dx.doi.org/10.1364/JOSAB.16.000147**.

[61] S. M. Spillane, T. J. Kippenberg, O. J. Painter, and K. J. Vahala. Ideality in a fiber-taper-coupled microresonator system for application to cavity quantum electrodynamics. *Physical Review Letters*, 91:043902, 2003. URL **http://dx.doi.org/10.1103/PhysRevLett.91.043902**.

[62] Allan W. Snyder and John D. Love. *Optical Waveguide Theory*. Chapman and Hall, 1983.

[63] H. Haus, W. Huang, S. Kawakami, and N. Whitaker. Coupled-mode theory of optical waveguides. *Journal of Lightwave Technology*, 5(1):16 –23, 1987. URL **http://dx.doi.org/10.1109/JLT.1987.1075416**.

[64] B.E. Little, J.-P. Laine, and H.A. Haus. Analytic theory of coupling from tapered fibers and half-blocks into microsphere resonators. *Journal of Lightwave Technology*, 17(4):704 –715, 1999. URL **http://dx.doi.org/10.1109/50.754802**.

[65] Y. Lu, J.-Y. Wang, X.-X. Xu, S.-H. Pan, and C.-Z. Zhang. Optimal conditions of coupling between the propagating mode in a tapered fiber and the given wg mode in a high-q microsphere. *Optik - International Journal for Light and Electron Optics*, 112(3):109 –113, 2001. URL **http://dx.doi.org/10.1078/0030-4026-00017**.

[66] T. W. Hänsch and B. Couillaud. Laser frequency stabilization by polarization spectroscopy of a reflecting reference cavity. *Optics Communications*, 35(3):441 –444, 1980. URL **http://dx.doi.org/10.1016/0030-4018(80)90069-3**.

[67] M. G. Littman and H. J. Metcalf. Spectrally narrow pulsed dye laser without beam expander. *Applied Optics*, 17(14):2224 –2227, 1978. URL **http://dx.doi.org/10.1364/AO.17.002224**.

[68] S.-X. Qian and R. K. Chang. Multiorder stokes emission from micrometer-size droplets. *Physics Review Letters*, 56:926 –929, 1986. URL **http://link.aps.org/doi/10.1103/PhysRevLett.56.926**.

[69] A. J. Campillo, J. D. Eversole, and H.-B. Lin. Cavity quantum electrodynamic enhancement of stimulated emission in microdroplets. *Physics Review Letters*, 67 (4):437 –440, 1991. URL **http://dx.doi.org/10.1103/PhysRevLett.67.437**.

[70] S. Uetake, M. Katsuragawa, M. Suzuki, and K. Hakuta. Stimulated raman scattering in a liquid-hydrogen droplet. *Physical Review A*, 61:011803, 1999. URL **http://link.aps.org/doi/10.1103/PhysRevA.61.011803**.

[71] T.J. Kippenberg, S.M. Spillane, B. Min, and K.J. Vahala. Theoretical and experimental study of stimulated and cascaded raman scattering in ultrahigh-q optical microcavities. *IEEE Journal of Selected Topics in Quantum Electronics*, 10(5): 1219–1228, 2004. URL **http://dx.doi.org/10.1109/JSTQE.2004.837203**.

[72] P. Del'Haye, A. Schliesser, O. Arcizet, T. Wilken, R. Holzwarth, and T. J. Kippenberg. Optical frequency comb generation from a monolithic microresonator. *Nature*, 450:1214 –1217, 2007. URL **http://dx.doi.org/10.1038/nature06401**.

[73] H. Rokhsari and K. J. Vahala. Observation of kerr nonlinearity in microcavities at room temperature. *Optics Letters*, 30(4):427 –429, 2005. URL **http://dx.doi.org/10.1364/OL.30.000427**.

[74] Y. Hadjar, P. F. Cohadon, C. G. Aminoff, M. Pinard, and A. Heidmann. High-sensitivity optical measurement of mechanical brownian motion. *Europhysics Letters*, 47(5):545 –551, 1999. URL **http://dx.doi.org/10.1209/epl/i1999-00422-6**.

[75] A. A. Clerk, M. H. Devoret, S. M. Girvin, F. Marquardt, and R. J. Schoelkopf. Introduction to quantum noise, measurement, and amplification. *Reviews of Modern Physics*, 82(2):1155 –1208, 2010. URL **http://dx.doi.org/10.1103/RevModPhys.82.1155**.

[76] A. H. Safavi-Naeini, J. Chan, J. T. Hill, T. P. M. Alegre, A. Krause, and O. Painter. Observation of quantum motion of a nanomechanical resonator. *Physical Review Letters*, 108(3):033602, 2012. URL **http://dx.doi.org/10.1103/PhysRevLett.108.033602**.

[77] A. Schliesser, G. Anetsberger, R. Rivière, O. Arcizet, and T. J. Kippenberg. High-sensitivity monitoring of micromechanical vibration using optical whispering gallery mode resonators. *New Journal of Physics*, 10:095015, 2008. URL **http://dx.doi.org/10.1088/1367-2630/10/9/095015**.

[78] M. Pinard, Y. Hadjar, and A. Heidmann. Effective mass in quantum effects of radiation pressure. *The European Physical Journal D*, 7(1):107 –116, 1999. URL **http://dx.doi.org/10.1007/s100530050354**.

[79] P. Meystre, J. D. McCullen, E. Vignes, and Wright E. M. Theory of radiation-pressure-driven interferometers. *Journal of the Optical Society of America B*, 2 (11):1830 –1840, 1985. URL **http://dx.doi.org/10.1364/JOSAB.2.001830**.

[80] A. Dorsel, J. D. McCullen, P. Meystre, E. Vignes, and H. Walther. Optical bistability and mirror confinement induced by radiation pressure. *Physical Review Letters*, 51:1550 –1553, 1983. URL **http://dx.doi.org/10.1103/PhysRevLett.51.1550**.

[81] C. K. Law. Interaction between a moving mirror and radiation pressure: A hamiltonian formulation. *Physical Review A*, 51:2537 –2541, 1995. URL **http://dx.doi.org/10.1103/PhysRevA.51.2537**.

[82] Vittorio Giovannetti and David Vitali. Phase-noise measurement in a cavity with a movable mirror undergoing quantum brownian motion. *Physical Review A*, 63: 023812, 2001. URL **http://dx.doi.org/10.1103/PhysRevA.63.023812**.

[83] C. Caves. Quantum-mechanical noise in an interferometer. *Physical Review D*, 23: 1693 –1708, 1981. URL **http://dx.doi.org/10.1103/PhysRevD.23.1693**.

[84] D. Rugar, R. Budakian, H. J. Mamin, and B. W. Chui. Single spin detection by magnetic resonance force microscopy. *Nature*, 430:329 –332, 2004. URL **http://dx.doi.org/10.1038/nature02658**.

[85] S. Forstner, S. Prams, J. Knittel, E. D. van Ooijen, J. D. Swaim, G. I. Harris, A. Szorkovszky, W. P. Bowen, and H. Rubinsztein-Dunlop. Cavity optomechanical magnetometer. *Physical Review Letters*, 108:120801, 2012. URL **http://dx.doi.org/10.1103/PhysRevLett.108.120801**.

[86] M. A. Taylor, J. Janousek, V. Daria, J. Knittel, B. Hage, H.-A. Bachor, and W. Bowen. Biological measurement beyond the quantum limit. *Nature Physics*, 7:229 –233, 2013. URL **http://dx.doi.org/10.1038/nphoton.2012.346**.

[87] G. Anetsberger, E. Gavartin, O. Arcizet, Q. P. Unterreithmeier, E. M. Weig, M. L. Gorodetsky, J. P. Kotthaus, and T. J. Kippenberg. Measuring nanomechanical motion with an imprecision below the standard quantum limit. *Physical Review A*, 82:061804, 2010. URL **http://dx.doi.org/10.1103/PhysRevA.82.061804**.

[88] T. Westphal, D. Friedrich, H. Kaufer, K. Yamamoto, S. Goßler, H. Müller-Ebhardt, S. L. Danilishin, F. Ya. Khalili, K. Danzmann, and R. Schnabel. Interferometer readout noise below the standard quantum limit of a membrane. *Physical Review A*, 85:063806, 2012. URL **http://dx.doi.org/10.1103/PhysRevA.85.063806**.

[89] A. H. Safavi-Naeini, S. Gröblacher, J. T. Hill, J. Chan, M. Aspelmeyer, and O. Painter. Squeezed light from a silicon micromechanical resonator. *Nature*, 500:185 –189, 2013. URL **http://dx.doi.org/10.1038/nature12307**.

[90] M. Xiao, L.-A. Wu, and H. J. Kimble. Precision measurement beyond the shot-noise limit. *Physical Review Letters*, 59:278 –281, 1987. URL **http://dx.doi.org/10.1103/PhysRevLett.59.278**.

[91] K. McKenzie, D. A. Shaddock, D. E. McClelland, B. C. Buchler, and P. K. Lam. Experimental demonstration of a squeezing-enhanced power-recycled michelson interferometer for gravitational wave detection. *Physical Review Letters*, 88:231102, 2002. URL **http://dx.doi.org/10.1103/PhysRevLett.88.231102**.

[92] H. Vahlbruch, S. Chelkowski, B. Hage, A. Franzen, K. Danzmann, and R. Schnabel. Demonstration of a squeezed-light-enhanced power- and signal-recycled michelson interferometer. *Physical Review Letters*, 95:211102, 2005. URL **http://dx.doi.org/10.1103/PhysRevLett.95.211102**.

[93] K. Goda, O. Miyakawa, E. E. Mikhailov, S. Saraf, R. Adhikari, K. McKenzie, R. Ward, S. Vass, A. J. Weinstein, and N. Mavalvala. A quantum-enhanced prototype gravitational-wave detector. *Nature Physics*, 4:472 –476, 2008. URL **http://dx.doi.org/10.1038/nphys920**.

[94] T. Eberle, S. Steinlechner, J. Bauchrowitz, V. Händchen, H. Vahlbruch, M. Mehmet, H. Müller-Ebhardt, and R. Schnabel. Quantum enhancement of the zero-area sagnac interferometer topology for gravitational wave detection. *Physical Review Letters*, 104:251102, 2010. URL **http://dx.doi.org/10.1103/PhysRevLett.104.251102**.

[95] The LIGO Scientific Collaboration. A gravitational wave observatory operating beyond the quantum shot-noise limit. *Nature Physics*, 7:962 –965, 2011. URL **http://dx.doi.org/10.1038/nphys2083**.

[96] D. Rugar, C. S. Yannoni, and J. A. Sidles. Mechanical detection of magnetic resonance. *Nature*, 360:563 –566, 1992. URL **http://dx.doi.org/10.1038/360563a0**.

[97] M. Poggio and C. L. Degen. Force-detected nuclear magnetic resonance: recent advances and future challenges. *Nanotechnology*, 21:342001, 2010. URL **http://dx.doi.org/10.1088/0957-4484/21/34/342001**.

[98] H. J. Mamin and D. Rugar. Sub-attonewton force detection at millikelvin temperatures. *Applied Physics Letters*, 79:3358, 2001. URL **http://dx.doi.org/10.1063/1.1418256**.

[99] E. Gavartin, P. Verlot, and T. J. Kippenberg. A hybrid on-chip optomechanical transducer for ultrasensitive force measurements. *Nature Nanotechnology*, 7:509 –514, 2012. URL **http://dx.doi.org/10.1038/nnano.2012.97**.

[100] K. Jensen, K. Kim, and A. Zettl. An atomic-resolution nanomechanical mass sensor. *Nature Nanotechnology*, 3:533 –537, 2008. URL **http://dx.doi.org/10.1038/nnano.2008.200**.

[101] N. Treps, U. Andersen, B. Buchler, P. K. Lam, A. Maître, H.-A. Bachor, and C. Fabre. Surpassing the standard quantum limit for optical imaging using nonclassical multimode light. *Physical Review Letters*, 88:203601, 2002. URL **http://dx.doi.org/10.1103/PhysRevLett.88.203601**.

[102] M Mehmet, S. Ast, T. Eberle, S. Steinlechner, H. Vahlbruch, and R. Schnabel. Squeezed light at 1550 nm with a quantum noise reduction of 12.3 db. *Optics Express*, 19:25763 –25772, 2011. URL **http://dx.doi.org/10.1364/OE.19.025763**.

[103] S. Ast, M Mehmet, and R. Schnabel. High-bandwidth squeezed light at 1550 nm from a compact monolithic ppktp cavity. *Optics Express*, 21:13572 –13579, 2013. URL **http://dx.doi.org/10.1364/OE.21.013572**.

[104] M. Mehmet, H. Vahlbruch, N. Lastzka, K. Danzmann, and R. Schnabel. Observation of squeezed states with strong photon-number oscillations. *Physical Review A*, 81:013814, 2010. doi: 10.1103/PhysRevA.81.013814. URL **http://link.aps.org/doi/10.1103/PhysRevA.81.013814**.

[105] A. Schliesser, R. Rivière, G. Anetsberger, O. Arcizet, and T. J. Kippenberg. Resolved-sideband cooling of a micromechanical oscillator. *Nature Physics*, 4: 415 –419, 2008. URL **http://dx.doi.org/10.1038/nphys939**.

[106] Michael L. G., Andrew D. P., and Vladimir S. I. Rayleigh scattering in high-q microspheres. *Journal of the Optical Society of America B*, 17:1051 –1057, 2000. URL **http://dx.doi.org/10.1364/JOSAB.17.001051**.

[107] T. J. Kippenberg, S. M. Spillane, and K. J. Vahala. Modal coupling in traveling-wave resonators. *Optics Letters*, 27:1669 –1671, 2002. URL **http://dx.doi.org/10.1364/OL.27.001669**.

[108] J. Knittel, J. D. Swaim, D. L. McAuslan, G. A. Brawley, and W. P. Bowen. Rayleigh scattering in high-q microspheres. *Scientific Reports*, 3:2974, 2013. URL **http://dx.doi.org/10.1038/srep02974**.

[109] W. Marshall, C. Simon, R. Penrose, and D. Bouwmeester. Towards quantum superpositions of a mirror. *Physical Review Letters*, 91:130401, 2003. URL **http://dx.doi.org/10.1103/PhysRevLett.91.130401**.

[110] O. Arcizet, R. Rivière, A. Schliesser, G. Anetsberger, and T. J. Kippenberg. Cryogenic properties of optomechanical silica microcavities. *Physical Review A*, 80: 021803, 2009. URL **http://dx.doi.org/10.1103/PhysRevA.80.021803**.

[111] A. Schliesser, O. Arcizet, R. Rivière, G. Anetsberger, and T. J. Kippenberg. Resolved-sideband cooling and position measurement of a micromechanical oscillator close to the heisenberg uncertainty limit. *Nature Physics*, 5:509 –514, 2009. URL **http://dx.doi.org/10.1038/nphys1304**.

[112] M. Poggio, C. L. Degen, H. J. Mamin, and D. Rugar. Feedback cooling of a cantilever's fundamental mode below 5 mk. *Physical Review Letters*, 99:017201, 2007. URL **http://dx.doi.org/10.1103/PhysRevLett.99.017201**.

[113] T. Rocheleau, T. Ndukum, C. Macklin, J. B. Hertzberg, A. A. Clerk, and Schwab K. C. Preparation and detection of a mechanical resonator near the ground state of motion. *Nature*, 463:72 –75, 2010. URL **http://dx.doi.org/10.1038/nature08681**.

[114] T. B. Jones. *Electromechanics of Particles*. Cambridge University Press, 1995.

[115] L. Ding, C. Baker, P. Senellart, A. Lemaitre, S. Ducci, G. Leo, and I. Favero. Wavelength-sized gaas optomechanical resonators with gigahertz frequency. *Applied Physics Letters*, 98:113108, 2011. URL **http://dx.doi.org/10.1063/1.3563711**.

[116] D. J. Wineland and W. M. Itano. Laser cooling of atoms. *Physical Review A*, 20: 1521 –1540, 1979. URL **http://dx.doi.org/10.1103/PhysRevA.20.1521**.

[117] S. Stenholm. The semiclassical theory of laser cooling. *Reviews of Modern Physics*, 58:699 –739, 1986. URL **http://dx.doi.org/10.1103/RevModPhys.58.699**.

[118] F. Marquardt, A. A. Clerk, and S. M. Girvin. Quantum dynamics of single trapped ions. *Journal of Modern Optics*, 55:3329 –3328, 2008. URL **http://dx.doi.org/10.1080/09500340802454971**.

[119] I. Wilson-Rae, N. Nooshi, J. Dobrindt, T. J. Kippenberg, and W. Zwerger. Cavity-assisted backaction cooling of mechanical resonators. *New Journal of Physics*, 10(9):095007, 2008. URL **http://dx.doi.org/10.1088/1367-2630/10/9/095007**.

[120] C. Genes, D. Vitali, P. Tombesi, S. Gigan, and M. Aspelmeyer. Ground-state cooling of a micromechanical oscillator: Comparing cold damping and cavity-assisted cooling schemes. *Physical Review A*, 77:033804, 2008. URL **http://dx.doi.org/10.1103/PhysRevA.77.033804**.

[121] S. Mancini, D. Vitali, and P. Tombesi. Optomechanical cooling of a macroscopic oscillator by homodyne feedback. *Physical Review Letters*, 80:688 –691, 1998. URL **http://dx.doi.org/10.1103/PhysRevLett.80.688**.

[122] P. F. Cohadon, A. Heidmann, and M. Pinard. Cooling of a mirror by radiation pressure. *Physical Review Letters*, 83:3174 –3177, 1999. URL **http://dx.doi.org/10.1103/PhysRevLett.83.3174**.

[123] D. J. Wilson, V. Sudhir, N. Piro, R. Schilling, A. Ghadimi, and T. J. Kippenberg. Measurement-based control of a mechanical oscillator at its thermal decoherence rate. *Nature*, 524:325 –329, 2015. URL **http://dx.doi.org/10.1038/nature14672**.

[124] T. Corbitt, C. Wipf, T. Bodiya, D. Ottaway, D. Sigg, N. Smith, S. Whitcomb, and N. Mavalvala. Optical dilution and feedback cooling of a gram-scale oscillator to 6.9 mk. *Physical Review Letters*, 99:160801, 2007. URL **http://dx.doi.org/10.1103/PhysRevLett.99.160801**.

[125] LIGO Scientific Collaboration. Observation of a kilogram-scale oscillator near its quantum ground state. *New Journal of Physics*, 11(7):073032, 2009. URL **http://dx.doi.org/10.1088/1367-2630/11/7/073032**.

[126] T. Li, S. Kheifets, and M. G. Raizen. Millikelvin cooling of an optically trapped microsphere in vacuum. *Nature Physics*, 7:527 –530, 2011. URL **http://dx.doi.org/10.1038/nphys1952**.

[127] J. J. DiStefano, A. R. Stubberud, and I. J. Williams. *Schaum's outline of theory and problems of feedback and control systems, Second Edition.* Academic Press, 1990.

[128] B. C. Buchler, M. B. Gray, D. A. Shaddock, T. C. Ralph, and D. E. McClelland. Suppression of classic and quantum radiation pressure noise by electro-optic feedback. *Optics Letters*, 24(4):259 –261, 1999. URL **http://dx.doi.org/10.1364/OL.24.000259**.

[129] H. Rokhsari, T. J. Kippenberg, T. Carmon, and K.J. Vahala. Radiation-pressure-driven micro-mechanical oscillator. *Optics Express*, 13(14):5293 –5301, 2005. URL **http://dx.doi.org/10.1364/OPEX.13.005293**.